# The Fluorescence Yield of Air excited by Electron measured with the AIRFLY Experiment

**A. Obermeier**
**Institut für Kernphysik**

# The Fluorescence Yield of Air excited by Electrons measured with the AIRFLY Experiment

Andreas Obermeier

Institut für Kernphysik

Diplomarbeit an der Universität Karlsruhe (TH)

# The Fluorescence Yield of Air excited by Electrons measured with the AIRFLY Experiment

A very direct way to observe ultra high energy cosmic rays is the fluorescence technique. Fluorescence detectors are already used in various experiments since the early eighties, the latest being the Pierre Auger Observatory. The most important parameter for the description of the fluorescence light detected is the fluorescence yield that defines how much light a particle causes on its way through gas. The fluorescence yield depends on temperature, pressure, gas composition and energy of the exciting particle. Also, the fluorescence yield is a major source of uncertainty in the reconstruction of the primary energy, because up to now its value is only determined within around 15%.

This thesis describes the AIRFLY experiment that was set up to determine the fluorescence yield precicely. The pressure dependence of 18 spectral lines in the range of 280 nm to 430 nm has been determined using high resolution spectra. The spectral distribution of the fluorescence light in air has been measured and the effect of argon has been found to be negligible. The proportionality of the fluorescence yield to the energy deposit of the electrons has been confirmed between 1 MeV and 3 MeV. Adopting an absolute scale for the fluorescence yield at 337 nm as given by Nagano et al., the consequences of this works results for cosmic-ray measurements has been investigated.

# Messung der Fluoreszenzlicht-Ausbeute von mit Elektronen angeregter Luft mit dem AIRFLY Experiment

Den direktesten Weg, von Kosmischer Strahlung erzeugte extensive Luftschauer (EAS) zu beobachten, bietet die Fluoreszenz Methode. Seit den frühen '80er Jahren werden Fluoreszenz-Teleskope verwendet, zuletzt auch bei dem Pierre Auger Observatorium. Das damit beobachtete Fluoreszenz-Licht wird von atmosphärischem Stickstoff emittiert, der von den Teilchen des EAS angeregt wurde. Der wichtigste Parameter zur Beschreibung des Fluoreszenz-Lichtes ist die Fluoreszenzlicht-Ausbeute, die festlegt, wieviel Licht ein Teilchen auf seinem Weg durch Luft bewirkt. Die Fluoreszenzlicht-Ausbeute hängt dabei von Temperatur, Druck, Gaszusammensetzung und der Energie des anregenden Teilchens ab. Die Fluoreszenzlicht-Ausbeute ist auch die größte Fehlerquelle bei der Rekonstruktion der Energie des Primärteilchens, da sie bis jetzt nicht genauer als auf etwa 15% bestimmt werden konnte.

Diese Diplomarbeit beschreibt das AIRFLY Experiment, das aufgebaut wurde, um die Fluoreszenzlicht-Ausbeute genau zu bestimmen. Mit Hilfe hochaufgelöster Fluoreszenz-Spektren wurde die Druckabhängigkeit von 18 Spektrallinien zwischen 280 nm und 430 nm bestimmt. Es ist auch die spektrale Verteilung des Fluoreszenzlichtes genau vermessen worden und die Energieabhängigkeit der Fluoreszenzlicht-Ausbeute wurde zwischen 1 MeV und 3 MeV untersucht. Es konnte weiterhin kein signifikanter Effekt von Argon auf das Fluoreszenz-Licht beobachtet werden. Schließlich wurden die Auswirkungen der Ergebnisse dieser Arbeit auf die Messung der Kosmischen Strahlen untersucht.

# CONTENTS

# INTRODUCTION

Since their first detection, cosmic rays have revealed many secrets of Nature. Even today they provide us with particles that have many times more energy than anything man-made accelerators could achieve. If we are able to detect cosmic rays, we can put our understanding of Nature at highest energies to the test. But the interesting ultra high energy cosmic rays can only be observed indirectly by watching for extensive air showers that they cause by interacting with our atmosphere. The most direct way to do this is the fluorescence technique.

Fluorescence detectors are already used in various experiments since the early '80s, the latest being the Pierre Auger Observatory. The fluorescence light detected with these detectors is emitted by atmospheric nitrogen that is excited by charged particles of the extensive air shower along their way. The parameter that determines the number of emitted fluorescence photons is the fluorescence yield that defines how much light a particle causes on its way.

In general, the fluorescence yield depends on wavelength, temperature, pressure, gas composition, and energy of the exciting particle. Currently, the fluorescence yield is a major source of uncertainty in the reconstruction of the primary energy in air shower measurements, because up to now its value is determined within about 15% only.

In order to determine the fluorescence yield precisely, the AIRFLY experiment has been set up. The AIRFLY project consists of a series of laboratory experiments to measure the fluorescence yield of electrons in air under various conditions, that is undertaken by an international group of scientists. Early measurements have been conducted in Frascati (Italy), before the equipment was transferred to Argonne near Chicago (USA).

The fluorescence spectrum has never before been measured at different pressures with a spectrometer, when electron impact excitation was used. The high resolution allows for a detailed analysis of individual spectral lines, without the problem of pollution by nearby lines. Also, all but one measurements do not have to be absolute measurements.

All dependencies can be determined relative to the most intense band head at 337 nm, which reduces uncertainties. For the absolute measurement, a new end-to-end calibration procedure will be implemented, using the well understood Cherenkov radiation as a calibration source. This calibration method has the potential to be precise within 5%, because many systematic uncertainties cancel.

The aim of this thesis is the determination of the pressure dependence analysis of the fluorescence spectrum, which includes the analysis of 18 band heads that cover 90% of all fluo-

rescence light in the region of interest. A needed prerequisite is the knowledge of the pressure dependence of the most intense band head at 337 nm, which will be determined beforehand in photomultiplier measurements. The effect of argon on the spectrum will also be investigated, as well as the energy dependence of the fluorescence yield between 1 MeV and 3 MeV.

All results will be compared to other authors and experiments, especially with Bunner, who investigated the fluorescence technique in his PhD thesis in 1967 and gave the first set of parameters, and Nagano et al., whose work on the fluorescence yield, in 2004, is currently the standard fluorescence model for the Pierre Auger Observatory. Finally, the impact of the results of this thesis on extensive air shower measurements will be examined. The energy of primary cosmic-ray particles, derived with the current standard fluorescence model and a modified model, will be compared.

The absolute measurement of the yield, however, is beyond the scope of this diploma thesis, as well as measurements concerning the temperature dependence and the effect of water vapor, which are planned for future measurements within the AIRFLY project.

Since the measurement of the energy of cosmic radiation is the motivation for this thesis, an introduction to this subject and to fluorescence detectors is mandatory and given in Chapter 1. The actual physical concepts needed later in this thesis are concepts of molecular physics. Thus, Chapter 2 gives an introduction to this field and defines all physical relations and parameters that will be used in the analysis of AIRFLY data.

The AIRFLY experiment is described in Chapter 3, which is restricted to essential aspects, because this thesis is not dedicated to AIRFLY's hardware setup. In Chapter 4 the analysis begins with the investigation of the 2P(0,0) band head, whose behavior at changing pressure and electron energy will be studied. The results of this analysis are used as input in Chapter 5 that deals with the fluorescence spectrum. There, crucial parameters will be derived for the first time in a consistent manner for the full fluorescence spectrum excited by electron impact. Chapter 6 will then highlight the impact of these results on extensive air shower measurements of the Pierre Auger Observatory. A summary and an outlook is given in Chapter 7.

# Chapter 1

# Cosmic Radiation and its Detection

This chapter gives an introduction to discovery, properties, and detection of cosmic radiation.

## 1.1 Cosmic Rays

The phenomenon of cosmic radiation first hit scientists at the beginning of the $20^{th}$ century, when Viktor Hess discovered an increase of "penetrating radiation" at high altitudes during his famous balloon flights in 1912 [31]. He concluded that this phenomenon could not be explained by the recently discovered earthbound radioactivity [32], and so a new source of radiation was necessary to explain his findings: cosmic radiation from outer space.

The questions about cosmic rays back then were the same as they are today:

- What does cosmic radiation consist of?

- What energy do cosmic rays have and how are they accelerated?

- Where do they come from?

To answer these questions, scientists began to undertake many of experiments (see for instance [61]). At first, there were more balloon flights and later on even satellite and aircraft experiments were realized. After Kolhörster [43] and Auger [6] discovered "extensive cosmic-ray showers" in 1938 also ground arrays were constructed.

In 1948 experiments of Bradt and Peters [11] revealed that the primary components comprised, in addition to protons, of a small fraction of other nuclei. It was also found, that cosmic rays extend to energy regions that are not accessible by any other means. Even today the most powerful man-made accelerators cannot reach the energies of cosmic rays. This enabled scientists to make several major discoveries concerning particle physics in general.

In 1933, the positron was found by Anderson [2], followed by the muon [53, 66], the pion, and several strange particles like the kaon. But not only particle physics had its share, the first experimental proof of special relativity was the observation of time dilatation of the muon lifetime. A lifetime of $2.2 \cdot 10^{-6}$ s allows muons to travel about 660 m at the speed of light, i.e. they would never reach the Earth's surface from higher altitudes. Thus, the observation of muons at ground

level is a sign for relativistic time dilatation that expands the lifetime, so that the particles can cover a greater distance.

However, despite all efforts to solve the central questions regarding cosmic radiation, there are still many unsolved problems. In the following a short description of the current knowledge about cosmic rays will be given.

### 1.1.1   Composition

Despite the name, cosmic radiation does not consist of photons, but mostly of atomic nuclei. The major part are protons, but all elements up to uranium have been found.

At low energies (i.e. lower than $10^{14}$ eV) the primary composition of cosmic rays can be measured directly by means of balloon or satellite experiments (see [42, 46]). In Figure 1.1, the results of direct measurements of elemental abundance as a function of nuclear charge of elements in cosmic radiation and in the solar system is shown. Although the data points are in good overall agreement, which is a strong sign for the source of low energetic cosmic rays being stars like the sun, there are some important differences.

Hydrogen and helium are more abundant in the solar system, which can be explained by their large first ionization potential that renders the acceleration processes less efficient. This also explains other small deviations of abundances of other elements. The second discrepancy is the amount of Li, Be, B and elements below iron in the cosmic radiation, which is several magnitudes higher than in the solar system. These elements are products of spallation processes of carbon, oxygen or iron, that collide with interstellar matter.

This assumption enables us to calculate the distance between the source and the detectors at Earth that the nuclei have to traverse: They have to cross 5-10 g/cm$^2$ of interstellar matter to produce the observed amount of spallation products. Thus, they travel for $3 \cdot 10^6$ years (assuming the density of our Galaxy is 1 proton/cm$^3$) before reaching the Earth [46]. Assuming cosmic radiation is of galactic origin, this implies that the particles do not approach the Earth in a straight line, but travel in a diffuse, undirected way many times through our Galaxy before eventually crossing the Earth's path.

Another way to calculate the age of cosmic rays provide so-called "cosmic ray clocks", radioactive nuclei with very long lifetimes. An analysis reveals a confinement time of $10^7$ years within our Galaxy, which in turn requires the galactic density to be 0.2 protons/cm$^3$. So, most of their time cosmic ray particles travel in the galactic halo, the edge of our Galaxy.

At high energies (above $10^{15}$ eV) the composition is expected to change. Due to the acceleration process, that reaches its maximum energy $E_{max}$ ($E_{max} \propto Z$, with nuclear charge Z) and the ability of the Galactic magnetic field to confine high energy particles (also $\propto Z$, "leaky box model"), the mean mass should increase, for example, from about 7 u at $10^{15}$ eV to 55 u at $10^{17}$ eV [35] — depending on the model used. However, it is difficult to determine the mass composition for these high energies, because cosmic-ray particles cannot be observed directly, but only secondary particles of cascades in the atmosphere caused by cosmic rays. Thus, the indirect measurement of the particle mass depends on simulations and interaction models, and
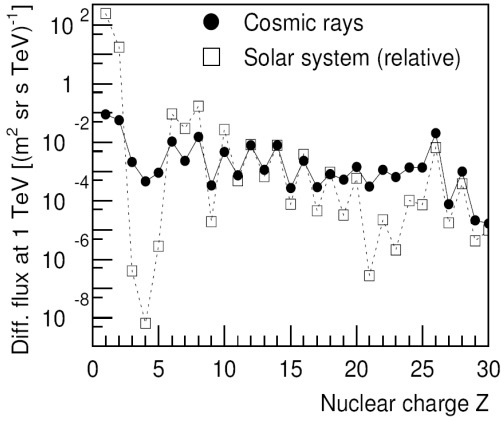
**Figure 1.1:** Abundance of elements ($Z < 28$) at $10^{12}$ eV measured directly, normalized to Si. The differences between cosmic ray and solar abundances are explained in the text. [36]
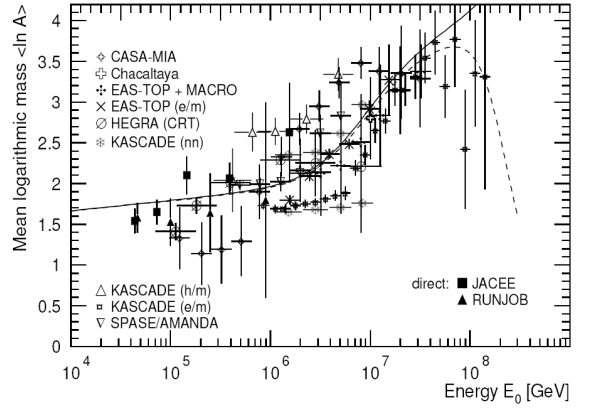
**Figure 1.2:** Mean logarithmic mass as a function of energy reconstructed from experiments observing the particle cascade caused by cosmic rays at ground level. [35]

is therefore neither precise nor unambiguous.

Figure 1.2 shows the results of the reconstruction of the mean mass of cosmic rays by several experiments that measure secondary particles at ground level. For comparison two balloon experiments are included as well. The lines represent the composition according to the "poly gonato" model [35]. At even higher energies (above $10^{17}$ eV) it could be possible (as the dotted line in Figure 1.2 indicates) that cosmic rays mainly consist of protons and helium again, because their sources are assumed to be extragalactic.

## 1.1.2 Energy Spectrum

The energy spectrum of cosmic radiation covers 12 orders of magnitude in energy and over 30 orders of magnitude in flux. It can be described with a broken power law:

$$\frac{dN}{dE} \propto E^{-\gamma}, \qquad \gamma = \begin{cases} 2.75, & E \lesssim 4 \cdot 10^{15}\,\text{eV} \\ 3.05, & 4 \cdot 10^{15}\,\text{eV} \lesssim \text{E} \lesssim 10^{19}\,\text{eV} \\ 2.75, & E \gtrsim 10^{19}\,\text{eV}. \end{cases} \qquad (1.1)$$

The spectrum begins at around $10^9$ eV with a flux of more than 1 particle per m$^2$ and second, and has been observed up to $10^{20}$ eV with a flux of about 1 particle per km$^2$ and century [51]. Figure 1.3 shows the spectrum scaled by E$^{2.5}$, as it is reported by several experiments.

The first change in the spectral index $\gamma$ occurs at 4 PeV, called the "knee", and is well investigated by several experiments. An analysis of the KASCADE experiment [67], shows that the change is correlated with a shift in mass composition towards heavier nuclei. The overall effect is a steeper spectrum.

Less understood is the second change of $\gamma$ at the "ankle" around 10 EeV. Statistics in this region is very low and the reason of the change has not been clearly explained up to now, but
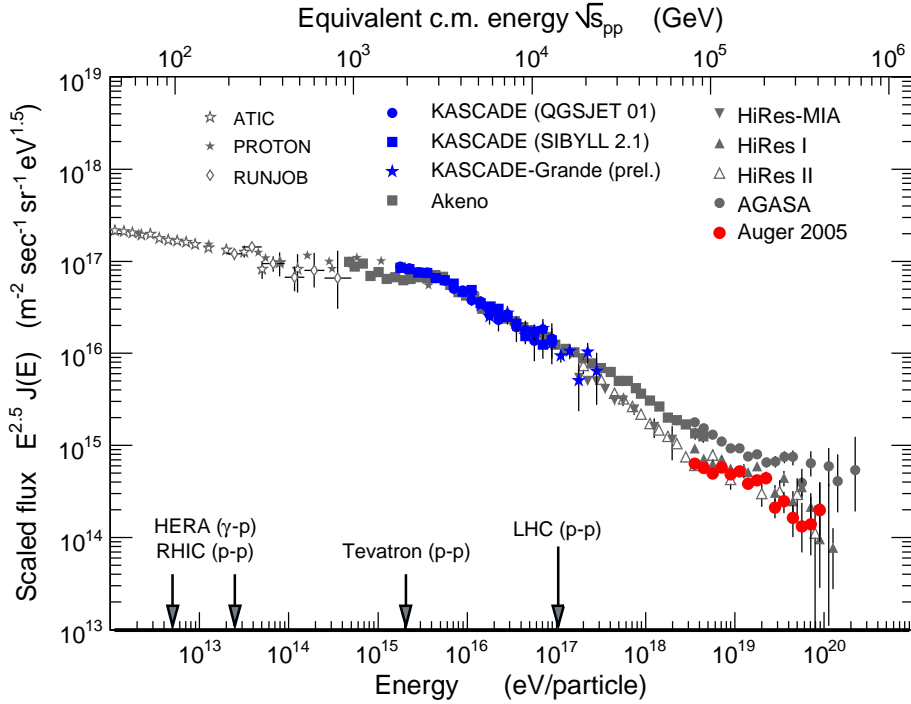
**Figure 1.3:** Flux of primary cosmic rays as a function of energy above 100 GeV scaled with $E^{2.5}$. The power law is broken at the "knee" (at $10^{15}$ eV) and the "ankle" (at $10^{19}$ eV). For comparison, maximum energies of some accelerators are indicated. [22, 23]

experimental results (for example of the HiRes experiment, [65]) suggest, that the mass composition shifts towards lighter nuclei, which can be interpreted as a transition from galactic to extragalatic sources.

It is difficult to identify processes that accelerate these particles to macroscopic scale. A proton at $10^{20}$ eV has the energy of a tennis ball moving at 100 km/h. A general acceleration process for particles was introduced by Fermi [24], that explains the power law spectrum and the knee: A particle is confined in a magnetic plasma and crosses a shock front, i.e. of a supernova remnant.

Each time the particle crosses the shock front it gains energy proportional to its initial energy, $\Delta E = \epsilon E$, and has a chance of escaping the region of the shock $P_e$. After $n$ turns it has an energy of $E_n = E_0(1 + \epsilon)^n$, and the number of particles that gain more energy than $E$ is given by

$$N(E) \propto \frac{1}{P_e}\left(\frac{E}{E_0}\right)^{-\gamma},\tag{1.2}$$

with

$$\gamma = \frac{\ln(\frac{1}{1-P_e})}{\ln(1+\epsilon)}.\tag{1.3}$$

The maximum energy depends on the ability of the plasma to confine the particle, which is

proportional to its size and magnetic field. A general estimate yields [33, 51]

$$E_{max} = 0.9 \cdot ZBR, \tag{1.4}$$

with $E_{max}$ in units of EeV, the magnetic field strength $B$ [$\mu$G], radius $R$ [kpc] of the plasma cloud and nuclear charge $Z$ of the particle. The dependence on Z can explain the knee, because protons have smaller maximum energies than iron, which is in agreement with the observed increase in mass.

The limit (1.4) can be used to classify astrophysical objects as sources for cosmic rays. This is shown in a Hillas plot, Figure 1.4. There, a constant $E_{max}$ refers to a straight line, and objects above it are able to accelerate a particle that much. The position of the line depends, as shown, on the particle charge and the velocity of the shock front. So far, no galactic objects have been found to accelerate particles to $10^{20}$ eV.

Another restriction to the observable energy spectrum is the Greisen-Zatsepin-Kuz'min-effect (GZK-effect, [28, 70]) that causes a supression of the flux close to 100 EeV. This GZK-cutoff is due to energy losses of particles during their propagation through space, because cosmic rays interact with the cosmic microwave background (CMB). The interactions are photodisintegration of a nucleus $X$ with mass $A$ and pion production of protons:

$$X^A + \gamma_{CMB} \longrightarrow X^{A-1} + p\,(n), \tag{1.5}$$

$$p + \gamma_{CMB} \longrightarrow \Delta^+(1232) \longrightarrow p + \pi^0, \quad n + \pi^+. \tag{1.6}$$

The intermediate state of the pion production is the nuclear resonance $\Delta^+$ with a mass of 1232 MeV/c$^2$ and a lifetime of $5.5 \cdot 10^{-24}$ s [58]. Figure 1.5 illustrates the GZK energy loss for three initial energies. The experimental confirmation of the GZK-effect is still under discussion, because in this energy region very few experimental data is available.

If the spectrum has no cut-off, cosmic rays have to originate in our very neighborhood (less than 200 Mpc away), which would support speculations about new physics, like topological defects or superheavy (supersymmetric) particles, that decay into highest energy protons and other particles. If the GZK-cutoff does not exist at all, even a violation of the Lorentz symmetry is possible, because this would shift the GZK threshold energy to even higher energies [51].

Since the cosmic-ray energy spectrum covers huge ranges in both energy and flux, very different techniques are required to measure it completely. The next section gives a short overview on the observation of ultra-high energy cosmic rays with fluorescence detectors.

## 1.2 Detection of Cosmic Rays

Above 100 TeV cosmic radiation cannot be measured directly, but only by means of extensive air showers. These huge cascades of secondary particles can be observed by ground arrays, and emit, above 1 EeV of primary energy, enough fluorescence light to be seen by optical detectors.
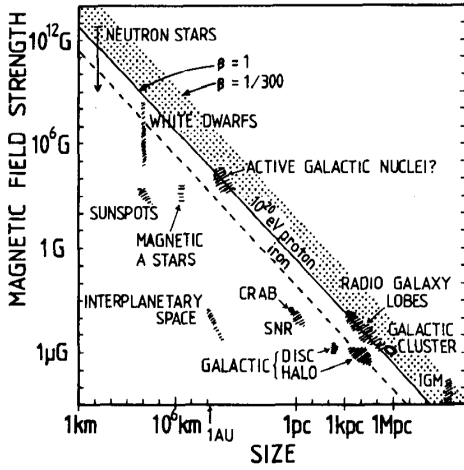
**Figure 1.4:** Hillas plot (1984): Characterization of astrophysical objects with respect to size and magnetic field strength. Objects below the lines cannot accelerate particles to $10^{20}$ eV. $\beta$ refers to the velocity of the shock front. [33]
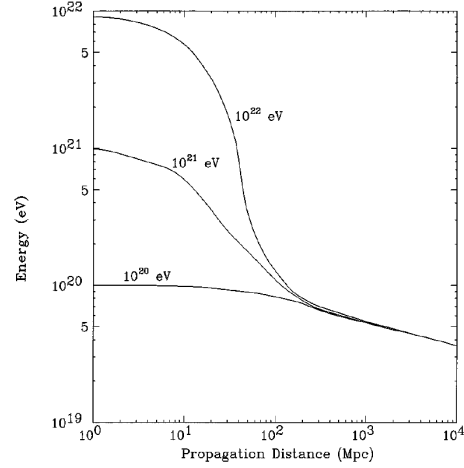
**Figure 1.5:** Energy of ultra high energy protons as a function of travelled distance. Illustration of the GZK-effect: After 200 Mpc initial energies are reduced to below $10^{20}$ eV. [19]

## 1.2.1   Extensive Air Showers

Extensive Air Showers are created, when a primary cosmic-ray particle collides with a nucleus of a molecule in the atmosphere. This collision produces secondary particles that collide themselves with other nuclei. This way, a cascade is generated that arrives at the Earth's surface.
The hadronic cascade proceeds at the center of the cascade feeding other parts with products of more and more collisions, until the energy of its particles is too low to initiate further reactions. In these reactions a wide variety of particles is produced, but the most common products are pions ($\pi^0$, $\pi^\pm$), that decay into muons and electrons to feed muonic and electromagnetic cascades. Their decay channels are

$$\pi^\pm \longrightarrow \mu^\pm + \nu_\mu(\overline{\nu_\mu}), \tag{1.7}$$

$$\pi^0 \longrightarrow \underbrace{\gamma + \gamma}_{98.8\%}, \quad \underbrace{e^+ + e^- + \gamma}_{1.2\%}. \tag{1.8}$$

Figure 1.6 shows a schematic diagram of the components of an extensive air shower. Most muons reach Earth and establish an muonic part of the extensive air shower, even if some of them decay into electrons and neutrinos, again feeding the electromagnetic cascade. Electrons and photons themselves lose energy and increase their numbers by a series of pair production and bremsstrahlung processes

$$\gamma \longrightarrow e^+ + e^-, \tag{1.9}$$

$$e^\pm \longrightarrow e^\pm + \gamma. \tag{1.10}$$

Soon after the first interaction, the electromagnetic cascade is the major part of the shower and deposits its energy into the atmosphere. Figure 1.7 shows the deposited energy of the shower
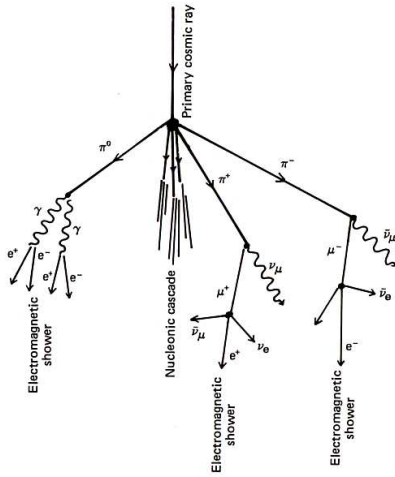
**Figure 1.6:** Sketch of an air shower with hadronic and electromagnetic component. Some muons do not decay before reaching the surface and thus form a third component that is not shown here. [46]
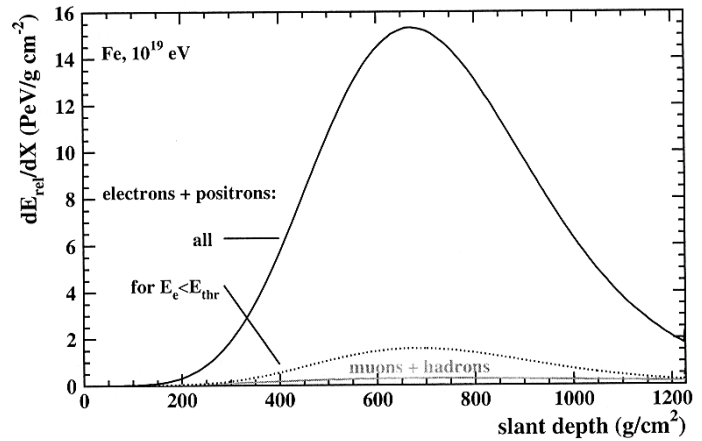
**Figure 1.7:** Longitudinal shower development (simulated) indicated by means of energy deposit as a function of slant depth. Ground level corresponds to circa 1036 g/cm$^2$ of atmospheric depth at sea level. It can be seen that the shower maximum is well above the ground and that electrons release the most energy into the atmosphere. [62]

particles along their way as a function of slant depth, which denotes the atmospheric depth in g/cm$^2$ along the shower axis. The vertical thickness of the atmosphere is 1036 g/cm$^2$. It can be seen, that the maximum of the shower is well above sea level, and that electrons are the dominant particles in an extensive air shower as far as energy deposit is concerned. For a detailed description see [46, 61].

Atmospheric nitrogen is excited by these electrons and emits fluorescence light. Since the emission is very faint and isotropic, it is hardly visible. But for showers of primary energy higher than $10^{17}$ eV, in moonless nights, it is possible to detect these traces on the sky with telescopes. This fluorescence technique is applied in the Pierre Auger Observatory.

## 1.2.2   Fluorescence Detectors and the Pierre Auger Observatory

Being the newest cosmic ray detector and the first one that is equipped with both surface and fluorescence detectors, the tasks set to the Pierre Auger Observatory [1, 10] are ambitious. Its aim is to observe ultra high energy cosmic rays with unprecedented accuracy, to look for point sources and to settle an important argument: The energy spectra put forward by AGASA (a surface detector, [64]) and HiRes (a fluorescence detector, [65]) do not agree, especially in the region the GZK-cutoff is presumed (see Figure 1.3). Since the Pierre Auger Observatory is equipped with both detector types, it can search for systematic differences in the reconstruction procedures, and its size should increase the statistics significantly.

The southern part of the Observatory is located in the Argentinian Pampa Amarilla close to Malargüe. After completion, it will cover 3000 km$^2$ with its 1600 water tanks, which measure
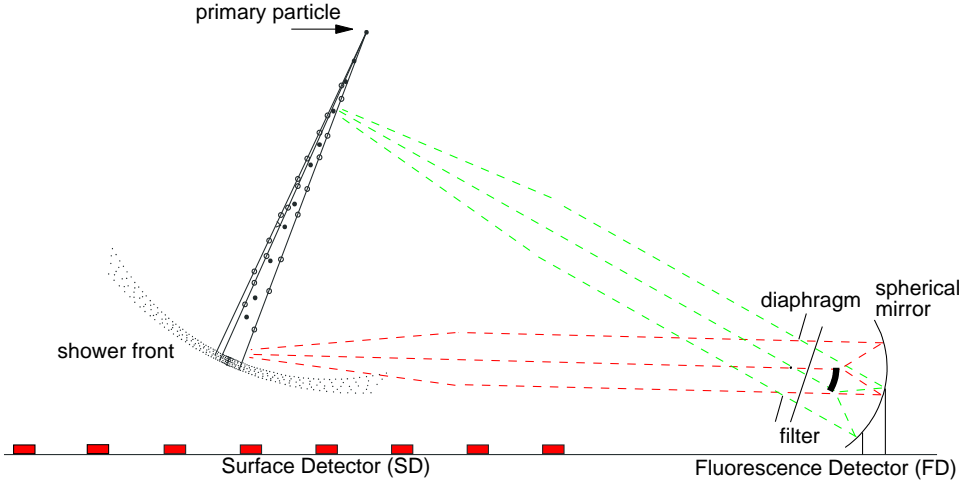
**Figure 1.8:** Schematic view of a hybrid detector as implemented in the Pierre Auger Observatory. The surface detector an the fluorescence detector observe extensive air showers simultaneously [68]

Cherenkov light of passing particles. This area will be overlooked by four fluorescence stations, each consisting of six independent telescopes. The principle of measurement with these fluorescence detectors is depicted in Figure 1.8. A detailed map of the area is shown in Figure 1.9. The most prominent features of the fluorescence telescopes are a filter for light between 300 nm and 400 nm, a segmented, spherical mirror to focus the light and a camera consisting of 440 photomultiplier tubes (PMTs). The filter suppresses light from sources like stars, reducing the background significantly. The mirror, with a radius of 3.4 m, focuses the light and directs it to the camera, which is in front of its focal point, with conserved pointing. Each of the 440 PMT-pixels of the camera has a field of view of $1.5°$. The four telescope stations have each a $180° \times 28.6°$ field of view, directed towards the experimental site. For more details see [1] and Figure 1.10.

The number of photons a pixel of a fluorescence telescope detects is assumed to be proportional to the deposited energy $E_{dep}$ of ionizing particles in the volume it observes at atmospheric depth $X$:

$$\frac{dN_\gamma}{dX} = \frac{dE_{dep}^{tot}}{dX} \cdot \int Y(\lambda, T, p) \cdot \tau_{ATM}(\lambda, X) \cdot \epsilon_{FD}(\lambda, X) \, d\lambda. \qquad (1.11)$$

Where $\epsilon_{FD}$ denotes the detector efficiency, $\tau_{ATM}$ the transmittance of the atmosphere and $Y(\lambda, T, p)$ the fluorescence yield that dependends on pressure, temperature and wavelength. Equation (1.11) is only true, if the fluorescence yield (in units of photons per deposited energy) is independent of the energy of the ionizing particles. To get the energy of the primary particle, $E_{dep}$ has to be multiplied by a factor $f_{inv}$ that accounts for all invisible (not deposited) energy [57], i.e. escaping muons and neutrinos.

Within this calculation, at present the fluorescence yield is the largest single source of uncertainty [7]. Therefore it is crucial to obtain more accurate knowledge of the fluorescence yield with laboratory experiments like AIRFLY. The current systematic uncertainties of the primary energy reconstruction of the fluorescence detectors of the Pierre Auger Observatory are listed

| source | uncertainty |
|---|---|
| absolute FLY | 13% |
| pressure dep. of FLY | 4% |
| humidity dep. of FLY | 5% |
| temperature dep. of FLY | 5% |
| $f_{inv}$ | 3% |
| sum of other sources | 19% |
| TOTAL | 25% |

**Table 1.1:** Current systematic uncertainties of the reconstruction of the primary energy by the Auger fluorescence detector. The abbreviation FLY denotes the fluorescence yield. [7]

in Table 1.1.    In order to increase the precision of extensive air shower measurements, the AIRFLY experiment measures the fluorescence yield under various conditions. The scope of this thesis covers the dependence of the fluorescence yield on pressure and wavelength, and investigates its energy dependence.

Early measurements of the AIRFLY project that is carried out by an international group of scientists are described in [3, 4]

Important features of AIRFLY include spectrometer measurements and a new strategy of an end-to-end calibration. Before these measurements can be properly described it is necessary to understand the process of fluorescence. Thus, the next chapter deals with spectra of diatomic molecules and some considerations about the fluorescence yield.
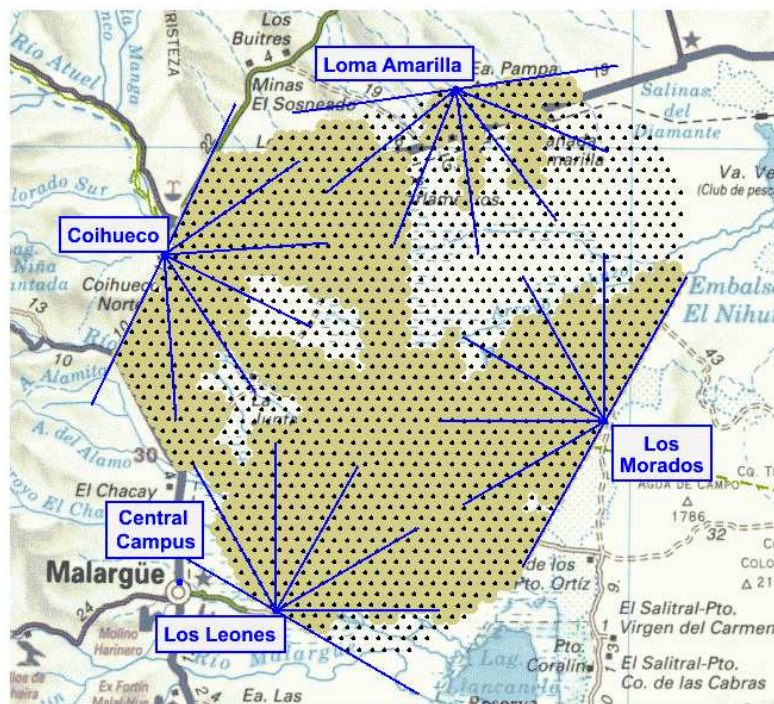
**Figure 1.9:** Map of the southern Auger site in Argentina with indicated fluorescence telescopes and tank positions. The telescope station Loma Amarilla is currently under construction, tank points with dark underlay are taking data (as of 8/2006). Courtesy of J. Oehlschläger.
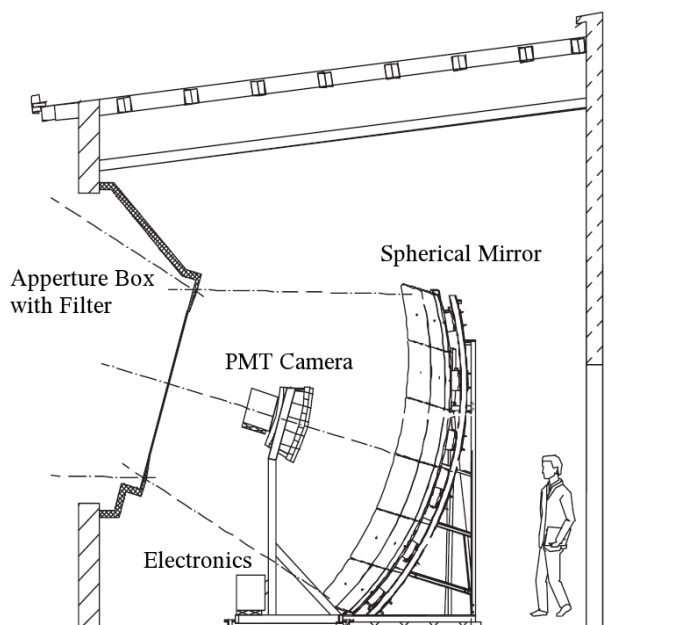


**Figure 1.10:** Sketch of one single telescope. Six of these "eyes" are combined to one detector station. [1]

# CHAPTER 2

# MOLECULAR SPECTRA AND FLUORESCENCE

The source of fluorescence light, that is detected by cosmic-ray experiments, is molecular nitrogen, because no other air-component has spectral lines at relevant intensities within the wavelength region of the observed fluorescence light, between 280 nm and 430 nm [56]. Figure 2.1 shows photographs of the nitrogen bands of the 2P and 1N electronic transitions of $N_2$ and $N_2^+$, that are in the mentioned region. Each band belongs to a vibrational transition within the electronic band system and consists of many lines of a rotational substructure. To explain their appearance, an introduction to molecular physics is given.

Since nitrogen is a diatomic, homonuclear molecule, the first part of the following chapter will deal with this special case, and will introduce the different possible transitions and how they build up the observed spectrum. Therefore, since a transition is always related to two states of certain energy, energy levels related to the different degrees of freedom of the molecule will be derived. For this part the main sources are textbooks on molecular physics and spectra [8, 30]. The second part describes the production of fluorescence light as a product of excitation and de-excitation processes, that will lead to a model of the fluorescence yield. This model will be used to interpret the measurements of the AIRFLY experiment. The model was already used to
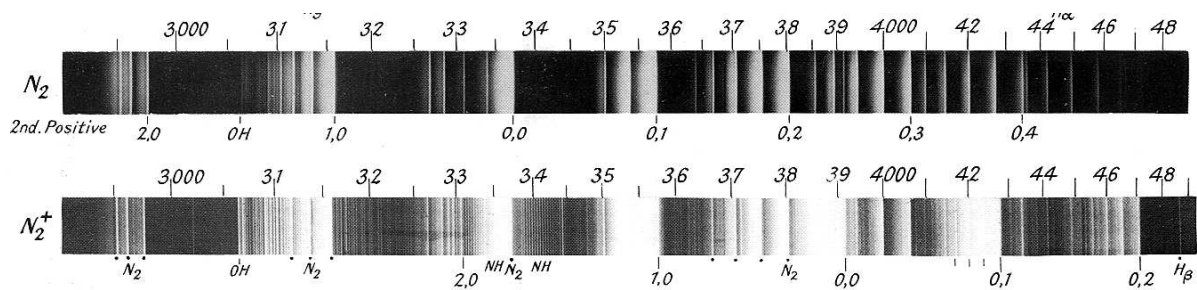


**Figure 2.1:** Emission lines of the second positive (2P) system of $N_2$ and the first negative (1N) system of $N_2^+$ between 290 nm and 480 nm. Recorded on photographic plates. Above each plate the wavelength is given in Angström (3000 Å = 300 nm). [56]

13

interpret the data of prior experiments, like [50, 69], but has been reviewed and in some aspects altered for the use in this thesis.

## 2.1 Transitions of Diatomic Molecules

For diatomic molecules there are, in addition to electronic transitions every atom (and molecule) can perform, transitions due to vibration and rotation, consistent with the respective degrees of freedom of vibrating along the axis between the two atoms, and rotating around it. This gives rise to additional terms in the calculation of the energy of the emitted photon, that determines the position of the spectral line. It reads as

$$h\nu = \Delta E_{el} + \Delta E_{vib} + \Delta E_{rot}. \tag{2.1}$$

Since the electron has a many times smaller mass than the nucleus, it follows every possible move of the nucleus with negligible delay. This allows the use of the Born-Oppenheimer approximation, to calculate the total energy of a molecular state as a simple sum of independent contributions, and the state $\Psi$ itself as their product

$$E = E_{el} + E_{vib} + E_{rot}, \tag{2.2}$$

$$\Psi = \Psi_{el} \cdot \Psi_{vib} \cdot \Psi_{rot}. \tag{2.3}$$

However, the energy scale of rotation is smaller than of vibration, which is in turn smaller than the one of electronic transitions [8]. This causes respective substructures in molecular spectra. An estimation yields

$$E_{el} \; : \; E_{vib} \; : \; E_{rot} \; = \; 1 \; : \; \sqrt{\frac{m}{M}} \; : \; \frac{m}{M}, \tag{2.4}$$

with mass of the electron $m$, and of the molecular nucleus $M$.

### 2.1.1 Electronic States

To understand electronic transitions of a molecule, its electronic states have to be defined first. Therefore, molecular orbitals are described as linear combinations of atomic orbitals (LCAO-method) [30].
The molecular nuclei and hence the Coulomb potential have, at least in our special case, cylindrical symmetry. This means, that the quantum number of angular momentum $l$ is no good quantum number any more, but the quantum number of its z-component $m_l$ is (z direction is chosen along the molecule's axis). Since the directions of the rotation of the electron angular momentum around the z-axis are equally energetic, a new quantum number $\lambda$ is defined

$$\lambda = |m_l| = l, l - 1, \ldots, 0. \tag{2.5}$$

Like atomic orbitals, that are denoted with Latin letters (s,p,d,f,...) respectively to $l$, molecular orbitals are denoted with Greek letters ($\sigma$, $\pi$, $\delta$, $\varphi$, ...) with respect to $\lambda$. But in order to ease

understanding, the orbital's former quantum numbers are kept in notation.

The symmetry of the new orbital is noted as index "g"[1] for symmetrical or "u"[2] for asymmetrical. If it is bonding or anti-bonding, is mentioned with a " $*$ ".

For example, $2s\sigma_u^*$ denotes a former $2s$ atomic orbital, that is now an asymmetric, anti-bonding molecular orbital with $\lambda = 0$, that can hold two electrons, because of their spin $s = \pm 1$. A $\pi$-orbital could hold four electrons, because of the electronic spin $s$ and $m_l = \pm 1$.

These abbreviations are used in Figure 2.2, which shows how the molecular orbitals (MO) are occupied by electrons of former atomic orbitals (AO) in case of nitrogen. The nitrogen electronic configuration of its ground state is

$$(1s\sigma_g)^2(1s\sigma_u^*)^2(2s\sigma_g)^2(2s\sigma_u^*)^2(2p\sigma_g)^2(2p\pi_u)^4, \tag{2.6}$$

where the superscripts denote the number of electrons the orbital contains. All the electrons in their orbitals define the electronic state. In the notation of electronic states with more than one electron, the sums of single electron quantum numbers are used. The total z-component of the angular momentum

$$\Lambda = \sum \lambda_i, \tag{2.7}$$

noted as uppercase Greek letters ($\Sigma, \Pi, \Delta, \ldots$), and the total electron spin

$$S = \sum |s_i|, \tag{2.8}$$

noted as multiplicity $2S + 1$.

Again, information about symmetry is included as indices. Sub-scripts "g" and "u" note the parity of the state, "+" and "-" the symmetry with respect to the plane through the molecule's axis. This way the ground state of N$_2$ is noted as $^1\Sigma_g^+$. Another notation (Mullikin notation) passes information regarding symmetry with uppercase Latin letters, corresponding to mathematical operations, like $C^3\Pi_u$.

Figure 2.3 depicts the electronic transition of the second positive system of neutral nitrogen with a sketch of the electronic energy curves. All transitions, also the 2P-transition ($C^3\Pi_u \longrightarrow B^3\Pi_g$) of N$_2$ and the 1N-transition ($B^2\Sigma_u \longrightarrow X^2\Sigma_g$) of N$_2^+$, are usually accompanied by vibrational and rotational transitions.

## 2.1.2 Vibrational Transitions

Molecules can vibrate, changing the distance between the two nuclei that are confined in a so-called Morse potential [30]. The potential is shown in Figure 2.4 with the corresponding energy levels, disintegration energy $D_e$, internuclear distance at the minimum $R_e$ and some indicated transitions. It can be expressed as

$$V(R) = D_e[1 - e^{-a(R-R_e)}]^2. \tag{2.9}$$

---

[1]"**g**erade" (German for even)

[2]"**u**ngrade" (German for odd)
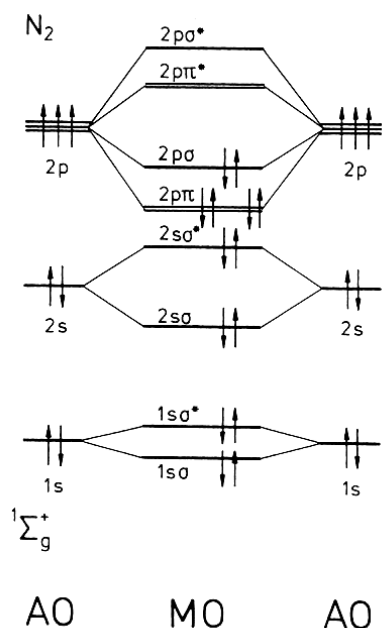
**Figure 2.2:** Scheme of energy states showing how two nitrogen atoms (AO) form molecular orbitals (MO). The notation follows the description in the text. The three outer orbitals are bonding, explaining the chemical notation N≡N. [30]
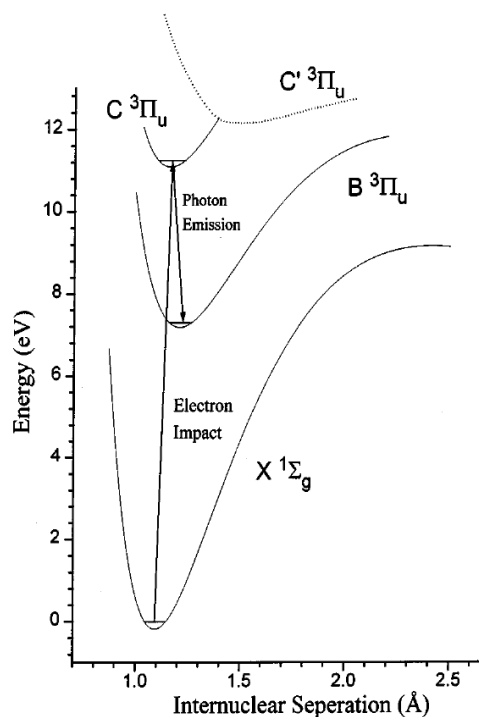
**Figure 2.3:** Respective states of the 2P electronic transition of $N_2$ and its ground state, shown as a plot of the respective Morse potentials as a function of internuclear distance. An electron impact excitation is assumed. [26]

Near $R_e$ (i.e. for small vibrational quantum numbers $\nu$), the Morse potential can be approximated by a parabola, and thus the vibration is treated as a harmonic oscillator with corrections. The vibrational energy levels converge towards higher quantum numbers $\nu$, as Figure 2.4 shows. The inhomogeneous energy eigenstates can be expressed as

$$E_\nu = \underbrace{\hbar\omega\left(\nu + \frac{1}{2}\right)}_{\text{harm. osc.}} \cdot \left[1 - x_e\left(\nu + \frac{1}{2}\right) + \dots\right], \qquad (2.10)$$

with

$$x_e = \frac{\hbar\omega}{4D_e} \approx 0.08|_{N_2}.$$

This changes the selection rules for vibrational transitions. As for the harmonic case only transitions with $\Delta\nu = \pm 1$ are allowed, here transitions with $|\Delta\nu| = 1, 2, 3, \dots$ are possible [30], although with less relative intensities that behave like $1 : x_e : x_e^2 : \dots : x_e^{|\Delta\nu|-1}$. However, for homonuclear, diatomic molecules a change of the vibrational state does not change the dipole moment of the molecule, and thus pure vibrational spectra are optically forbidden and cannot be observed.
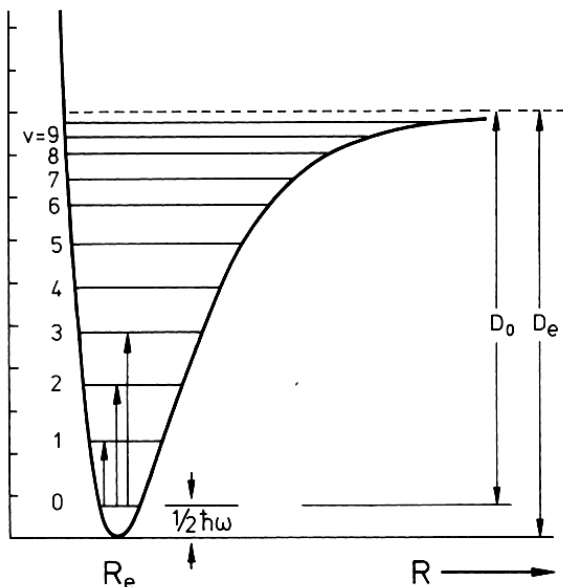
**Figure 2.4:** Morse potential and vibrational energy levels, with dissociation potential $D_e$ and zero-level energy $\hbar\omega/2$. In approximation, the Morse potential is replaced by the quadratic potential of the harmonic oscillator.[30]
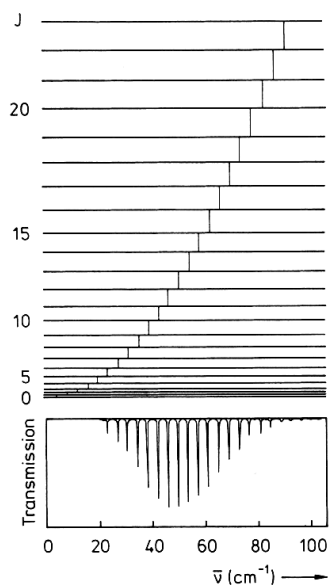
**Figure 2.5:** Energy of rotational states. Their energy difference increases with quantum number J, which leads to equidistant lines in the rotational spectrum, as shown at the bottom. [30]

## 2.1.3  Rotational Transitions

The classical calculation of the energy of an inelastic rotator results in

$$E_{rot} = \frac{L^2}{2\theta},\tag{2.11}$$

with the angular momentum $L$ and moment of inertia $\theta$.

In the quantum mechanical case, the magnitude of the angular momentum is quantized and can be expressed as $|L| = \hbar \cdot \sqrt{J(J+1)}$, with the quantum number $J = 0, 1, 2, \ldots$. This, combined with Equation (2.11), yields an expression for the energy of rotational states in a molecule:

$$E_{rot} = \frac{\hbar^2}{2\theta} \cdot J(J+1), \quad J = 1, 2, \ldots.\tag{2.12}$$

Since the energy difference between two states increases linearly with $J$, and only transitions with $\Delta J = \pm 1$ are allowed, a pure rotational spectrum consists of equidistant lines, as Figure 2.5 shows. The intensity of the lines is determined by the degeneration of the energy levels and their thermal population [8].

If the vibration of molecules is taken into account, the inelastic rotator has to be modified, since the distance of the two masses, and therefore the moment of inertia, is not constant any more. This leads to corrections in Equation (2.12) that are not negligible for high quantum numbers

$J$.

A requirement for the existence of pure rotational spectra is a permanent dipole moment [8], that homonuclear, diatomic molecules do not have. However, in combination with electronic transitions, vibrational and rotational transitions occur and cause substructures in the spectrum. This spectrum will be discussed in the next section.

## 2.2    The Spectrum of Molecular Nitrogen

The spectrum of molecular nitrogen in the range of 280 - 430 nm, is composed of several band heads of the 2P- and 1N-band-systems of $N_2$ and $N_2^+$ respectively. The labels "2P" (second positive) and "1N" (first negative) are historical, and describe the place of emission in a gas discharge tube. They correspond to the following electronic transitions with their vibrational states indicated by $\nu$:

$$2P(\nu', \nu''): \quad C^3\Pi_u(\nu') \longrightarrow B^3\Pi_g(\nu''),$$

$$1N(\nu', \nu''): \quad B^2\Sigma_u(\nu') \longrightarrow X^2\Sigma_g(\nu'').$$

For optical transitions the molecular dipole moment has to change, or — more general — the corresponding transition matrix element needs to be non-zero:

$$\langle \Psi_{final}|\mathcal{M}|\Psi_{initial}\rangle \neq 0. \tag{2.13}$$

This requirement can be used to derive selection rules for optical transitions [8, 30]. They turn out to be

- Total angular momentum: $\Delta\Lambda = 0, \pm 1$.

- If $\Lambda = 0$ ($\Sigma$-states), symmetry has to be conserved: $\Sigma^+ \leftrightarrow \Sigma^+$, $\Sigma^- \leftrightarrow \Sigma^-$.

- Total electronic spin: $\Delta S = 0$.

- Rotational quantum number: $\Delta J = \begin{cases} \pm 1, & \Lambda' = \Lambda'' = 0 \\ 0, \pm 1, & \text{otherwise.} \end{cases}$

- Laport's rule: $g \leftrightarrow u$ (The state's parity has to change).

With these selection rules, spin-orbit coupling is not considered, which allows the total electron spin $S$ to change. However, such transitions are very rare, and thus have very little intensity, so they are not observed. There is no constraint limiting vibrational transition, which is due to the inhomogeneous Morse potential, that allows $\nu$ to change freely (see section 2.1.2). As discussed earlier, these transitions with $|\Delta\nu| \geq 3$ are very faint and hardly observed here.

Also, the inhomogeneity causes the energy level to be not equidistant, so that band heads, associated with transitions with $|\Delta\nu| = const.$, are shifted and not at the same position in the spectrum. For example, the $2P(2,3)$ and $2P(1,2)$ band heads lie 3.6 nm apart, which corresponds to $\approx 0.04$ eV difference in energy.
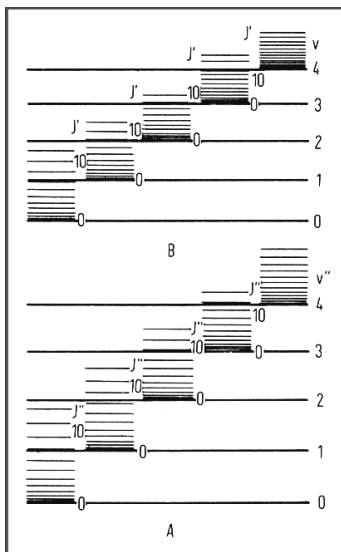
**Figure 2.6:** Scheme of energy levels of two electronic states $A$ and $B$. Each has vibrational sub-levels ($\nu$) that have rotational energy levels ($J$). [8]
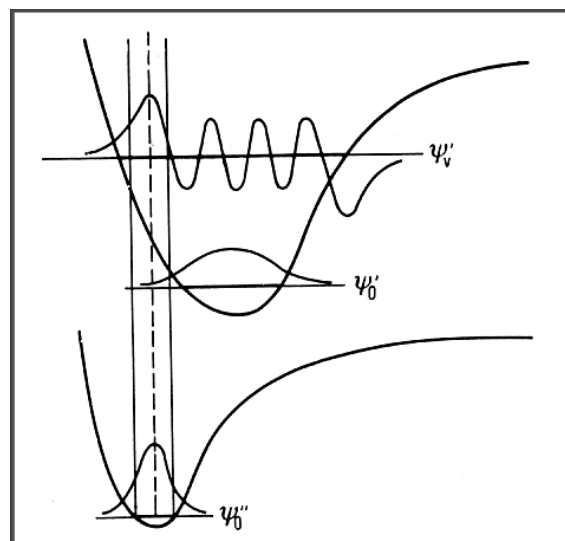


**Figure 2.7:** Illustration of the Franck-Condon-Principle. The transition probability is proportional to the wavefunction's overlap. For comparison, two vibrational states of the higher electronic level are shown. [8]

## 2.2.1   The Vibrational and Rotational Sub-Structure

Figure 2.6 is a depiction of the energy levels within electronic states. Nitrogen does not have a pure vibrational or rotational spectrum due to its symmetry, but in combination with an electronic transition, the vibrational and rotational state can change as well. Without these vibrational transitions, the spectrum would have only two lines corresponding to the 2P- and 1N-transition. But because of vibration there are many more band heads that include many rotational lines themselves. We can easily identify over 15 band heads, that are intense enough to be observed with the AIRFLY experiment.

**The Franck-Condon-Principle**

With the Franck-Condon-Principle, it is possible to derive transition probabilities, that define intensity ratios of band heads of the same initial state. The Franck-Condon-Principle is illustrated in Figure 2.7.

For the sake of simplicity rotation is neglected in the calculations of the Franck-Condon-Principle. The crucial assumption of the principle is, that the movement of the electrons is much faster than the nuclei's movement. This means, that an electronic transitions can be represented as vertical lines in Figure 2.7.

This is the reason, why the change of the wavefunctions does not have to be represented in Equation (2.14) to derive the transition matrix element $\mathcal{M}_{fi}$ of final and initial electronic states. Also, the Born-Oppenheimer approximation allows the wavefunctions, as functions of elec-

tronic coordinates $\mathbf{r}$ and internuclear distance $R$, of electron ($\phi$) and nucleus ($\chi$) to be separated [30]

$$
\begin{aligned}
\mathcal{M}_{if} &= \langle \Psi_f(\mathbf{r}, R) | \mathcal{M}(\mathbf{r}) | \Psi_i(\mathbf{r}, R) \rangle \\
&= \langle \phi_f(\mathbf{r}, R) \chi_f(R) | \mathcal{M}(\mathbf{r}) | \phi_i(\mathbf{r}, R) \chi_i(R) \rangle .
\end{aligned}
\tag{2.14}
$$

This can be separated in electronic and vibrational transition probabilities, using the r-centroid approximation [27], which is an expansion of the pure electronic transition moment in a power series of $R$. The internuclear distance $R_{\nu_i, \nu_f}$ of the transition is the first order approximation:

$$
R_{\nu_i, \nu_f} = \frac{\langle \chi_f(R) | R | \chi_i(R) \rangle}{\langle \chi_f(R) | \chi_i(R) \rangle} .
\tag{2.15}
$$

Now, with this first order approximation, the total transition probability separates like

$$
\underbrace{\langle \phi_f(\mathbf{r}, R_{\nu_i, \nu_f}) | \mathcal{M}(\mathbf{r}) | \phi_i(\mathbf{r}, R_{\nu_i, \nu_f}) \rangle}_{\text{electronic trans. prob.}} \cdot \underbrace{\langle \chi_f(R) | \chi_i(R) \rangle}_{\text{vibrational trans. prob.}} .
\tag{2.16}
$$

The square of the second integral is the Franck-Condon factor $q_{\nu_f, \nu_i}$ and depends on both initial and final vibrational states

$$
q_{\nu_f, \nu_i} = \langle \chi_f(R) | \chi_i(R) \rangle^2 = \left( \int \chi_f^*(R) \chi_i(R) dV \right)^2 .
\tag{2.17}
$$

The vibrational transition probability is proportional to the overlap of the corresponding vibrational wavefunctions that are centered around the internuclear distance of their electronic state (see Figure 2.7). With the introduced approximations, it is also possible, to calculate the total transition probabilities (or Einstein-coefficients $A_{\nu_i, \nu_f}$) as the squares of Equation (2.16). They were calculated in [27] and are stated in Table 2.1.

Since the population of the initial state is not known, the Einstein-coefficients can only be used to derive intensity ratios of band heads with the same initial state. These ratios do not depend on environmental parameters like pressure, so they can be used to improve the analysis later. Nevertheless, the relative position of the electronic potentials ($R_i < R_f$, $R_i > R_f$, $R_i \approx R_f$) has a great influence on these ratios, because their relative position defines where the overlap of wavefunctions is calculated.

For the rotational sub-structure a similar principle to the Franck-Condon-Principle can be formulated, which leads to Hönl-London factors. However, this more detailed treatment of the rotational substructure is not needed for this diploma thesis, because the rotational structure cannot be resolved by AIRFLY. The spectral lines are not symmetrical, but shaded towards smaller wavelengths (see Figure 2.1). This is an effect of the rotational transitions, that is explained by a model of R-, P- and Q-branches [8, 30], which depends again on the relative position of the electronic potential.

| $\lambda$ (nm) | System($\nu_i, \nu_f$) | $A_{\nu_i,\nu_f}$ ($10^6\,\mathrm{s}^{-1}$) | $\lambda$ (nm) | System($\nu_i, \nu_f$) | $A_{\nu_i,\nu_f}$ ($10^6\,\mathrm{s}^{-1}$) |
|---|---|---|---|---|---|
| 310.40 | 2P(4,3) | 3.02 | 358.21 | 1N(1,0) | 5.76 |
| †311.67 | 2P(3,2) | 5.94 | 364.17 | 2P(4,6) | 1.00 |
| †313.60 | 2P(2,1) | 10.1 | 367.19 | 2P(3,5) | 2.35 |
| †315.93 | 2P(1,0) | 11.9 | †371.05 | 2P(2,4) | 4.04 |
| 326.81 | 2P(4,4) | 3.71 | †375.54 | 2P(1,3) | 4.93 |
| †328.53 | 2P(3,3) | 2.85 | †380.49 | 2P(0,2) | 3.56 |
| 329.34 | 1N(4,2) | 3.19 | 385.79 | 2P(4,7) | 2.33 |
| 329.84 | 1N(3,1) | 2.08 | 385.79 | 1N(2,2) | 0.93 |
| 330.80 | 1N(2,0) | 0.90 | 388.43 | 1N(1,1) | 4.03 |
| †330.90 | 2P(2,2) | 0.80 | 389.46 | 2P(3,6) | 3.00 |
| †333.90 | 2P(1,1) | 0.59 | †391.44 | 1N(0,0) | 11.4 |
| †337.13 | 2P(0,0) | 13.1 | †394.30 | 2P(2,5) | 3.14 |
| 344.60 | 2P(4,5) | 0.12 | †399.84 | 2P(1,4) | 2.43 |
| †346.90 | 2P(3,4) | 0.12 | †405.94 | 2P(0,3) | 1.10 |
| †350.05 | 2P(2,3) | 1.71 | 409.48 | 2P(4,8) | 2.09 |
| 353.26 | 1N(5,4) | 6.63 | 414.18 | 2P(3,7) | 2.01 |
| †353.67 | 2P(1,2) | 5.54 | 416.68 | 1N(3,4) | 2.32 |
| 353.83 | 1N(4,3) | 7.46 | 419.91 | 1N(2,3) | 3.47 |
| 354.89 | 1N(3,2) | 8.09 | 420.05 | 2P(2,6) | 1.57 |
| 356.39 | 1N(2,1) | 7.88 | 423.65 | 1N(1,2) | 4.28 |
| †357.69 | 2P(0,1) | 8.84 | 427.81 | 1N(0,1) | 3.71 |

**Table 2.1:** Details on band heads of $N_2$ and $N_2^+$ between 300 nm and 430 nm. The analysis of this thesis includes transitions marked with "†". Given are their wavelength (from [56]), transition label and their Einstein-coefficients $A_{\nu_i,\nu_f}$ (from [27]).

## 2.2.2 The Spectrum

In Table 2.1 band heads of the spectrum are listed together with their wavelength, corresponding transition, and their Einstein-coefficients [27] that have only meaning within their band system. Band heads, that are intense enough to be analyzed in this thesis, are marked with "†".

The fluorescence spectrum recorded by AIRFLY is shown in Figure 2.8. It was recorded in dry air at a pressure of 800 hPa. The energy of the electrons used for excitation was 3 MeV. The band heads marked in Table 2.1 are labeled with the transition system and the respective vibrational quantum numbers. It can be seen, that the 2P(0,0)-transition is the most intense, and that the remaining background is very low. For comparison the fluorescence spectrum reported by Bunner [15] in 1967 is shown in the upper right corner.
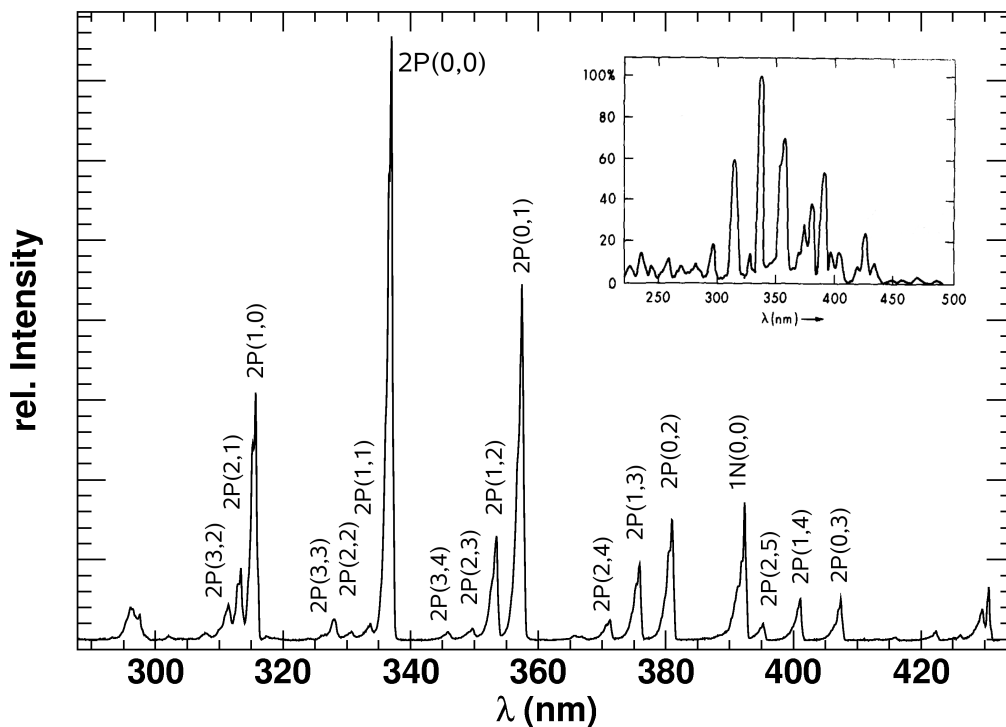
**Figure 2.8:** Fluorescence spectrum of air between 280 nm and 430 nm recorded by AIRFLY with transition labels. The gas was excited by 3 MeV electrons at a pressure of 800 hPa. In the right upper corner, the spectrum reported by Bunner (1967) is shown [15].

## 2.3 The Process and Yield of Fluorescence

In general, fluorescence is a form of luminescence. It is the emission of light from an excited atom or molecule, with a lifetime of the excited state around $10^{-8}$ s. Here, the molecule is nitrogen and it is excited via electron impact. The mechanism of this type of excitation has been the subject of several studies [5, 9, 12, 15, 21, 25, 26, 37, 69] that investigated the excitation cross section, and most of these studies also investigate the relaxation process (in particular [9, 16]). A summary of the current experimental status and theoretical considerations can be found in [41].

The following section gives a short overview on how nitrogen is excited and how it relaxes. Then a model of the fluorescence yield will be introduced that is used later in the analysis.

### 2.3.1 Excitation

Electrons that hit a gaseous target dissipate their energy by ionization according to the Bethe-Bloch formula. This can excite nitrogen to the $B^2\Sigma_u^+$ state of $N_2^+$ directly:

$$N_2(X^1\Sigma_g^+) + e \longrightarrow N_2^{+*}(B^2\Sigma_u^+) + 2e. \tag{2.18}$$
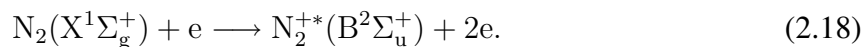
This produces additional secondary electrons with lower energy. The initial electronic state of the 2P-system cannot be excited by high energy (primary) electrons, because the molecule's

spin quantum number would have to change, which is not allowed in collisional excitation [15, 21, 41]. Thus, the excited state can only be reached by electron exchange and recombination of $N_2^+$:

$$N_2(X^1\Sigma_g^+) + e(\uparrow) \longrightarrow N_2^*(C^3\Pi_u) + e(\downarrow), \tag{2.19}$$

$$N_2^+ + e \longrightarrow N_2^*(C^3\Pi_u). \tag{2.20}$$
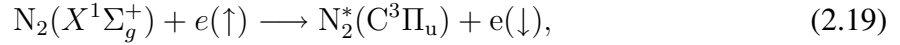
Both mechanisms require low energy electrons, that are mainly provided as secondaries of the direct excitation of the nitrogen ion (Equation (2.18)). Also, some ionization processes lead to the emission of Auger electrons, that can excite the nitrogen. But the cross section for this mechanism is two orders of magnitude lower than of those mentioned before.

It is assumed here, that these excitation mechanisms do not depend on temperature and are proportional to the energy deposit. Especially this proportionality to the deposited energy has to be confirmed by measurements.

Another possibility to feed an excited state is vibrational relaxation within the electronic state. The molecule relaxes, within the same electronic state, to the next lower vibrational level by collision [16]:

$$N_2(C^3\Pi_u)_{\nu=i} + N_2(X^1\Sigma_g^+)_{\nu=0} \longrightarrow N_2(C^3\Pi_u)_{\nu=i-1} + N_2^*(X^1\Sigma_g^+)_{\nu=0}. \tag{2.21}$$
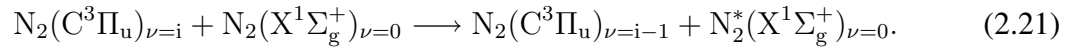
However, this works only by collision and the higher state can as easily decay to the ground state, and thus the process is negligible, as discussed in [55].

## 2.3.2 De-Excitation

There are two possible mechanisms for the excited molecules to relax, radiative transitions and collisional de-excitation called quenching. For the 2P-transitions they can be described as

$$N_2^*(C^3\Pi_u) \longrightarrow N_2(B^3\Pi_g) + h\nu, \tag{2.22}$$

$$N_2^*(C^3\Pi_u) + Q \longrightarrow \text{products}, \tag{2.23}$$
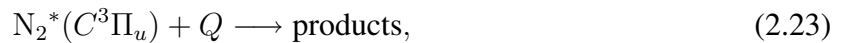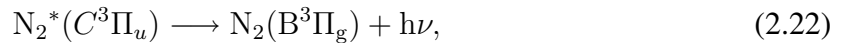
and for the 1N-transitions as

$$N_2^{+*}(B^2\Sigma_u^+) \longrightarrow N_2^+(X^2\Sigma_g^+) + h\nu, \tag{2.24}$$

$$N_2^{+*}(B^2\Sigma_u^+) + Q \longrightarrow \text{products}, \tag{2.25}$$
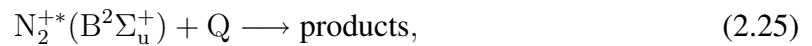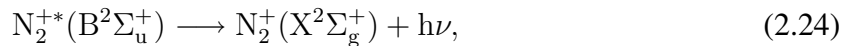
where Q is a collisional quenching partner.

Both processes can be described by simple decay laws, with lifetime $\tau_0$ for fluorescence and lifetime $\tau_q(p, T)$ for quenching, which depends on pressure and temperature,

$$\left(\frac{dN^*}{dt}\right)_{rad} = -\frac{1}{\tau_0} \cdot N^*, \tag{2.26a}$$

$$\left(\frac{dN^*}{dt}\right)_q = -\frac{1}{\tau_q(p, T)} \cdot N^*, \tag{2.26b}$$

with the number of excited molecules $N^*$. The reciprocal life time $\tau_0^{-1}(\nu_i, \nu_f)$ corresponds to Einstein-coefficients $A_{\nu_i, \nu_f}$ (see Table 2.1). It is important to note, that $\tau_0$ not only includes radiative decay, but all "internal" relaxation processes. It can therefore be written as

$$\frac{1}{\tau_0} = \frac{1}{\tau_{FL}} + \frac{1}{\tau_{iq}}, \tag{2.27}$$

with indices referring to fluorescence light emission and internal quenching.
Equations (2.26) can be combined to

$$\left(\frac{dN^*}{dt}\right)_{tot} = -\left(\frac{1}{\tau_q(p,T)} + \frac{1}{\tau_0}\right) \cdot N^*. \tag{2.28}$$

The quenching lifetime $\tau_q$ can be derived by gas kinetic theory to determine its dependence on pressure $p$ and temperature $T$ [15]. The reciprocal lifetime is equal to the collisional deactivation rate $R_c$ that can be expressed as a function of the molecule's relative velocity $v_{rel}$ between the collisional partners:

$$\frac{1}{\tau_q} = R_c = \frac{N}{V}\sigma(v_{rel})v_{rel}, \tag{2.29}$$

with the particle density $N/V$.
In the following, the collisional cross section $\sigma$ is assumed to be independent of temperature and energy, hence independent of velocity. The relative velocity of the molecules can be calculated with the Maxwell-Boltzmann distribution

$$f(\mathbf{v}) = \left(\frac{m}{2\pi kT}\right)^{\frac{3}{2}} \cdot e^{-\frac{m\mathbf{v}^2}{2kT}}. \tag{2.30}$$

Therefore a weighted integral over all velocities has to be calculated, in order to average over all relative velocities:

$$\langle R_c \rangle = \frac{N}{V}\sigma \iint v \cdot f(\mathbf{v}_1)f(\mathbf{v}_2)\, d^3v_1 d^3v_2. \tag{2.31}$$

This leads to an expression for the quenching lifetime between nitrogen and a quenching partner $Q_i$

$$\frac{1}{\tau_q} = p_i \cdot \sigma_i \cdot \sqrt{\frac{8}{\pi kT m_{N_2}} \cdot \frac{m_{N_2} + m_i}{m_i}}. \tag{2.32}$$

Here, the particle density was substituted by $p/kT$ according to the ideal gas law. $m$ denotes masses, $k$ is the Boltzmann-constant and $T$ the thermodynamic temperature. The relation simplifies even more, if a pure nitrogen target is assumed, where only nitrogen self-quenching ($\sigma_{N_2}$) occurs:

$$\frac{1}{\tau_q} = p \cdot \frac{4\sigma_{N_2}}{\sqrt{\pi kT m_{N_2}}}. \tag{2.33}$$

For the later analysis, it is convenient to define another parameter, the reference pressure $p'$. It is defined as the pressure, at which the quenching lifetime equals the radiative lifetime

$$\tau_q|_{p=p'} = \tau_0. \tag{2.34}$$

For pure nitrogen, this leads to

$$p'_{N_2} = \frac{\sqrt{\pi k T m_{N_2}}}{4\sigma_{N_2}\tau_0} \quad \propto \frac{\sqrt{T}}{\sigma_{N_2}}. \tag{2.35}$$

Since collisional cross sections in mixtures can be expressed as a sum of their single contributions, reference pressures, too, are additive. They can be added for mixtures, but have to be weighted by the proportions of the components $f_i$ and, in the formulation of above, a factor for mass-correction $\widehat{m}_i$ has to be used. Thus, the reference pressure of air (mixture of 79% nitrogen and 21% oxygen) can be derived as

$$\frac{1}{p'_{Air}} = \frac{0.79}{p'_{N_2}} + \widehat{m}_{O_2}\frac{0.21}{p'_{O_2}}, \tag{2.36}$$

with

$$\widehat{m}_{O_2} = \sqrt{\frac{m_{N_2} + m_{O_2}}{2m_{O_2}}}, \quad p'_{O_2} = \frac{\sqrt{\pi k T m_{N_2}}}{4\sigma_{O_2}\tau_0}. \tag{2.37}$$

Here, $\sigma_{O_2}$ denotes the nitrogen-oxygen collisional cross section. The parameter $p'_{O_2}$ has, strictly speaking, no physical meaning, since it corresponds to the nitrogen-oxygen quenching in a gas mixture without nitrogen. Nevertheless, this new quantity of the reference pressure of oxygen is very usefull in the later analysis, since it can be used to decouple the reference pressures of nitrogen and air, and thus enhances the analysis.

### 2.3.3 The Fluorescence Yield

The fluorescence yield $Y$ is the number of photons produced by one electron per 1 m of pathlength. The unit of the fluorescence yield, [photons/m], has practical reasons and was introduced by the first collaboration that needed to use the fluorescence yield for air shower measurements. The fluorescence yield is defined here in this unit.

In order to get a hold on the fluorescence yield, another quantity, the fluorescence efficiency $\Phi$ has to be defined, first. The fluorescence efficiency is the ratio of radiated energy to deposited energy at a given wavelength

$$\Phi_\lambda = \frac{\text{radiated energy}}{\text{deposited energy}} = \frac{n_\lambda \cdot E_\lambda}{E_{dep}}, \tag{2.38}$$

with number of emitted photons $n_\lambda$. If the number of excited molecules is proportional to the deposited energy, the fluorescence efficiency can also be formulated using the decay lifetimes. It reads then

$$\Phi_\lambda = \frac{\frac{1}{\tau_{FL}}}{\frac{1}{\tau_0} + \frac{1}{\tau_q}}. \tag{2.39}$$

This can be reformulated by using the reference pressure $p'$ and defining the pure fluorescence efficiency $\Phi_\lambda^0 = \tau_0/\tau_{FL}$, at wavelength $\lambda$ without quenching, and can then be combined with Equation (2.38)

$$\Phi_\lambda = \frac{\Phi_\lambda^0}{1 + \frac{p}{p'}} = \frac{n_\lambda \cdot E_\lambda}{n_e \cdot \frac{dE}{dX}\rho\Delta x}. \tag{2.40}$$

Here, $n_e$ is the number of electrons and $\frac{dE}{dX}\rho\Delta x$ the deposited energy of one electron according to the Bethe-Bloch equation along a path of length $\Delta x$ in a gaseous medium of density $\rho$.
The fluorescence yield can now be determined by solving Equation (2.40) for the number of emitted photons $n_\lambda$ per electron and pathlength. For the sake of clarity, all constant factors are merged into $C_\lambda$, but since the density $\rho$ depends on pressure, this factor $p$ is excluded from $C_\lambda$. Thus the fluorescence yield $Y$ can be expressed as

$$Y = Y(\lambda, p, T, \sigma) = \frac{n_\lambda}{n_e \cdot \Delta x} = \frac{C_\lambda \cdot p}{1 + \frac{p}{p'}}. \tag{2.41}$$

The pressure dependence can be seen explicitly and the dependence on temperature is included in the $p'$-factor that is proportional to $\sqrt{T}$. The influence of the gas composition is also hidden in the reference pressure, since it depends on the total collisional cross section $\sigma$. The wavelength dependence can be found in $C_\lambda$ or $\Phi_\lambda$ and is reflected in the fluorescence spectrum, because the intensity of the lines is proportional to the fluorescence efficiency. Furthermore, the reference pressure $p'$ is the same for all lines that belong to the same band system, since their intensity ratios do not change, which means that they have to depend in the same way on pressure.
In this thesis the fluorescence yield is always, unless explicitly mentioned, defined in units of

$$\left[\frac{\text{photons}}{\text{m}}\right].$$

Some authors use $\left[\frac{\text{photons}}{\text{MeV}}\right]$ as unit. They are related through the energy deposit per pathlength $\frac{dE}{dX}\rho$:

$$Y\left[\frac{\text{photons}}{\text{m}}\right] = Y\left[\frac{\text{photons}}{\text{MeV}}\right] \cdot \frac{dE}{dX}\rho. \tag{2.42}$$

### 2.3.4   The Effect of Argon and Water Vapor

After nitrogen and oxygen, argon is the most common component of air with a relative abundance of 1%. It is therefore the only additional air-component, whose effect on the fluorescence yield cannot be, a priori, assumed to be negligible.
Argon is on the one hand a quenching partner, and on the other hand a source of secondary electrons, that can excite nitrogen. These effects are expected to be at the 1% level, but should almost cancel for the 2P system. Thus, if the effects are significant, they are expected to affect the 1N(0,0)-transition most, because its upper state is excited by primary electrons, thus the quenching effect should be dominating. An early but elaborate study of the effects of argon is [29].
Like the effect of argon, the effect of water vapor has to be studied. It is believed, that a relative humidity of 100% at sea level has a supressing effect of 20% on the fluorescence yield. Some experiments have already given first results on investigations of the water vapor effect [14, 48, 55, 69].
AIRFLY will look for the effects of argon by means of a comparison of measurements in air and air mingled with 1% argon. Measurements of AIRFLY are carried out without water vapor or at

constant relative humidity, but measurements to determine the effect are planed.

The next chapter will introduce the experimental setup of AIRFLY and will be followed by the analysis carried out for this diploma thesis. The goal of AIRFLY is the quantitative determination of all dependencies of the air fluorescence yield on environmental parameters. This includes pressure, temperature and energy of the exciting particles. The spectral distribution of the fluorescence light will be investigated, as well as the effect of argon and water vapor as additional compositions to the gas mixture.
The specific aims of this diploma dissertation are to determine the pressure dependence of all visible band systems of the fluorescence spectrum of air between 300 nm and 410 nm, to determine intensity ratios of the individual spectral lines, to check the proportionality of the fluorescence yield to the deposited energy, and to look for the effect of argon.

# CHAPTER 3

# THE AIRFLY EXPERIMENT

In 1967 Bunner investigated the fluorescence technique for the detection of ultra high energy cosmic rays [15]. Since then, the fluorescence emission of nitrogen was subject of many studies, not only by groups dealing with the detection of cosmic rays (like [39]). Also, chemical physics groups (for instance [55]), and even groups interested in excimer lasers (i.e. [48]) measured the nitrogen fluorescence yield. Recent results about the fluorescence yield of astroparticle physics related groups can be found in [17, 45, 49, 50, 69], as well as a detailed summary in [41].

Currently, the Pierre Auger Observatory uses the results of Nagano et al. [50] for its reconstruction of the primary energy of cosmic rays. But, despite the effort, the uncertainty of the fluorescence yield is still the largest contribution to the uncertainty of the energy reconstruction (see table 1.1). That is the motivation for yet another laboratory experiment to determine the fluorescence yield: The AIRFLY experiment (**Air Fl**uorescence **Y**ield).

The strategy of determination is threefold and uses relative measurements as far as possible to reduce systematic uncertainties:

- Relative measurement of the 2P(0,0)-transition at 337 nm with a PMT.

- Relative measurement of the fluorescence spectrum.

- Absolute end-to-end calibration of the PMT setup with Cherenkov light.

These measurements are conducted at variable pressure, electron energy, temperature and humidity. Since the data is not complete yet, the scope of this diploma thesis is restricted to the pressure and energy dependence of the fluorescence yield. Therefore, the experimental setup is only explained as far as necessary for this work.

## 3.1   Experimental Setup

AIRFLY is a thin target experiment, and thus, the energy of the electrons, used to produce fluorescence light, can be assumed to be constant in the volume of the experiment's chamber. The fluorescence light is observed perpendicular to the beam axis, because it is emitted in all directions, contrary to Cherenkov light or transition radiation that is emitted along the axis.
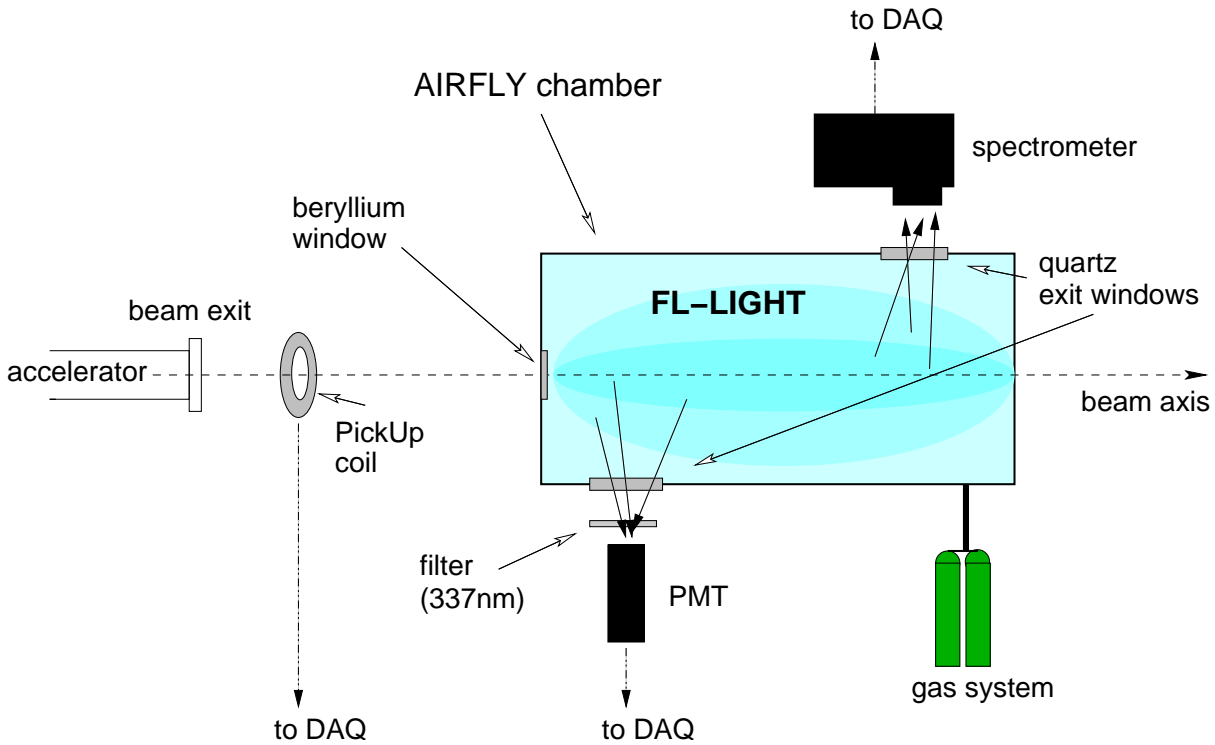
**Figure 3.1:** Scheme of AIRFLY's setup. The important components are the accelerator, chamber, gas system and measuring devices (Pick-up coil, PMT and spectrometer). Also the PMT and the spectrometer do not measure simultaneously.

This thesis includes measurements taken at the Argonne National Laboratory (ANL) [44], near Chicago (USA), at three different accelerators. Additionally, there have been measurements at the $DA\Phi NE$ Test Beam Facility in Frascati (Italy), that are not considered here, since they are analyzed elsewhere [4].

Figure 3.1 illustrates the setup of the AIRFLY experiment and labels all important parts, that are described in the next sections.

### 3.1.1 The Accelerators

AIRFLY uses three accelerators at the ANL, that cover different energy regions and use different techniques.

**The Advanced Photon Source (APS)** uses 7 GeV electrons in a storage ring as a X-ray source. These photons produce a very stable electron beam in the keV region due to the photoelectric effect. The electrons are then used to measure the fluorescence spectrum.

**The Van-de-Graaff (VdG)** is a linear accelerator, that uses an electrostatic generator to build up voltage. The VdG at the ANL is designed for energies of 1-3 MeV, and can be operated in continuous or pulsed mode. For AIRFLY the pulsed mode was used with $\approx 10^{10}$ e$^-$/bunch (a few $10^{-9}$ Coulomb) at a rate of 50 Hz. The beam spot is relatively large
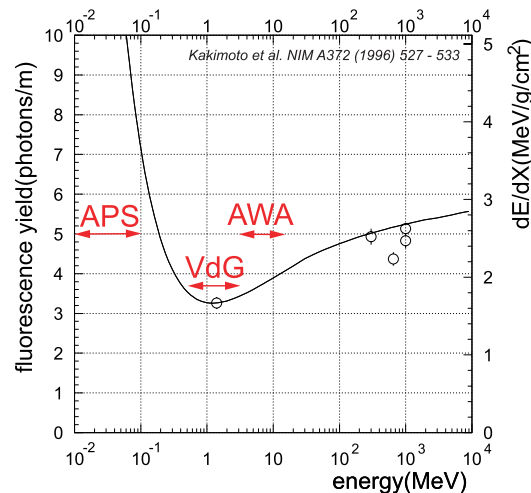
**Figure 3.2:** Illustration of the energy ranges of the three accelerators used by AIRFLY, marked with red arrows. The data points show the results for the air fluorescence yield of Kakimoto et al. [39]

and oscillates within the beam exit window. The beam quality is good enough for the spectrometer, but PMT measurements have to be treated very carefully.

**The Advanced Wakefield Accelerator (AWA)** is a special type of linear accelerator, that utilizes a low-energy electron beam to accelerate a second beam called "witness beam". This beam rides on the low-energy electron's wake. The AWA has a range in energy of 3-15 MeV and operates at 2 Hz.

Figure 3.2 shows the energy ranges of the accelerators in a plot of the results for the air fluorescence yield of Kakimoto et al. [39], which are compared to the Bethe-Bloch function. One of AIRFLY's aim is to check the energy dependence of the fluorescence yield over the range marked.

## 3.1.2   The AIRFLY Chamber

The volume, in which the measured fluorescence light is produced, is defined by the AIRFLY chamber. It is made of 3 mm thick, black painted aluminum. The chamber is cylindrical in shape, 200 mm in diameter and 400 mm in length along the beam axis. At the entrance and exit 0.5 mm thick beryllium windows are placed. At each side are two quartz windows to allow light detectors to be placed perpendicular to the beam axis. On top of the chamber sensors for pressure, humidity and temperature can be inserted, and an aluminum cap holds a mirror, that can be lowered into the chamber for Cherenkov-light measurements. For some measurements with the spectrometer another mirror could be placed at the opposite side of the beam, in order to catch more light with the spectrometer. For photographs of the chamber see Figure 3.3.
The Cherenkov mirror consists of a 1.5 $\mu$m thin aluminized mylar foil that is applied to a thick support. It has a reflectivity of 83%. The gas system can be remotely controlled and allows,

(a) Alignment of beam and PMT at AWA without chamber.
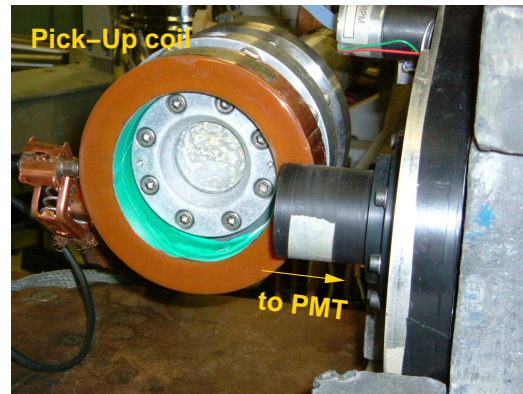


(b) Pick-Up coil at the beam exit at the Van-de-Graaff accelerator.
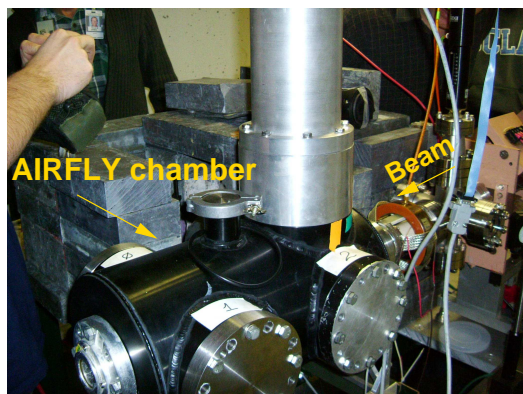


(c) AIRFLY chamber at AWA.
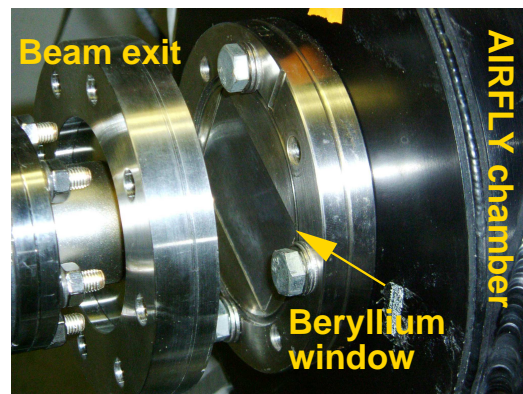


(d) Entrance window of the chamber in front of beam exit.

**Figure 3.3:** Photos of AIRFLY, taken during the measurements in February and July 2006.

together with a Leybold Capacitron DM 21 pressure gauge, a precise adjustment of pressure inside the chamber within $\approx 0.5$ hPa.

Both nitrogen and dry air (with or without argon) was used in a pressure range of 4-1000 hPa. Dry air denotes a mixture of nitrogen and oxygen (79%:21%), that could be mingled with 1% argon (i.e. 78%$N_2$:21%$O_2$:1%Ar). Measurements conducted without chamber used the natural air of the laboratory. In the following the artificial mixtures used will be referred to as "air" or "air with argon" respectively.

### 3.1.3  Measuring Devices

AIRFLY's measuring devices consist of a spectrometer and a photomultiplier to observe the emitted fluorescence light, as well as a Pick-up coil and a Faraday cup to monitor the number of electrons per bunch. Photographs of the setup, showing the Pick-up coil, are given in Figure 3.3.

At APS and VdG the spectrometer was used. It is an Oriel spectrograph MS 257 with a focal length of 25.7 cm. It has a resolution in wavelength of $\approx 0.1$ nm and is equipped with

an Andor CCD chip (DV 420), that has $1024 \times 256$ active pixels. The spectrometer is favored, because a monochromator would be sensitive to changes of beam intensity or position.

The dynamic range of the spectrometer is too small to cover the whole range of 280-430 nm, so the spectrum is recorded in two parts, from 280-370 nm and 340-430 nm. The spectrometer's alignment varied slightly at the accelerators and it was used with and without the chamber, the later could be equipped with a collecting mirror and optical fibers. For all these cases calibration measurements have been performed. For the absolute wavelength calibration a mercury pencil lamp from Oriel was used [63]. The intensity calibration was accomplished relative to a NIST traceable calibrated xenon lamp from Hamamatsu.

The photomultiplier was used at VdG and AWA. It is a Hamamatsu H7195P model and was chosen for low background. It has a bialkali photocatode with a diameter of 46 mm and a peak sensitivity at 420 nm. The bialkali catode has a quantum efficiency at 337 nm of about 8% and a very low dark current.

The alignment of the PMT also varied, because it was used at different locations and for energy dependence measurements without the chamber. Due to different distances of the PMT to the beam, the field of view changed as well. However, for the relative analysis performed in this thesis these scan-to-scan differences are of no importance. But it is crucial, to monitor the photomultiplier's gain throughout each measurement, which was done with the signal of a precise LED.

The interference filter, used to delimit the wavelength region of the light reaching the PMT, has a peak transmission of about 50% at 340 nm and a width of 10 nm (FWHM). With this filter, the light reaching the PMT originates to 98.3% from the 2P(0,0)-transition at 337 nm. The filter's transmission curve is shown in Figure 3.4. During the measurements, the spectrometer and the PMT were shielded with lead bricks to reduce background.

For the analysis of the spectrometer measurements, it is not required to know by how many electrons the light was produced. For the PMT measurements, however, the information about the number of electrons is needed. Therefore, a Pick-up coil was placed around the beam. The bunches of electrons traverse the coil and induce a current proportional to the charge of the bunch.

The Pick-up coil was monitored by a Faraday cup that was placed in front of the beam exit. The Faraday cup collects all electrons of the beam, producing a current that is proportional to the number of collected electrons. Since the Faraday cup absorbs all the electrons, it could not be used in the actual measurements, but it was used to check the linearity of the Pick-up coil.

The signal of the Pick-up coil was a linear function of the Faraday cup signal, indicating that the Pick-up coil was mounted correctly and giving a proper signal. An example yields Figure 3.5. Of course, the Pick-up signal is only a relative measurement.

All the signals of the PMT, Pick-up coil, and Faraday cup have been integrated within a gate signal of 100 ns and recorded as ADC signals. ADC denotes an analog to digital conversion, at which every integrated signal is converted to a digital integer value and stored in an ASCII data
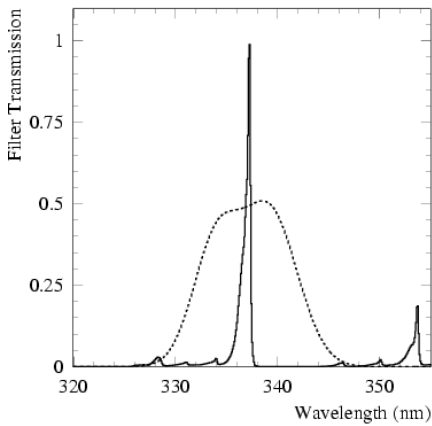
**Figure 3.4:** Transmission curve (dotted) of the interference filter at the 337 nm line (solid). Impurities of the 2P(0,0) band head amount to 1.7% within the filter range.
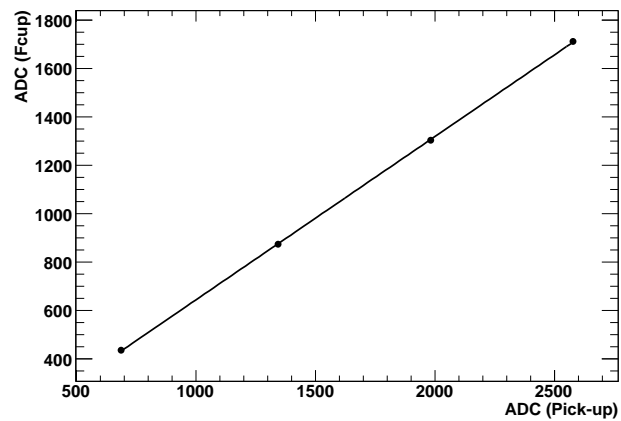
**Figure 3.5:** Plot of Faraday cup signal ($ADC_{Fcup}$) over Pick-up signal ($ADC_{Pick-up}$). The linearity assures a proper function of the Pick-up coil (see text).

file for later analysis.

## 3.2   Agenda of Measurements

The AIRFLY experiment began measurements in 2003 at $DA\Phi NE$ in Frascati (Italy). These measurements are analyzed elsewhere [4] and are not regarded in the extent of this diploma thesis.

In 2005, AIRFLY moved to ANL nearby Chicago (USA) and conducted measurements at the accelerators mentioned in Section 3.1.1. They were performed in July and October 2005, as well as in February, July, and September 2006.

The following measurements were performed at a temperature of 293 K:

- PMT-scans (only 337 nm line)

  - at different energies, without chamber (laboratory air).

  - at different pressures for nitrogen, "air", and "air with argon".

  - for different mixtures of nitrogen and oxygen.

  - with Cherenkov mirror in Freon12 gas for calibration.

- Spectrometer-scans

  - at different pressures for "air" and "air with argon".

  - at constant pressure for nitrogen, laboratory air, "air", and "air with argon".
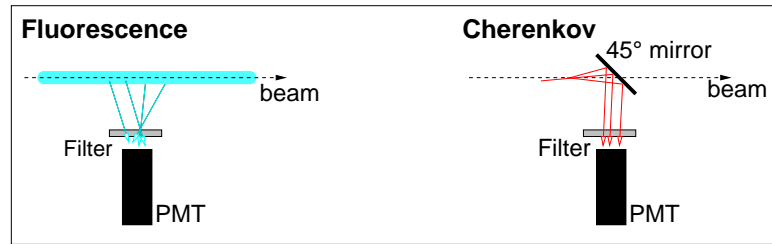
**Figure 3.6:** A comparison of fluorescence and Cherenkov measurements. The Cherenkov light is emitted along the beam axis and must be reflected into the PMT, whereas the fluorescence light is emitted isotropically around the beam axis.

Relative measurements are used as far as possible. All spectrometer data are analyzed relative to the 2P(0,0) band head at 337 nm. Thus, only a relative calibration of the spectrum is needed, and the pressure dependence of the fluorescence yield (i.e. the reference pressure $p'$) can even be determined with an uncalibrated spectrum. Of course, the reference pressure $p'$ of the 2P(0,0)-transition has to be calculated first. This can be done with uncalibrated PMT measurements. Since $p'$ depends on the collisional cross sections $\sigma_i$ of the gas components, these can also be deduced, if the lifetime $\tau_0$ of the transition is known (see Equation (2.35)).

During each measurement, the photomultiplier's gain was monitored with the signal of an LED, and a measurement of the background was performed with a closed shutter in front of the PMT. An absolute calibration of the PMT is needed to determine the pure fluorescence efficiency $\Phi_{337}^0$ (Equation (2.40)) or the factor $C_{337}$ of Equation (2.41) of the 2P(0,0)-transition. With the factor $C_{337}$ and the relative spectra, all factors $C_\lambda$ can be derived.

The strategy to obtain an absolute end-to-end calibration is to compare the fluorescence signal to the signal of a well known process. In this case, the process is the emission of Cherenkov light, whose intensity and spectral distribution can be calculated very precisely. Therefore, as Figure 3.6 shows, a mirror has to be lowered into the chamber to reflect the light into the PMT. For these measurements, Freon12 was used instead of air, since the threshold energy of Cherenkov light production in air cannot be reached by the accelerators at ANL. The background due to fluorescence and transition radiation can be neglected, because of its very low intensity compared to the Cherenkov light.

However, there are other considerable difficulties, like the simulation of geometrical effects and multiple scattering in the field of view. This leaves the analysis of the data of the absolute calibration too time-consuming to be accomplished within the limitations of this diploma thesis.

In Figure 3.7, the measurements and their connections are shown graphically. This thesis covers the analysis of the data as indicated by solid frames and arrows.
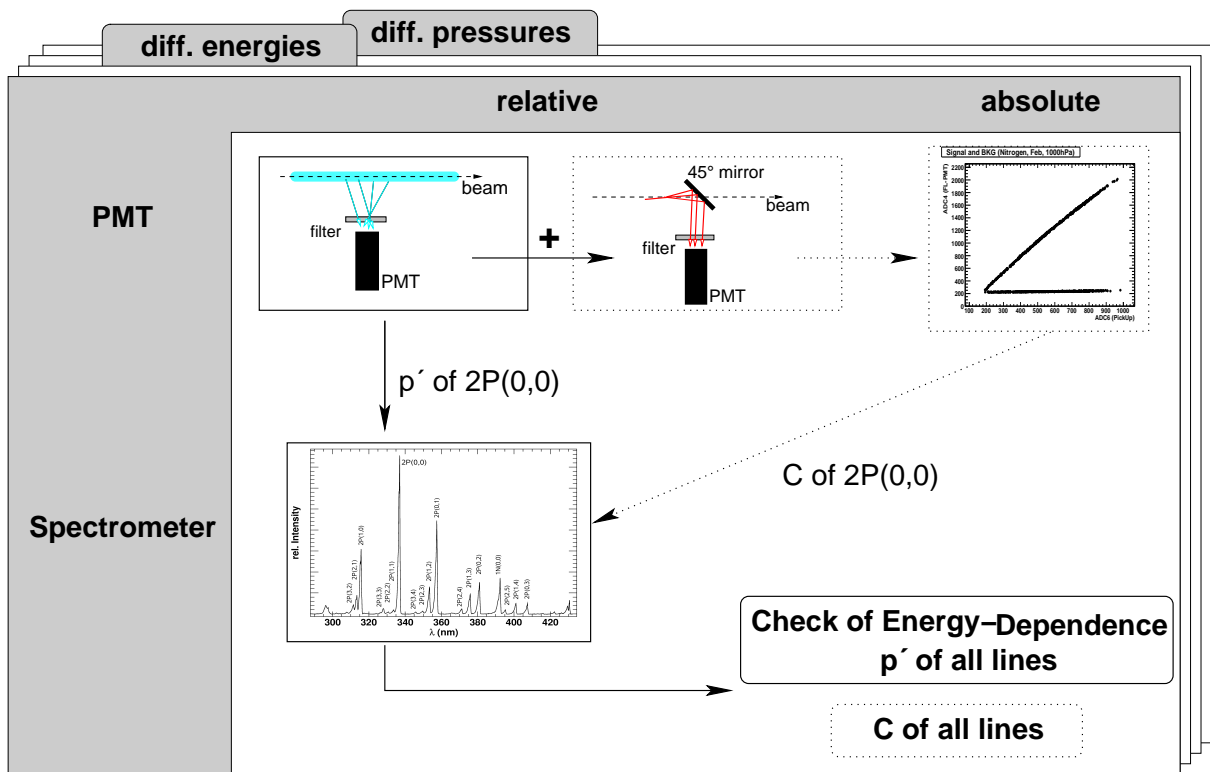
**Figure 3.7:** Diagram of the different kinds of measurements, that have been conducted at various pressures and energies, and their interplay. The scope of this thesis includes the part indicated with solid frames and arrows.

# CHAPTER 4

# THE FLUORESCENCE YIELD OF THE 2P(0,0)-TRANSITION

In this chapter, the analysis of the photomultiplier measurements will be presented. The first part shows the connection of the fluorescence yield to the observed quantities, which will lead to restrictions for the choice of data. The ratio method used to determine the reference pressure is introduced, after a Stern-Volmer analysis has been performed. This will be followed by a discussion of the results obtained.

Thereafter, measurements will be analyzed to investigate the energy dependence of the fluorescence yield. The results obtained with the Pick-up coil and the Faraday cup will be discussed.

## 4.1 An Estimator for the Fluorescence Yield

In a fixed volume the fluorescence yield $Y$ is proportional to the ratio of emitted photons to the number of exciting electrons. These are measured with the photomultiplier and the Pick-up coil respectively:

$$Y \propto \frac{\text{number of photons}}{\text{number of electrons}} = \frac{\text{ADC}_{\text{PMT}}}{\text{ADC}_{\text{Pick-up}}}. \tag{4.1}$$

This equation holds true in an ideal case, only. Because the ADC values are afflicted with pedestals and background, Equation (4.1) has to be reformulated to

$$\text{ADC}_{\text{PMT}} = \text{S}_{\text{FL}} \cdot \text{ADC}_{\text{Pick-up}} + \text{b}. \tag{4.2}$$

The summand $b$ depends on background and pedestals of Pick-up and PMT, while $S_{FL}$ does not. $S_{FL}$ is proportional to the fluorescence yield, and can thus be used as an estimator for $Y$. With this result and Equation 2.41, the data has to be compared to

$$S_{FL} = C^* \cdot \frac{p}{1 + \frac{p}{p'}}, \tag{4.3}$$

with $C^* \propto C$ (Equation 2.41), as long as a constant volume can be assumed.

The constant volume does not refer to the AIRFLY chamber, but to the observed volume depending on the field of view of the PMT. At high pressures, all secondary electrons, produced by the

interactions of high energy primary electrons with nitrogen (see Section 2.3.1), dissipate their
energy in the field of view. At low pressures, some of them may escape and carry energy out of
the observable volume. This leads to an underestimation of the fluorescence yield. Therefore a
correction function has to be introduced to the model

$$S_{FL} = C^* \cdot \frac{p}{1 + \frac{p}{p'}} \cdot F(p). \tag{4.4}$$

For the alignment of the PMT used at the AWA accelerator, this function $F(p)$ was determined
with a Monte Carlo simulation [59]. The simulation yields

$$F(p) = \left(\frac{p}{1000}\right)^{0.027}, \tag{4.5}$$

with pressure $p$ given in hPa. This amounts to a 10% effect at a pressure of 20 hPa.
In order to determine the reference pressure $p'$, only the relative parameter $S_{FL}$ is needed, given
as the slope of $\mathrm{ADC_{PMT}}$ over $\mathrm{ADC_{Pick-up}}$. To determine $C$, or the pure fluorescence efficiency
$\Phi^0$, an absolute calibration is needed to get the numbers of photons and electrons:

$$\mathrm{ADC_{PMT}} \xrightarrow{\text{Cherenkov calib.}} \text{number of photons} \tag{4.6}$$

$$\mathrm{ADC_{Pick-up}} \xrightarrow{\text{Pick-up calib.}} \text{number of electrons.} \tag{4.7}$$

However, these calibrations are beyond the scope of this diploma dissertation.
The need for a precise determination of $S_{FL}$ yields some restrictions to the data samples that
could be used. This is the issue of the first part of the next section.

## 4.2 Pressure Dependence of the Yield

### 4.2.1 Choice of Data Sample

The photomultiplier was mounted for pressure scans with the AIRFLY chamber at the Advanced
Wakefield and the Van de Graaff accelerators. A slight change in alignment could not be avoided
when the equipment was moved, but this does not affect the relative measurements. Figure 4.1
shows typical measurements at the different accelerators as scatter plots. Each point corre-
sponds to one measured event, with the Pick-up and PMT signals on x- and y-axis respectively.
The slope of the resulting line is proportional to the fluorescence yield. Each run consists of
5000 events at VdG and of 500 events at AWA. Despite the large number of data points a linear
fit to the VdG data is not exact enough, because the fitrange is too small and the points are sig-
nificantly smeared out. Especially at low pressures the uncertainty of the slope, resulting from
a linear fit to the VdG data is high.
Annother approach to find $S_{FL}$ is to average all events into one data point (red point in Fig-
ure 4.1(a)), subtract all background, and calculate the slope of the resulting line through origin.
This calculation is also not accurate, because of the beam quality. The VdG beam is not very
stable, which causes pedestal shifts in the Pick-up coil and changes of the beam position in
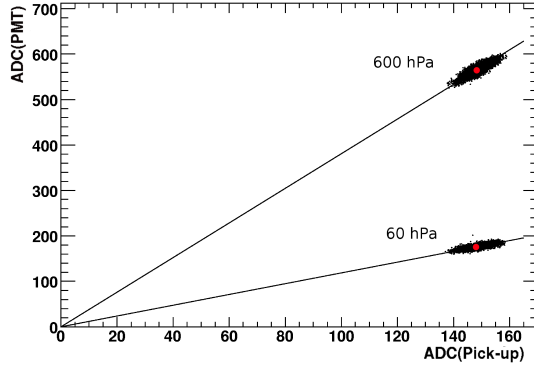
(a) Typical measurement at VdG with line through origin and center of scatter plot (red point).
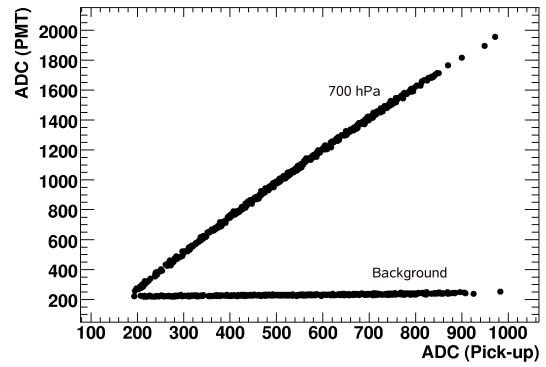


(b) Typical measurement at AWA (signal and background).

**Figure 4.1:** Scatter plots of $\mathrm{ADC_{PMT}}$ over $\mathrm{ADC_{Pick-up}}$ of measurements at VdG and AWA. The linear dependence of the number of photons to the number of electrons is clearly visible, as well as the differences of the data sets. At VdG more data points are recorded, but at AWA the measurement covers a larger range on the Pick-up axis. The slope of the background measurements (shown for AWA), recorded with closed PMT shutter, is very small.

| ID | date | gas |
|----|------|-----|
| 1 | February $16^{th}$ 2006 | "Air" |
| 2 | February $17^{th}$ 2006 | "Air with Ar" |
| 3 | February $17^{th}$ 2006 | Nitrogen |

**Table 4.1:** List of AWA pressure measurements. Later, they may be referred to by their ID number. "Air" corresponds to a mixture of nitrogen and oxygen (79%:21%), "Air with Ar" to a mixture of nitrogen, oxygen and argon (78%:21%:1%). Measurements were conducted at a Temperature of 293 K and electron energy of 14 MeV.

the PMT's field of view. These beam properties add systematic uncertainties, that cannot be reduced by analytic means due to an insufficient ability to monitor the beam. An analysis of the VdG data yielded differences in the obtained reference pressures of up to 200%, due to the reasons mentioned beforehand.

The beam of the Advanced Wakefield Accelerator is much more stable, can be better adjusted and monitored, and allows a wider range in electron bunch size. Although the number of data points is only a tenth compared to VdG measurements, the eight times larger fitrange allows a determination of the slope $S_{FL}$ by a linear fit.

Therefore, only pressure scans performed at AWA are considered to determine the reference pressure of the 2P(0,0)-transition. They are listed in Table 4.1. All PMT measurements conducted at the VdG are rejected, including measurements of varying nitrogen-oxygen mixtures. The chosen measurements are now analyzed in two steps. First, $S_{FL}$ is determined as the slope of $\mathrm{ADC_{PMT}}$ over $\mathrm{ADC_{Pick-up}}$ scatter plots. Second, these estimators of the fluorescence yield are plotted as a function of pressure, using their ratios to account for effects due to escaping

secondary electrons.

## 4.2.2 Determination of $S_{FL}$

In order to get the slopes $S_{FL}$, the scatter plots of ADC counts have been transformed to histograms with a bin width of four counts. Since the ADC counts are integers, there are always four ADC counts of the Pick-up coil that belong to the same bin. This binning was found by studying its effect on the $\chi^2$-distribution of the linear fit. Above a bin width of four, its increase does not reduce the mean of the $\chi^2$-distribution of all fit results. This implies, that the uncertainty of the Pick-up measurements is not greater than four counts, and that each bin has enough entries that the analysis is not biased [18].

Since there are still, by chance, bins with only one single entry, and therefore without error (of the mean), such bins have been assigned the biggest error of the other bins to avoid a bias to the fit. The error of the mean (RMS/$\sqrt{N}$) in each bin was preferred to Poisson-like errors ($\sqrt{N}$), because the spread of the $\mathrm{ADC_{PMT}}$ versus $\mathrm{ADC_{Pick-up}}$ distribution does not increase with $\mathrm{ADC_{Pick-up}}$. Figure 4.2 shows a histogram of measurement 1 at 180 hPa. The line represents the fit result over the whole range.

The fit was performed as a $\chi^2$ minimization, done with Minuit [38] used within the ROOT framework (v. 5.08) [13]. The minimization used a simplex minimization first, to find good starting values for the gradient minimization, that was used to find the minimum. The parameter uncertainties have been found thereafter with the $\chi^2 + 1$-contours. All these functions are part of the Minuit package [38].

This way, all signal and background measurements have been analyzed. In the following, $S_{FL}$ always refers to the background subtracted signal.

The slopes are accurate with an uncertainty smaller than 0.1%. However, due to a slight curvature at high Pick-up values, it seems necessary to apply the fit only to the lower part of the data points (2/3 of the full range). This reduced range increases the relative uncertainty to about 1%, but excludes effects due to saturated devices or beam instabilities at high currents. The small curvature, that is sometimes observed, is not always bent in the same direction, which indicates deficiencies in the measuring devices rather than a physical effect like electron-electron interaction.

## 4.2.3 The Stern-Volmer Kinetics

The de-excitation of nitrogen follows the so-called Stern-Volmer kinetics, since it is composed of two independent de-excitation processes, one of which depends on pressure. Thus, the inverse de-excitation yield is proportional to pressure $p$. In the case of nitrogen, excited by electrons, the de-excitation yield $Y_{de-ex}$ is given by

$$Y_{de-ex} \propto \frac{Y}{p} \propto \frac{S_{FL}}{p}, \tag{4.8}$$

with the fluorescence yield $Y$. Since the excitation is proportional to the energy deposit, which itself is proportional to pressure $p$, the fluorescence yield has to be divided by pressure to get
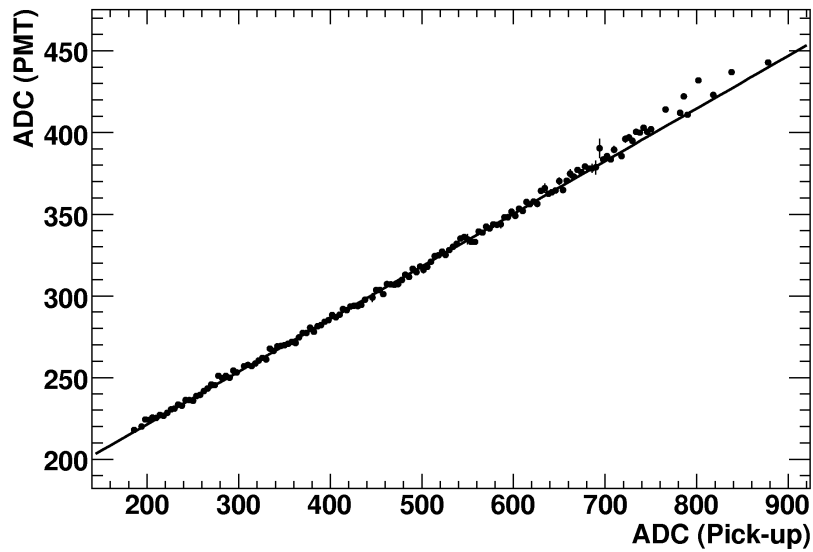
**Figure 4.2:** Histogram of photomultiplier signal as a function of pick-up signal at 180 hPa with bin width 4. The line represents the best fit over full range.

| ID | gas | $p'$ (hPa) | uncertainty (hPa) |
|:---:|:---:|:---:|:---:|
| 1 | "Air" | 16.8 | 1.2 |
| 2 | "Air with Ar" | 14.1 | 2.7 |
| 3 | Nitrogen | 100.7 | 3.2 |

**Table 4.2:** Reference pressures, determined without correction for escaping secondary electrons.

the de-excitation yield. The Stern-Volmer shape of this expression follows with Equation (4.3)

$$\frac{1}{Y_{de-ex}} \propto \frac{p}{S_{FL}} = \frac{1}{C^*} + \frac{1}{C^*p'} \cdot p. \tag{4.9}$$

A typical Stern-Volmer plot is shown in Figure 4.3. The line corresponds to a fit yielding the reference pressure $p'$ as parameter according to Equation (4.9).

At high pressure the function is linear, suggesting that there are no three-body deactivation mechanisms observed. Such mechanisms would cause a quadratic development of the relative yield with pressure in a Stern-Volmer plot [47]. At low pressures, deviations from linearity can be seen. These are due to secondary electrons that leave the field of view. A correction for this was introduced in Section 4.1.

Without this correction an analysis of the Stern-Volmer plots above 30 hPa yields values for the reference pressures of the gases used, as stated in Table 4.2. The errors are statistical only. To avoid a too large bias by escaping secondary electrons the fitrange was chosen to be 30-1000 hPa. The reference pressures $p'$ of "air" and "air with argon" do agree within their uncertainties. However, an analysis that includes a correction at low pressures is needed, and will be given in the next section with the ratio method.
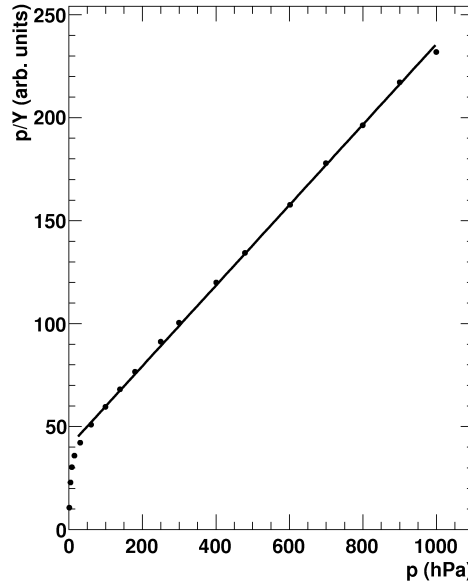
**Figure 4.3:** Stern-Volmer plot: $1/Y_{de-ex} = p/Y$ is plotted over pressure p. The line represents a linear fit in the range of 30-1000 hPa. At low pressures deviations from the linear behavior of the model are visible.

## 4.2.4   The Ratio Method

The correction for escaping secondary electrons due to the limited field of view of the photo-multiplier was introduced in Equation (4.4) and reads as

$$S_{FL} = C^* \cdot \frac{p}{1 + \frac{p}{p'}} \cdot F(p). \tag{4.10}$$

The correction factor $F(p)$ describes losses due to the geometry of the experiment. Since this effect stems from the geometry, it is the same for different gases (at the same energy) an approach to cancel its effect is to use only ratios of the relative yields $S_{FL}$ of two gases. As a result the data can be described with the ratio-method using

$$R = \frac{S_{FL}^{(1)}}{S_{FL}^{(2)}} = \frac{C^{*(1)}}{C^{*(2)}} \cdot \frac{1 + p/p'^{(2)}}{1 + p/p'^{(1)}} \cdot \frac{F(p)}{F(p)}. \tag{4.11}$$

Here, the correction $F(p)$ cancels, and therefore does not have to be determined by simulations. If gas 1 is nitrogen and gas 2 is "air", Equation (4.11) can be written as

$$R = \frac{S_{FL, N_2}}{S_{FL, Air}} = \frac{\rho_{N_2}}{\rho_{Air} \cdot 0.79} \cdot \frac{1 + p \cdot \left[ \frac{0.79}{p'_{N_2}} + \frac{0.21 \cdot \widehat{m}_{O_2}}{p'_{O_2}} \right]}{1 + p/p'_{N_2}}. \tag{4.12}$$

With $\rho$ being the respective gas densities, numerically

$$\frac{\rho_{N_2}}{\rho_{Air} \cdot 0.79} = 1.224. \tag{4.13}$$

The ratio of the factors $C^*$ is determined by the ratio of the respective densities, since everything else cancels. The factor 0.79 stems from the fluorescence efficiency of "air", because only nitrogen emits fluorescence light, so the efficiency is reduced by the relative amount of other gases. At last, the reference pressure for "air", $p'_{\text{Air}}$, had to be separated into a sum of its components. This reduces the correlation of the parameters for the fit, which is needed to obtain precise results. The sum reads as

$$\frac{1}{p'_{\text{Air}}} = \frac{0.79}{p'_{\text{N}_2}} + \frac{0.21 \cdot \widehat{m}_{\text{O}_2}}{p'_{\text{O}_2}}, \tag{4.14}$$

with $\widehat{m}_{\text{O}_2} = \sqrt{(m_{\text{N}_2} + m_{\text{O}_2})/2m_{\text{O}_2}} = 0.968$, see Section 2.3.2.

To determine the reference pressures, a $\chi^2$ minimization was performed with the fit function given in Equation (4.12). To estimate the statistical uncertainty, Gaussian error propagation was used to transfer the uncertainties of the slopes (signal and background) to the ratio. An uncertainty of the pressure measurement was assumed as 0.5 hPa. Additionally, the impact of different fit ranges on both, the scatter plots and the $R(p)$ plots have been studied and are assumed as systematic uncertainties.

Since there have been two background measurements — one before and one after each scan —, there are two different approaches to subtract the background. First an average was subtracted, hence, for each run the same background was subtracted. The other approach was to subtract the earlier background from the first half of runs and the later one from the second half. The difference of these two methods was found to be negligible.

The PMT gain was found to be stable within $\approx 1\%$ during all three runs. The effect of this change is also negligible.

### 4.2.5 Results and Discussion

**"Air" / "Air with Ar"**

With the ratio of the relative yields of "air" (here 79% $N_2$:21% $O_2$) and "air with argon" (here 78% $N_2$:21% $O_2$:1% Ar), it can be shown that there is no significant difference in the pressure dependence between these two gases. In the plot (Figure 4.4) all points are consistent with unity. This does not change with different fit ranges in the scatter plots. A fitted constant is consistent with one within its uncertainty. The fit yields $C = 1.005 \pm 0.01$. An effect due to argon can therefore be expected to be less than 1%.

Since "air" cannot be distinguished from "air with argon" by this analysis, it is not important which air measurement is compared to the nitrogen measurement. In this case measurement 2 is used, because they were taken in immediate succession, ensuring that nothing changed but the gas.

**Figure 4.4:** Numerical result of the Ratio method comparing measurements of "air" and "air with argon" as a function of pressure. The small graph shows the same plot for the original data. The large error of the data point at 15 hPa is due to an abnormal data point, caused by a voltage surge in the PMT signal. This data point was removed for the analysis, reducing the error of this data point as indicated, but not altering the result. The solid line shows the result of a fitted constant.

**Nitrogen / "Air with Ar"**

Figure 4.5 shows the ratio of nitrogen and "air with argon" plotted versus pressure. The nitrogen fluorescence yield is about 7 times higher than for air at 1 atm and the ratio decreases with pressure. It is also important to note that the relative uncertainty of the ratio increases with pressure, but the relative uncertainty of the pressure measurement decreases. This means that the uncertainty of the pressure measurement is important for the result of the fit, because without it the low pressure points would get too large relative weights and bias the fit.
The reduced $\chi^2/\mathrm{NDF}$ of the best fit is 1.0. This value of the reduced $\chi^2$ is a strong confirmation for the used fluorescence model. The numerical result is:

$$p'_{\mathrm{N}_2} = 102.79 \pm 5.7\,\mathrm{hPa} \qquad \mathrm{p}'_{\mathrm{O}_2} = 3.76 \pm 0.15\,\mathrm{hPa}. \tag{4.15}$$

The uncertainty resulting from the fit, cited as "statistical and $\Delta p$ error", and uncertainties of other sources as described in the last section (4.2.4) are stated in Table 4.3. The errors are assumed to be not correlated, and hence added quadratically to get a total uncertainty. With the determined values of $p'_{\mathrm{N}_2}$ and $p'_{\mathrm{O}_2}$ it is possible to calculate other parameters. The reference pressure of "air", Equation (4.14), and the collisional cross sections of nitrogen self-quenching
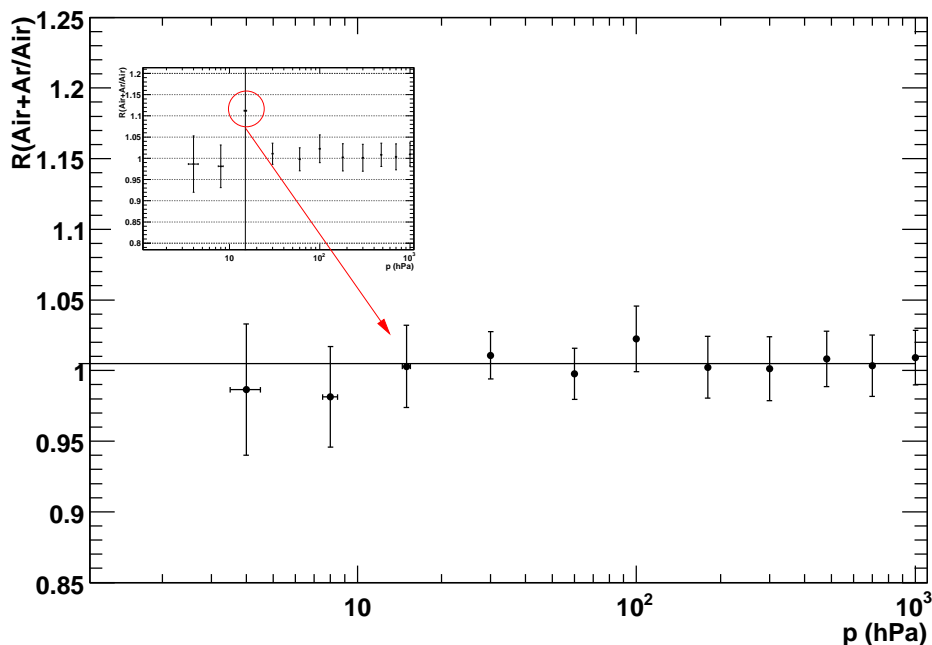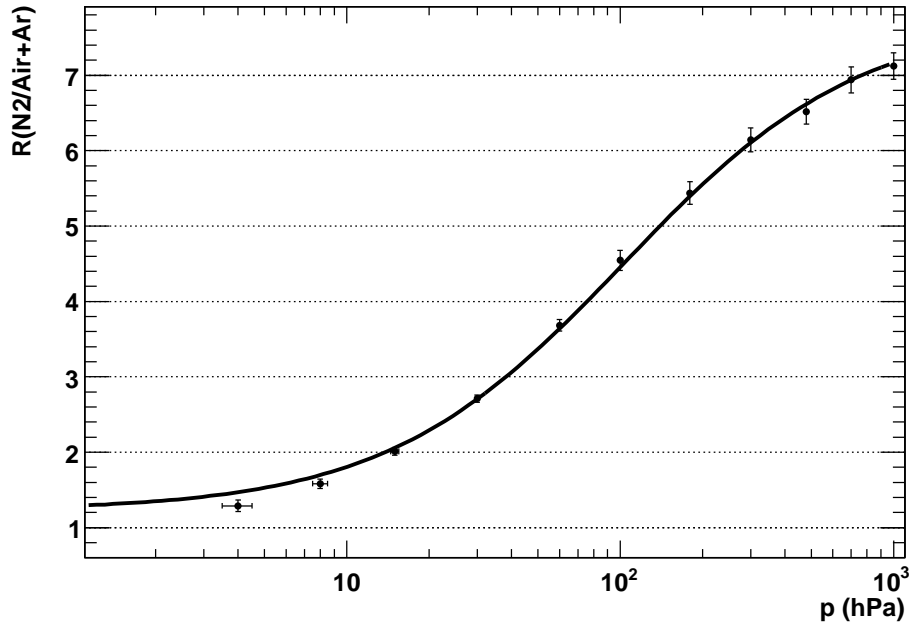
**Figure 4.5:** Numerical result of the Ratio method comparing measurements of nitrogen and "air with argon" as a function of pressure. The solid line is the best fit yielding $\chi^2/\mathrm{NDF} = 1.0$. At high pressure, the error of the ratio R is dominant, at low pressure the uncertainty of the pressure measurement is important.

$\sigma_{N_2}$ and nitrogen-oxygen quenching $\sigma_{O_2}$

$$\sigma_{N_2} = \frac{\sqrt{\pi m_{N_2} kT}}{4 \cdot p'_{N_2} \tau_0}, \tag{4.16}$$

$$\sigma_{O_2} = \left( \frac{\sqrt{\pi m_{N_2} kT}}{4 \cdot p'_{Air} \tau_0} - f_{N_2} \sigma_{N_2} \right) \frac{1}{f_{O_2} \sqrt{\frac{m_{N_2} + m_{O_2}}{2 m_{O_2}}}}. \tag{4.17}$$

With the lifetime of the upper state $\tau_0$, the molar mass of nitrogen and oxygen $M$, their contribution to the mixture $f$, the Boltzmann constant $k$, temperature $T$, and the respective reference pressures $p'$. The lifetime $\tau_0$ of the upper state $2P(\nu = 0)$ has recently been measured by three experiments [48, 55, 69]. They agree well within their uncertainties. Here, the value presented in [69] is used: $\tau_0 = 38.9 \pm 0.3$ ns. The other constants used are $m_{N_2} = 28$ u, $m_{O_2} = 32$ u, $k = 1.381 \cdot 10^{-23}$ J/K, $f_{N_2} = 0.79$, $f_{O_2} = 0.21$.

The results of the calculation, valid for room-temperature (20° C), are summarized in Table 4.4. The uncertainties were derived by Gaussian error propagation and are dominated by the uncertainties of $p'_{N_2}$ and $p'_{O_2}$.

It should be noted, that the results of the ratio analysis are not contradictory to the values obtained with the simple analysis without the correction $F(p)$. An analysis of measurement 3 and measurement 1, which were performed without argon in "air" the day before (see Table 4.1), yields the same reference pressures within the given uncertainties ($p'_{N_2} = 98.1$ hPa, $p'_{O_2} = 3.6$

| source | $\Delta p'_{N_2}$ (hPa) | $\Delta p'_{O_2}$ (hPa) |
|---|---|---|
| statistical and $\Delta p$ | 4.9 | 0.13 |
| scatter fit range | 2.3 | 0.06 |
| ratio fit range | 1.8 | 0.05 |
| background subtraction | negl. | negl. |
| PMT gain | negl. | negl. |
| TOTAL | 5.7 | 0.15 |

**Table 4.3:** Errors of the reference pressures of nitrogen and oxygen. They have been added quadratically to a total, that is dominated by the statistical uncertainty.

| Line | $p'_{N_2}$ (hPa) | $p'_{O_2}$ (hPa) | $p'_{Air}$ (hPa) | $\sigma_{N_2}$ $(10^{-20}\,\mathrm{m^2})$ | $\sigma_{O_2}$ $(10^{-20}\,\mathrm{m^2})$ |
|---|---|---|---|---|---|
| 337 nm | $102.8 \pm 5.7$ | $3.76 \pm 0.15$ | $16.2 \pm 0.6$ | $1.52 \pm 0.09$ | $41.5 \pm 0.3$ |

**Table 4.4:** Parameters of the pressure dependence of the fluorescence yield obtained by PMT measurements of the 337 nm line of the 2P(0,0)-transition.

hPa). A determination of the reference pressures using a simulated function $F(p)$ also yielded the same results within the stated uncertainty [59].

An attempt to determine the reference pressure of argon $p'_{Ar}$ was done by expanding Equation (4.14) to

$$\frac{1}{p'_{Air}} = \frac{0.79}{p'_{N_2}} + \frac{0.21 \cdot \widehat{m}_{O_2}}{p'_{O_2}} + \frac{0.01 \cdot \widehat{m}_{Ar}}{p'_{Ar}}, \qquad (4.18)$$

with $\widehat{m}_{Ar} = \sqrt{(m_{N_2} + m_{Ar})/2m_{Ar}} = 0.922$. This model yields no differences in $p'_{N_2}$ and $p'_{O_2}$. The obtained value for $p'_{Ar}$ was three orders of magnitude higher than the other parameters and had huge uncertainties. This, and the fact that the $\chi^2$ of the fit did not change, indicates, that the effect of argon is smaller than the accuracy of AIRFLY.

Thus, with the model obtained in Section 2.3.3 the pressure dependence of the fluorescence yield of the 2P(0,0) transition in air at 20° C is

$$Y(p) = \frac{C \cdot p}{1 + p/16.2\,\mathrm{hPa}}. \qquad (4.19)$$

**Comparison with other Experiments**

A comparison of the values of the reference pressures of nitrogen and air with other experiments is given in Table 4.5. Some parameters had to be converted into reference pressures or at least to SI units, because some authors give lifetimes and rate constants. Converted rate constants are marked with " $*$ ". All parameters refer to the common model of the fluorescence yield that was introduced in Section 2.3.3

| author | year | $p'_{N_2}$ (hPa) | $p'_{Air}$ (hPa) | Ref. |
|---|---|---|---|---|
| Present Result | | $102.8 \pm 5.7$ | $16.2 \pm 0.6$ | — |
| Waldenmaier | 2006 | $92.3 \pm 0.8^*$ | $15.5 \pm 0.3^*$ | [69] |
| Morozov et al. | 2005 | $80 \pm 7.3^*$ | — | [48] |
| Nagano et al. | 2004 | $155 \pm 4$ | $19.2 \pm 0.7$ | [50] |
| Nagano et al. | 2003 | $152 \pm 5$ | $19.2 \pm 0.7$ | [49] |
| Pancheshnyi et al. | 2000 | $74.3 \pm 12^*$ | $13.2 \pm 1.3^*$ | [55] |
| Brunet | 1973 | $113.5 \pm 22^*$ | $21.9 \pm 5^*$ | [14] |
| Mitchell | 1970 | $83.3 \pm 10$ | $13.1 \pm 1.3$ | [47] |
| Davidson and O'Neil | 1968 | $263 \pm 39$ | $14.4 \pm 2.2$ | [21] |
| Bunner | 1967 | $120$ | $20^{+3}_{-7}$ | [15] |
| Brocklehurst et al. | 1967 | $78.4 \pm 9$ | — | [12] |

**Table 4.5:** Reference pressures $p'$ of this analysis of AIRFLY data of the line at 337 nm and other experiments. Authors marked with "$*$" reported quenching rate constants, that have been converted into reference pressure using the radiative lifetime $\tau_0$.

The values of the reference pressures for nitrogen and air vary strongly, with a spread of about 200% and one extreme value of 263 hPa for $p'_{N_2}$ reported by Davidson and O'Neil [21]. The different results are not correlated with the date of the experiment, and no other correlation is obvious, although various exciting mechanisms, analysis procedures, and energy ranges were used. For example, two different observables have been utilized in the measurements, namely light intensity or lifetime of the excited state. The excitation mechanisms used are x-rays, low energy electrons, high energy electrons, electrons of the $\beta$-decay of $^{90}$Sr, or discharge tubes. Some authors invoke three body deactivation processes or believe in vibrational relaxation. All these differences in measurement, setup, and analysis are probably causing the deviations in the results, but the combination of possibilities do not allow a judgment of the quality of the individual experimental strategies.

In the more recent works, a tendency can be observed that experiments measuring lifetime report lower $p'$ values than those recording intensities (for instance [50] and [48]). To explain this discrepancy, the mechanism of vibrational relaxation was examined, but it is too weak to be even observed (see Section 2.3.1). However, older results of intensity studies also report low reference pressures (i.e. [47]), and AIRFLY obtains results near to an average of the former experiments (N$_2$: $\approx$109 hPa, without Davidson and O'Neil).

A comparison to the values of Nagano et al. as reported in [49, 50] for the 2P(0,0)-transition, is of great interest, because these are currently used by the Pierre Auger Observatory to interpret their fluorescence measurements of extensive air showers.

In the experiment of Nagano et al. the fluorescence light intensity is measured over a wide pressure range with photomultipliers, that observe a thin target. As in AIRFLY, the exciting particles are electrons, but the source is the $\beta$-decay of $^{90}$Sr with a maximum electron energy of 2.28 MeV. Interference filters were used to separate the band heads.

In [50], Nagano et al. state values for the reference pressures of $p'_{N_2} = 155 \pm 4$ hPa and

$p'_{Air} = 19.2 \pm 0.7$ hPa. The respective uncertainties are comparable to this work's accuracy. For pure nitrogen, the discrepancy of 50% is well beyond the stated uncertainties. Yet more important is the much smaller difference for air. It is about 15% and is within $2.3\sigma$ of the reported uncertainties.

However, the analysis of Nagano et al. does not utilize the fact that the reference pressure must be constant within a band system (see Section 2.3.3). There, the following reference pressures for other band heads of the 2P(0,*) band system are given (nitrogen): $p'_{2P(0,1)} = 125$ hPa, $p'_{2P(0,2)} = 128$ hPa and $p'_{2P(0,3)} = 140$ hPa. This indicates, that their value for $p'$ of the 2P(0,0) band head could be overestimated.

Another discrepancy in the results of Nagano et al. is, that the ratios of the fluorescence yields and reference pressures do not match for high pressures. For high pressures, Equation 4.12 can be simplified to

$$\frac{S_{FL,\,N_2}}{S_{FL,\,Air}} = \frac{\rho_{N_2}}{\rho_{Air} \cdot 0.79} \cdot \frac{p'_{N_2}}{p'_{Air}}. \tag{4.20}$$

For the results given in [50] at 1000 hPa, this equality is violated by 40%, indicating a possible bias in the measurements. The same ratios of the present work yield at 1000 hPa

$$7.2 \approx 7.8. \tag{4.21}$$

This is a very good agreement, since the ratio of the yields can be expected to increase by a small amount towards the limit of highest pressures, and hence, further reducing the relative difference of 8%. This suggests that the measurement and its analysis are consistent.

## 4.3   Energy Dependence of the Yield

A crucial assumption in the calculation of the primary energy of a cosmic-ray particle, detected with the fluorescence technique, is that the fluorescence yield is proportional to the energy deposit, given by the Bethe-Bloch equation (see Section 1.2.2). This is a reasonable assumption, since nitrogen is excited by collision with electrons and the Bethe-Bloch equation describes energy loss due to ionization, but up to now the proportionality of the fluorescence yield to the deposited energy is neither verified at all energies nor with sufficient precision.

Recent theoretical considerations lead to an expected deviation from the assumed proportionality. In Figure 4.6 results of Arqueros et al. [5] are shown as a plot of fluorescence yield over energy deposit as a function of electron energy. The lines correspond to different pressures from 1 hPa to 1013 hPa (dotted to solid line), and display a significant discrepancy to proportionality. To investigate the energy dependence of the fluorescence yield, AIRFLY has measured the relative yield at several energies. These measurements are addressed in the following.

### 4.3.1   Advanced VdG Data and its Processing

It was outlined in Section 4.2.1, that data taken at the VdG accelerator is difficult to analyze, and shows large systematic uncertainties, mostly due to invisible pedestal shifts that occur when
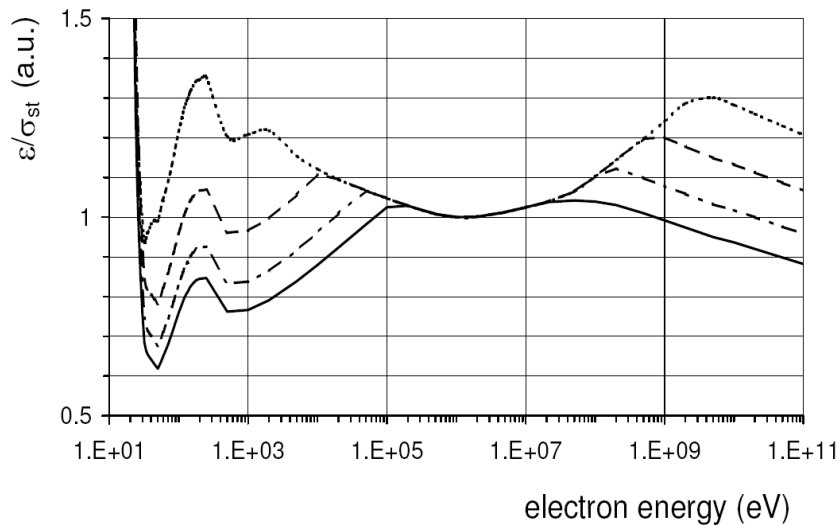
**Figure 4.6:** Theoretical considerations of Arqueros et al. lead to this plot of the ratio of fluorescence yield over stopping cross section (Bethe-Bloch) as a function of energy, normalized at 1 MeV. The curves correspond to different pressures of 1, 20, 200, and 1013 hPa (dotted to solid). The deviations from a horizontal line indicate deviations from proportionality. [5]

the beam changes. The measurements to determine the energy dependence of the fluorescence yield have been conducted at VdG, but in a more reliable manner.

At each energy, data was taken for four beam intensities: 0.2, 0.4, 0.6 and 0.8 $\mu$A. This leads to four independent measurements, effectively enlarging the fitrange in the $ADC_{PMT}$ over $ADC_{Pick-up}$ scatter plots (see also Section 4.2.1 and Figure 4.1(a)). Every measurement was accompanied with a background run, to monitor the beam, because a change in the beam leads to a shift in the pedestal of the Pick-up coil, which is visible in background measurements.

Additionally, the function of the Pick-up coil was checked at each energy by a comparison to the Faraday cup, for the respective signals are expected to be directly proportional, and the factor of proportionality constant. These Pick-up versus Faraday cup measurements have been done at each energy for all the mentioned beam intensities. They have also been carefully monitored with background runs.

Table 4.6 lists all energy measurements analyzed here, with their respective energy and date. The measurements were conducted without the chamber in laboratory air. During all three days, the relative humidity was stable at 80% and the temperature was stable at 20° C in the accelerator hall. The gain of the photomultiplier was monitored with a blue LED, and found stable within less than 1%.

Figure 4.7 shows the four scatter "clouds" of a typical measurement and their respective background measurements. The red points indicate the weighted centers of the clouds, and drawn in blue are the resulting data points with the linear fit that yields $S_{FL}$, the estimator for the fluorescence yield.

For the centers of the scatter clouds the uncertainty of the mean applies, and is calculated ac-

| ID | Date | $E_{beam}$ (MeV) |
|----|------|------------------|
| 1 | July $19^{th}$ 2006 | 3 |
| 2 | July $19^{th}$ 2006 | 2 |
| 3 | July $19^{th}$ 2006 | 1 |
| 4 | July $19^{th}$ 2006 | 3 |
| 5 | July $20^{th}$ 2006 | 3 |
| 6 | July $20^{th}$ 2006 | 0.8 |
| 7 | July $20^{th}$ 2006 | 0.5 |
| 8 | July $20^{th}$ 2006 | 1.5 |
| 9 | July $20^{th}$ 2006 | 2.5 |
| 10 | July $20^{th}$ 2006 | 0.9 |
| 11 | July $21^{st}$ 2006 | 3 |
| 12 | July $21^{st}$ 2006 | 1.5 |

**Table 4.6:** At VdG conducted energy runs with ID number, date and energy.

cording to

$$\sigma^2 = \frac{1}{n(n-1)} \sum_i (x_i - \mu)^2, \qquad (4.22)$$

with number of measurements $n$, measurement $x_i$ and mean value $\mu$.

This is calculated for signal and background for the PMT and Pick-up ADC-distribution separately, and gives uncertainties in x- and y-direction. The uncertainties are then propagated to the background reduced data points (blue in Figure 4.7). A $\chi^2$ minimization yields then the slope $S_{FL}$ and its uncertainty. Since all uncertainties are statistical, and hence not correlated, they are propagated using the simple Gaussian error propagation.

### 4.3.2   Results and Discussion

The obtained slopes are given in Table 4.7. At 3 MeV and 1.5 MeV more than one measurement has been conducted and the relative yields do agree very well. Below 1 MeV the Pick-up versus Faraday cup slope changes significantly. This suggests that below this energy the measurement is not reliable. In fact, the VdG is not designed for energies below 1 MeV, and it could be observed that the beam spot was very large and unstable, sometimes hitting the beampipe. This leads to a bad monitoring of the electron bunch size, and hence to bad data points. Therefore only results above 1 MeV are shown in Figure 4.8.

The errors stated with the data points include the statistical error. The gain of the photomultiplier was stable within $\approx 0.8\%$, and the temperature and humidity was constant in the accelerator hall. Other systematic uncertainties would apply to all measurements and therefore cancel in this relative plot. The dashed line indicates the collisional stopping power calculated for electrons in dry air with ESTAR [60]. It is proportional to the energy loss $dE/dX$ as described
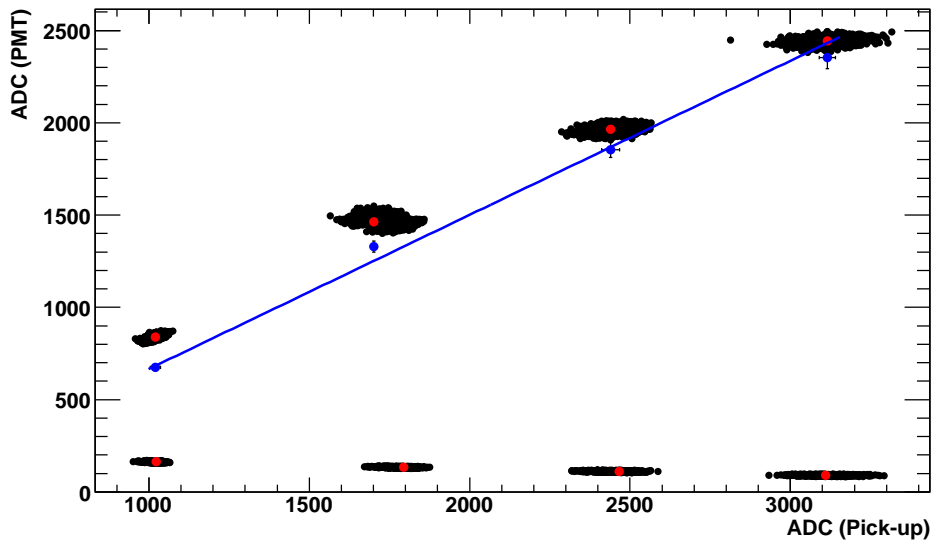
**Figure 4.7:** Plot of $\text{ADC}_{\text{PMT}}$ over $\text{ADC}_{\text{Pick-up}}$ at 3 MeV (scan1). All four beam intensities and background measurements of the advanced VdG measurements are shown. Red points indicate the weighted centers of the clouds, blue points show the background subtracted data points. The line represents a linear fit that yields $S_{FL}$.

by the Bethe-Bloch equation.

No significant deviations from proportionality can be recognized. This means, that in the range of 1-3 MeV the fluorescence yield is proportional to the deposited energy. This result agrees with the results of other authors [39, 69], who observed no deviations from $dE/dX$ within their accuracy.

| ID | E (MeV) | $S_{FL}$ | $S_{Fcup}$ |
|---|---|---|---|
| 1 | 3 | $1.20 \pm 0.04$ | $0.67 \pm 0.02$ |
| 2 | 2 | $1.16 \pm 0.05$ | $0.69 \pm 0.02$ |
| 3 | 1 | $1.05 \pm 0.05$ | $0.74 \pm 0.03$ |
| 4 | 3 | $1.20 \pm 0.04$ | $0.69 \pm 0.02$ |
| 5 | 3 | $1.19 \pm 0.03$ | $0.65 \pm 0.02$ |
| †6 | 0.8 | $1.57 \pm 0.07$ | $0.45 \pm 0.02$ |
| †7 | 0.5 | $1.85 \pm 0.12$ | $0.34 \pm 0.02$ |
| 8 | 1.5 | $1.17 \pm 0.04$ | $0.62 \pm 0.02$ |
| 9 | 2.5 | $1.10 \pm 0.03$ | $0.68 \pm 0.02$ |
| †10 | 0.9 | $1.24 \pm 0.04$ | $0.54 \pm 0.01$ |
| 11 | 3 | $1.24 \pm 0.04$ | $0.66 \pm 0.02$ |
| 12 | 1.5 | $1.18 \pm 0.03$ | $0.62 \pm 0.02$ |

**Table 4.7:** Relative yields $S_{FL}$ and factor of proportionality of the correlation between Faraday cup and Pick-up coil $S_{Fcup}$. Below 1 MeV (marked with "†") this correlation changes due to properties of the accelerator. Only data points above 1 MeV are considered reliable.



**Figure 4.8:** Graph of the stopping power of electrons in dry air ([60]). The data points correspond to the relative yield as a function of energy, and are normalized at 2 MeV. The uncertainties are statistical only, since systematic uncertainties cancel in this relative presentation. Multiple measurements at 1.5 MeV and 3 MeV agree within their respective uncertainties.
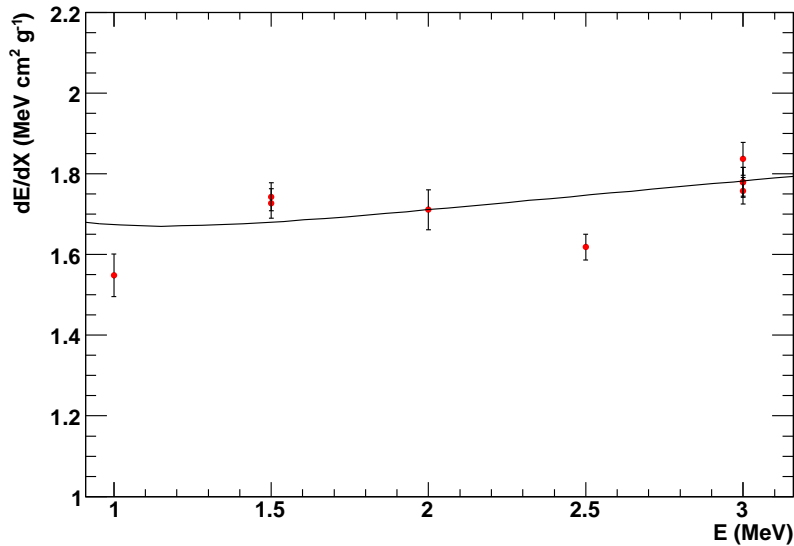
# CHAPTER 5

# THE FLUORESCENCE SPECTRUM

A spectral resolved measurement of the fluorescence spectrum of air with the quality, the AIR-FLY experiment provides, is new. Former experiments use filters or static monochromators to access single band heads. This is one of AIRFLY's biggest advantages.

The fluorescence spectrum between 280 nm and 430 nm contains band heads of the "second positive" band system of molecular nitrogen $N_2$ and the "first negative" band system of ionized nitrogen $N_2^+$ (Table 2.1). This chapter describes the spectral investigation of the fluorescence light, that is observed by cosmic-ray detectors.

The recorded spectra will be calibrated, then analyzed. There are two parts to each step: The calibration is performed for wavelength and for intensity. The analysis concentrates on the intensity ratios of the spectral lines and their dependence on pressure. Since all calculations are done relative to the 2P(0,0) band head at 337 nm, a relative calibration of the spectral intensity is sufficient.

The dynamic range of the spectrometer (see Section 3.1.3) is too small to record the whole spectrum at once. The measurement is split into two parts, between 280-370 nm and 340-430 nm. The calibration is done separately for each range, before the overlap (340-370 nm) is used to assemble the partial spectra. The merged spectra are then used for the analysis.

## 5.1   Calibration of the Spectra

The wavelength calibration is actually not needed for the calculations of the later analysis, but to determine the correct band heads. Each peak in the spectrum has to be identified in order to associate it with the correct vibrational transition. Therefore, the calibration does not need to be very accurate and its uncertainty does not affect the result of the later calculations.

The relative intensity calibration is important for the determination of intensity ratios of transitions. Since the calibration factor $C(\lambda)$ is not a constant, but depends on wavelength $\lambda$ it alters the ratios:

$$\frac{I_{real}(\lambda_1)}{I_{real}(\lambda_2)} = \frac{C(\lambda_1)}{C(\lambda_2)} \cdot \frac{I_{obs}(\lambda_1)}{I_{obs}(\lambda_2)},$$ (5.1)

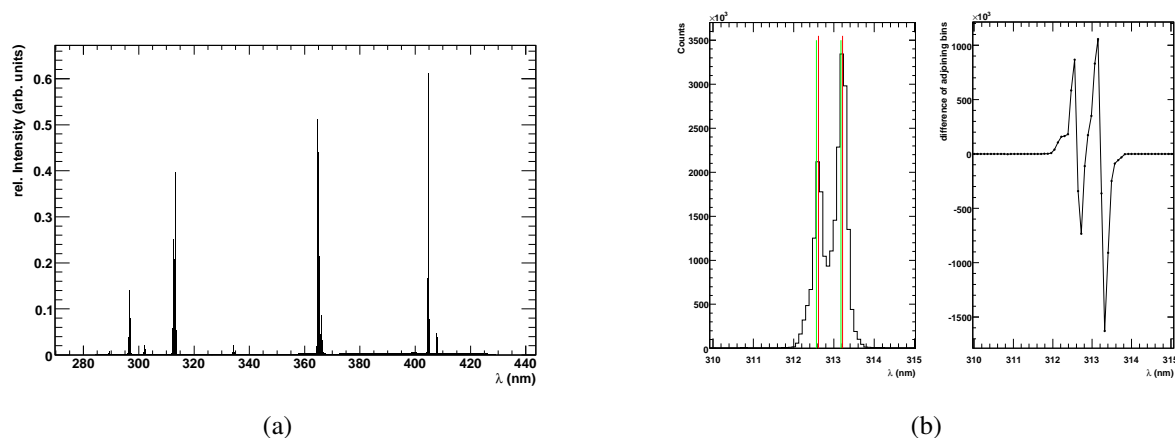(a)                                                                  (b)

**Figure 5.1:** (a) Spectrum of the mercury pencil lamp used for calibration. The actual positions of the spectral lines are well known and can be compared to measured ones. (b) Example of two spectral lines of the mercury pencil lamp spectrum (left) and the calculated difference of two adjoining bins (right). The zero transition from positive to negative values indicates the wavelength of a spectral line. Red lines in the spectrum mark the calculated peak position, green lines indicate reference values found in [63].

with observed and real intensities $I_{obs}$ and $I_{real}$ at wavelengths $\lambda_1$ and $\lambda_2$. Thus, the uncertainty of the calibration has to be taken into account.

Since the calibration $C(\lambda)$ does not depend on pressure, and the pressure dependence of the band heads is determined relative to the 2P(0,0)-transition, the intensity calibration has no effect on the calculation of the reference pressures $p'$ of the band heads. Therefore, the calibration's uncertainty can be neglected for this part of the analysis.

### 5.1.1   Wavelength Calibration

For the wavelength calibration, the measured wavelengths of spectral lines of a mercury pencil lamp were compared to reference values given in [63]. The spectrum of the lamp used is shown in Figure 5.1(a), and has a resolution of $\approx 0.1$ nm.

The position of the lines in the measured spectrum was found by calculating the zero-transition of its derivative. Therefore, the difference of two consecutive bins was plotted as a function of wavelength. The two points of this derivative, at which its sign changed from (+) to (-), were interpolated with a linear function, whose zero transition marks the position of the spectral line. Figure 5.1(b) illustrates this procedure with the graph of a recorded peak and its derivative.

One property of this method is, that the resulting wavelength is within the bin of maximum content, but it is weighted by the two surrounding bins. With the used bin width of 0.09 nm, this leads to an estimated uncertainty of the line positions of 0.05 nm. The uncertainty of the reference values is given as 0.0001 nm. The resulting wavelengths of the calibration measurement and the corresponding literature values are stated in Table 5.1. The relative difference between measured and expected wavelengths is very small. Nevertheless, this difference was interpolated with a polynomial of the order of three. Since both parts of the spectrum are recorded in

| $\lambda_{ref}$ (nm) [63] | $\lambda_{low}$ (nm) | $\lambda_{high}$ (nm) |
|---|---|---|
| 296.7283 | 296.737 | |
| 302.1504 | 302.173 | |
| 312.5674 | 312.616 | |
| 313.1727 | 313.213 | |
| 334.1480 | 334.279 | |
| 365.0158 | 364.774 | 365.107 |
| 365.4842 | 365.201 | 365.554 |
| 366.3196 | 366.054 | 366.429 |
| 404.6565 | | 404.794 |
| 407.7837 | | 407.903 |

**Table 5.1:** Reference wavelengths $\lambda_{ref}$ for calibration and the respective measured wavelengths for the first $\lambda_{low}$ and second $\lambda_{high}$ part of the spectrum.

the same way, a very similar interpolation function $f(\lambda)$ is expected for both parts. Its relation to the measurement is

$$\lambda_{real} = f(\lambda) \cdot \lambda_{meas}. \tag{5.2}$$

In fact, a fit yields almost the same function for both ranges:

$$f_{low}(\lambda) = 0.981573 + 0.337741 \cdot 10^{-3} \cdot \lambda - 1.56531 \cdot 10^{-6} \cdot \lambda^2 + 2.14666 \cdot 10^{-9} \cdot \lambda^3, \tag{5.3}$$

$$f_{high}(\lambda) = 0.990207 + 0.344281 \cdot 10^{-3} \cdot \lambda - 1.59081 \cdot 10^{-6} \cdot \lambda^2 + 1.97144 \cdot 10^{-9} \cdot \lambda^3. \tag{5.4}$$

After the calibration with the function $f(\lambda)$, the calculated wavelengths of the spectral lines of mercury agreed with the reference values within the estimated uncertainty of 0.05 nm. However, the calibration's uncertainty between the data points has to be assumed to be rather high, due to the great distance between them. This means, that deviations of the observed wavelength of the fluorescence band heads to values stated by other authors (for instance [56]) are to be expected. But the accuracy is high enough, that the band heads can be clearly identified, which is the pourpose of this calibration.

This calibration is valid for all used setups, because an offset or shift in wavelength can only be caused by internal properties of the spectrometer, and those have not been changed.

## 5.1.2 Intensity Calibration

An intensity calibration was accomplished by a comparison to a well known intensity distribution of a calibrated (NIST-traceable) light source. The light source is a halogen lamp with a continuous spectrum that is described as

$$I(\lambda) = e^{\left(A + \frac{B}{\lambda}\right)} \cdot \lambda^{-5} \left( C + \frac{D}{\lambda} + \frac{E}{\lambda^2} + \frac{F}{\lambda^3} + \frac{G}{\lambda^4} \right), \tag{5.5}$$
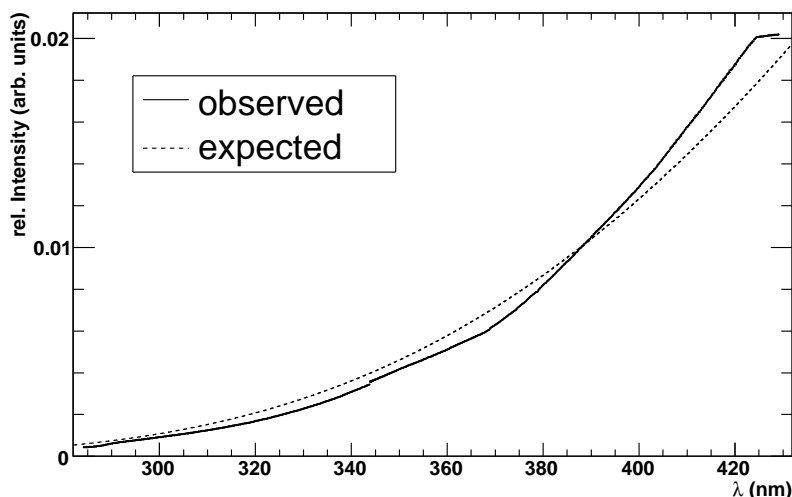
**Figure 5.2:** Measured spectrum of the halogen lamp used as a calibration light source (solid) and its ideal form calculated with Equation 5.5 (dashed). The areas under the spectra are scaled to unity, and in this plot the overlap region is averaged. This example shows the measurement for the setup of October 2005 without mirror.

with

$$
\begin{aligned}
A &= 42.7471566506923 \\
B &= -4673.39307023916 \\
C &= 0.901236780420845 \\
D &= 276.940799011223 \\
E &= -273055.609314449 \\
F &= 107653235.41275 \\
G &= -14011623123.4989.
\end{aligned}
\tag{5.6}
$$

The uncertainty of $I(\lambda)$ is 2.5%. The function given in Equation 5.5 givens the spectrum of the calibration lamp in units of irradiance, $\left[\mathrm{Jsm}^{-2}\right]$, which has to be considered for comparisons to other authors.

Since all spectra are analyzed relative to the 2P(0,0) band head at 337 nm, a relative calibration is sufficient. Therefore, an observed spectrum is compared to the expected "real" spectrum, given in Equation 5.5. This way, a calibration factor $C(\lambda)$ can be determined,

$$
I_{real}(\lambda) = C(\lambda) \cdot I_{obs}(\lambda).
\tag{5.7}
$$

The factor $C(\lambda)$ is the inverse of a relative sensitivity $s$, $C(\lambda) = 1/s(\lambda)$. A measured spectrum of the halogen lamp and the prediction of Equation 5.5 are shown in Figure 5.2.

Because it is a continuous spectrum, a calibration factor for each wavelength bin $C_i(\lambda)$ can be calculated, so there is no need for interpolation, and since a relative calibration is needed, only the slope of $C(\lambda)$ is important. On the other hand, it is necessary to conduct calibration measurements for every setup, because the alignment of the spectrometer or a mirror change
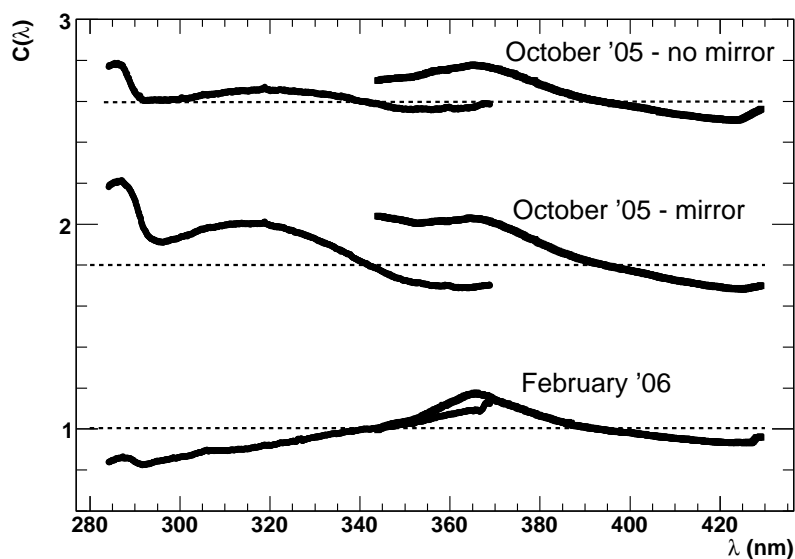
**Figure 5.3:** Calibration factors $C(\lambda)$ plotted over wavelength. The labels indicate the conditions of validity of the respective calibrations. The values for October '05 "mirror" and "no mirror" are shifted by 0.8 and 1.6 respectively to improve the view. For the relative calibration only the slopes of the curves are important.

the spectral sensitivity of the experiment. Therefore, Figure 5.3 shows three plots of $C(\lambda)$ over wavelength, each corresponding to a different setup (see labels).

Also, the sensitivity depends on the origin of the measured light. This is considered by changing the position of the light around the beam axis, thereby shifting the source's position in the spectrometer's field of view. The spectra are then weighted by their integral and added up to one "effective" spectrum, that is used to determine the calibration factor.

This analysis has been carried out for both parts of the spectrum independently. The uncertainty for the relative intensity calibration is composed of the uncertainty of the assumed lamp spectrum and the statistical error of the measurement. This adds up to 3%.

## 5.2 Analysis

This section describes the analysis of the measured fluorescence spectra after calibration. First, the dataset is given and the method used to merge the two parts is explained. After identifying all visible lines, the actual analysis is done in two steps. With spectra recorded at stable pressure with very good statistics, the intensity ratios of band heads are determined and the effect of argon is investigated. Then, with a series of spectra recorded at various pressures, the pressure dependence of the band heads is calculated.

| ID | date | kind | gas |
|----|------|------|-----|
| 1 | 18. October '05 | pressure scan | "Air with Ar" |
| 2 | 18. October '05 | pressure scan | "Air with Ar" |
| 3 | 18. October '05 | pressure scan | "Air" |
| 4 | 19. October '05 | pressure scan | "Air" |
| 5 | 20. October '05 | $p = 800\,\mathrm{hPa}$ | "Air" |
| 6 | 20. October '05 | $p = 800\,\mathrm{hPa}$ | "Air with Ar" |
| 7 | 20. October '05 | $p = 1000\,\mathrm{hPa}$ | Nitrogen |
| 8 | 11. February '06 | $p = 1000\,\mathrm{hPa}$ | Lab. Air |

**Table 5.2:** The dataset consists of eight independent measurements, that are stated with an ID number, date of measurement, what kind of measurement it was and which gas was used. "Air" corresponds to a mixture of nitrogen and oxygen (79%:21%), "Air with Ar" to a mixture of nitrogen, oxygen and argon (78%:21%:1%), and Lab. Air is natural air. Measurements were conducted at a Temperature of 293 K. Measurements of October 2005 were conducted at the Van de Graaff accelerator, the February measurement was done at the Advanced Photon Source (see Section 3.1.1).

### 5.2.1 The Dataset

There have been eight measurements that are considered in this analysis. For each measurement a proper calibration is available, even if they have been conducted at different days with a different setup. Table 5.2 shows the measurements, considered in the analysis. Measurements 1 to 4 are pressure scans ranging from 4 hPa to 1000 hPa, which are used to determine the reference pressure $p'$ for each band system. Measurements 5 to 8 are several spectra measured at the same pressure in close succession. These spectra can be added up to gain statistics and determine the intensity ratios of different lines precicely.

These spectra of stable conditions also show, that the measurements are very nicely reproducible, because the single spectra at the same pressure do not differ. This can be seen in Figure 5.4 that shows the distribution of the integrated intensity of the 2P(0,1) band head at 380 nm of the 10 individual spectra of measurement 5. The small spread shows the reliability of the measurements.

### 5.2.2 Preparation of the Spectra

In order to do the analysis some basic operations have to be done first.

Since the spectrum is measured in two parts, these have been corrected with the calibration, that was found earlier, separately. After the calibration of the wavelength the data points are no longer equidistant, so there was no way to chose a binning without empty bins. To avoid any bias due to binning, all data was processed without binning. Thus, no histograms have been used. Before the parts were merged to one complete spectrum, background that was found in
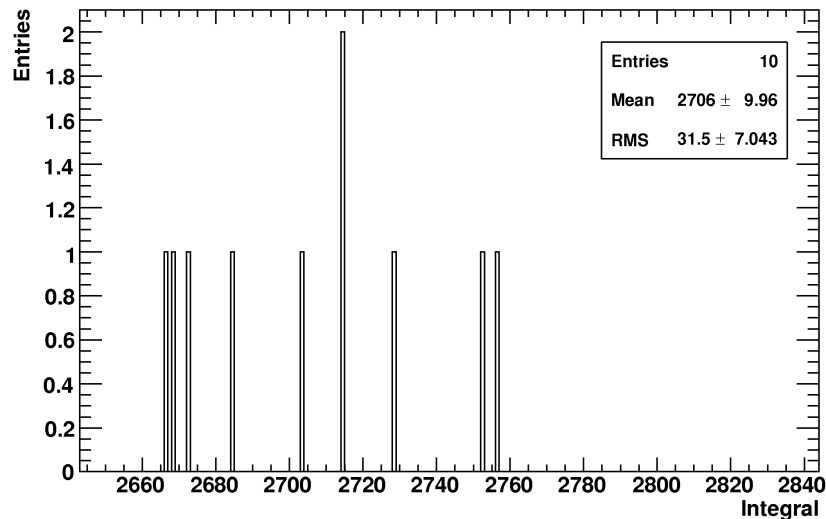
**Figure 5.4:** Integrated relative intensity of the 2P(0,1) band head (380 nm) of 10 spectra recorded under stable conditions at 800 hPa. The integration was performed within fixed borders and yields very stable results, indicating that the measurements are reproducible. The variance of the shown distribution is of statistical origin and leads to Poisson statistics for the calculation of the statistical uncertainty.

wavelength regions without lines was subtracted.

Without binning, integration was done by interpolating between each two points with a straight line and adding the areas contained within. Every integral mentioned hereafter has been derived this way, which is more accurate than integrating a histogram that, naturally, assumes a constant between points. However, the differences are only at the 0.1% level.

Prior to the actual analysis the two parts of the spectra have been merged into one complete spectrum. For some pressure scans there have been two measurements at the very same conditions. These measurements have been simply added up, before merging. In order to get a correct spectrum over the whole wavelength region, the intensity of the 2P(0,1) band head at 358 nm was compared, since it is included in both recorded parts of the spectrum. The upper part was weighted by the relative difference of the intensity of this common peak. These intensities have always been equal within 5%. Figure 5.5 shows the two parts of the spectrum, before they are merged into one.

 The error that is to be assigned to the integrals over some range of the spectrum has been found to be a Poisson-like error ($\sigma_N = \sqrt{N}$). To find this, integrals over different lines of the spectrum have been taken of all spectra of measurements 5, 6, 7, and 8. The spread of these integrals is in very good agreement to a Poisson error. In the following, the statistical uncertainty is always assumed to be a Poisson error.

The uncertainty of the wavelength calibration can be neglected, as well as the uncertainty of the intensity calibration in case of the pressure scans. Because the reference pressure is determined by relative intensities to the 2P(0,0) band head at 337 nm, the calibration's uncertainty does not affect the $p'$. However, the uncertainty of the intensity calibration has to be considered in the calculation of the intensity ratios of different lines.
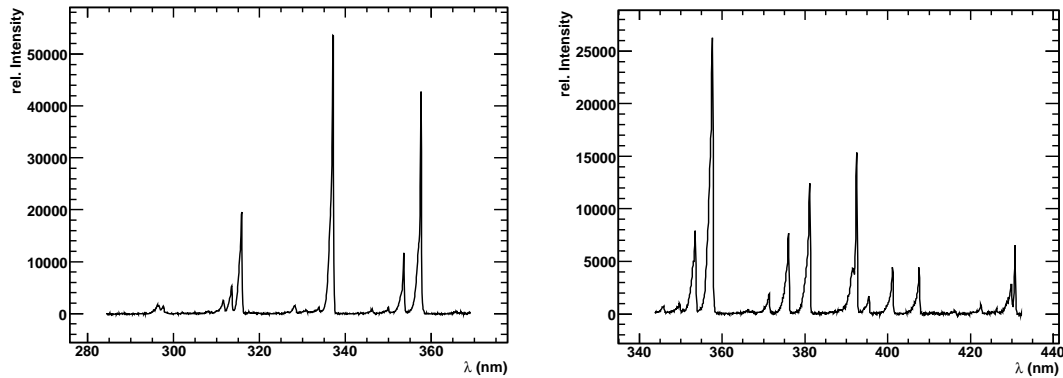
**Figure 5.5:** Parts of the Fluorescence spectrum, containing 10 measurements each. They have been simply added. The lower part reaches from 280nm to 369 nm, the upper part from 343 nm to 432 nm. The overlap region contains the 2P(3,4), 2P(2,3), 2P(1,2), and 2P(0,1) transitions.

For the identification of all visible band heads, all spectra of measurements 5, 6, 7, and 8 have been added up. All band heads can be accounted for as transitions of nitrogen. Of these lines 17 have been chosen to be analyzed for their pressure dependence. With the 2P(0,0) transition at 337 nm, relative to which all the other lines are considered, this includes 18 lines or 90% of all light emitted between 280 nm and 430 nm, and covers even more than 90% of the light collected by fluorescence detectors due to transmissions of the filters used.

The analyzed band heads are listed in Table 5.3, which is sorted by wavelength rather than transitions. The boundaries for the integration of the respective peaks are also given. Figure 5.6 shows the fluorescence spectrum measured with AIRFLY at 1000 hPa in laboratory air at APS.

**Figure 5.6:** Fluorescence spectrum of air recored at APS.

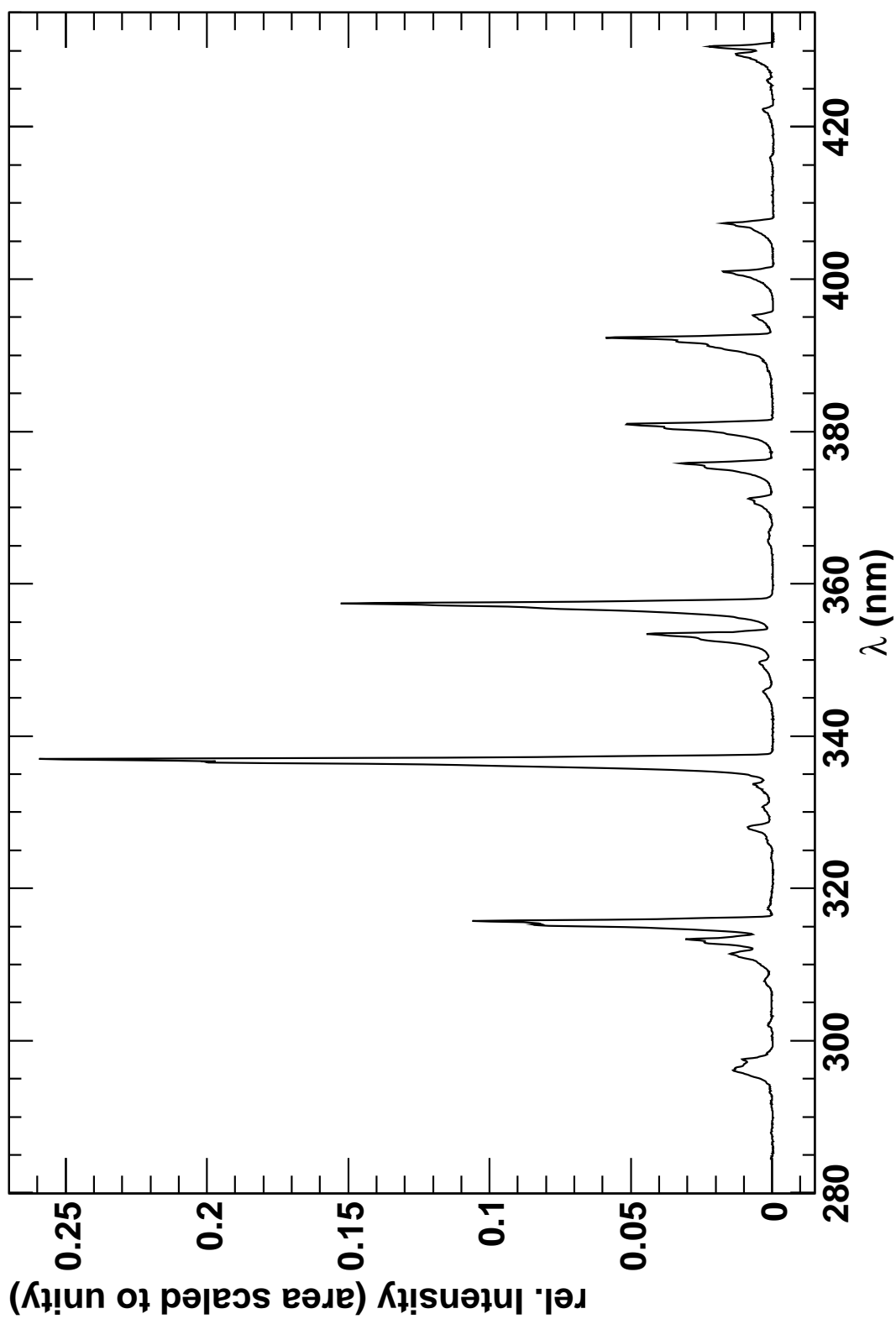| No. | Transition | $\lambda$ (nm) | lower Boundary (nm) | upper Boundary (nm) |
|-----|------------|-----------|-------------------|-------------------|
| 0 | 2P(0,0) | 337 | 334.5 | 338.5 |
| 1 | 2P(3,2) | 311.7 | 310.5 | 312.1 |
| 2 | 2P(2,1) | 313.6 | 312.1 | 314.0 |
| 3 | 2P(1,0) | 315.9 | 314.0 | 316.5 |
| 4 | 2P(3,3) | 328.5 | 327.0 | 329.0 |
| 5 | 2P(2,2) | 330.9 | 330.0 | 332.0 |
| 6 | 2P(1,1) | 333.9 | 332.5 | 334.3 |
| 7 | 2P(3,4) | 346.9 | 345.0 | 347.0 |
| 8 | 2P(2,3) | 350.1 | 348.0 | 350.5 |
| 9 | 2P(1,2) | 353.7 | 350.5 | 354.5 |
| 10 | 2P(0,1) | 357.7 | 354.5 | 359.0 |
| 11 | 2P(2,4) | 371.1 | 369.5 | 372.0 |
| 12 | 2P(1,3) | 375.5 | 373.0 | 377.0 |
| 13 | 2P(0,2) | 380.5 | 377.5 | 382.5 |
| 14 | 1N(0,0) | 391.8 | 390.0 | 393.2 |
| 15 | 2P(2,5) | 394.3 | 394.0 | 396.3 |
| 16 | 2P(1,4) | 399.8 | 399.0 | 402.0 |
| 17 | 2P(0,3) | 405.9 | 405.5 | 409.0 |

**Table 5.3:** Analyzed lines with the respective wavelengths, transitions and the boundaries used for their integration. This 18 band heads contain more than 90% of all light in the wavelength region of interest.

### 5.2.3   Intensity Ratios of the Spectral Lines

This section deals with measurements 5 to 8, whose spectra have been added and merged in order to compare them and calculate intensity ratios of the chosen lines. This way, the relative statistical error is very small, so that for the intensity ratios the dominant error stems from the calibration, which was assumed to be 3%.

**The Effect of Argon**

Figure 5.7 shows the spectra of "air" and "air with argon" at 800 hPa super-imposed on the same coordinate system. Their respective area is scaled to unity.
It is clearly visible that there is no difference at all. The spectra are distinguishable only in the very detail. This allows an important conclusion. Since the effect of Argon is twofold, it is a quenching partner to the nitrogen and it provides more secondary electrons, its effect could cancel for the 2P(0,0)-transition, which is mainly excited by secondaries. However, the initial state of the 1N(0,0)-transition is not as heavily excited by secondary electrons, hence the two effects would not cancel.
The fact that there is no difference in the spectra for both band heads leads to the conclusion
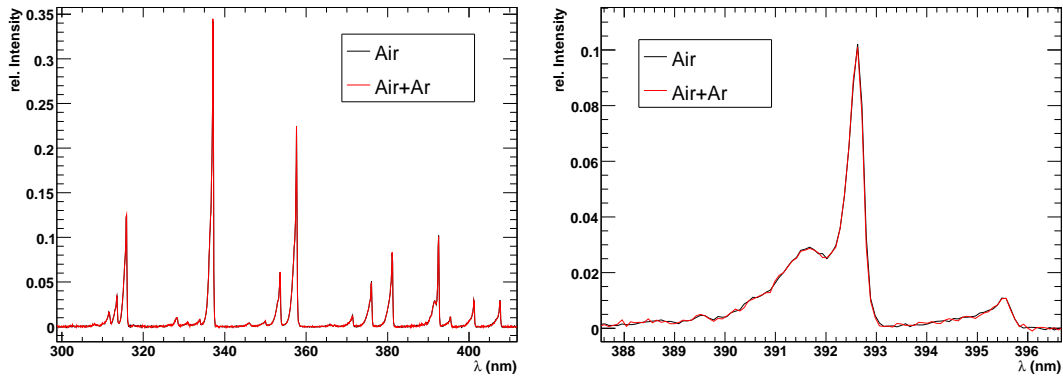
**Figure 5.7:** Comparison of "air" and "air with argon" spectra. The spectra are drawn in different colours in the same coordinate system, their respective areas are scaled to unity. On the left side, the 1N(0.0) band head at 391 nm is magnified.

that both effects are too small to be seen. This is a strong confirmation of the PMT result that "air" and "air with argon" do not show a difference within our accuracy.

**Intensity Ratios**

Measurements 7 and 8 can be used to find intensity ratios of the chosen lines at 1000 hPa. These numbers can be compared to theoretical values as well as to other authors who have measured the fluorescence yield of these lines separately. With these ratios and the reference pressure $p'$ for each line an artificial spectrum can be modeled and extrapolated to every desired pressure. The statistical error of the intensity ratios is due to the adding always lower than 1%, but the error due to calibration is 3%, which leads to the assumed error of 4.4% for each ratio of this analysis mentioned later. For the integration, fixed boundaries have been used. This was necessary, because no procedure could be found, that could have chosen these limits correctly. The correct fit of the limits to the peaks was checked by hand.

The ratios calculated here are ratios of irradiance $I$ of two different spectral lines. Since irradiance is proportional to energy $E$, these are ratios of the emitted energy per band head. To compare this to ratios of fluorescence yields $Y$ (proportional to the number of emitted photons, $\#\gamma$), or to transition probabilities $A$ (as given by Gilmore et al. [27]), it has to be converted using the wavelengths of the transitions:

$$I \propto E = \#\gamma \cdot \frac{hc}{\lambda}, \tag{5.8}$$

$$\frac{\#\gamma_1}{\#\gamma_2} = \frac{Y_1}{Y_2} = \frac{A_1}{A_2} = \frac{I_1}{I_2} \cdot \frac{\lambda_1}{\lambda_2}. \tag{5.9}$$

This is taken into account for all statements of ratios hereafter.

The ratios within a single band system are not influenced by the gas mixture. But the ratios to the 2P(0,0)-line differ from air to nitrogen, because band heads of different initial states are quenched differently by oxygen. In Table 5.4 all the calculated ratios can be found for air at 1000 hPa.

| (a) | | | | (b) | | |
|---|---|---|---|---|---|---|
| $\lambda$ (nm) | Transition | Ratio (%) | Gilmore [27] (%) | $\lambda$ (nm) | Transition | Ratio (%, air) |
| to 337nm (2P(0,0)) | | | | to 337 nm, 2P(0,0) | | |
| 358 | 2P(0,1) | $68.4 \pm 2.9$ | 67.5 | 312 | 2P(3,2) | $6.00 \pm 0.29$ |
| 380 | 2P(0,2) | $28.3 \pm 1.1$ | 27.2 | 314 | 2P(2,1) | $11.8 \pm 0.6$ |
| 406 | 2P(0,3) | $8.68 \pm 0.32$ | 8.4 | 316 | 2P(1,0) | $40.2 \pm 1.9$ |
| to 316nm (2P(1,0)) | | | | 328 | 2P(3,3) | $3.66 \pm 0.17$ |
| 334 | 2P(1,1) | $7.27 \pm 0.30$ | 4.9 | 331 | 2P(2,2) | $1.53 \pm 0.069$ |
| 353 | 2P(1,2) | $53.6 \pm 2.1$ | 46.6 | 334 | 2P(1,1) | $2.92 \pm 0.13$ |
| 375 | 2P(1,3) | $44.0 \pm 1.6$ | 41.4 | 347 | 2P(3,4) | $1.39 \pm 0.06$ |
| 399 | 2P(1,4) | $22.6 \pm 0.8$ | 20.4 | 350 | 2P(2,3) | $2.65 \pm 0.11$ |
| to 314nm (2P(2,1)) | | | | 353 | 2P(1,2) | $21.6 \pm 0.91$ |
| 331 | 2P(2,2) | $13.0 \pm 0.5$ | 7.9 | 358 | 2P(0,1) | $68.4 \pm 2.9$ |
| 350 | 2P(2,3) | $22.4 \pm 0.9$ | 16.9 | 371 | 2P(2,4) | $4.43 \pm 0.18$ |
| 371 | 2P(2,4) | $37.4 \pm 1.4$ | 40.0 | 375 | 2P(1,3) | $17.7 \pm 0.70$ |
| 394 | 2P(2,5) | $27.0 \pm 0.9$ | 31.1 | 380 | 2P(0,2) | $28.3 \pm 1.1$ |
| to 312nm (2P(3,2)) | | | | 391 | 1N(0,0) | $31.0 \pm 1.2$ |
| 328 | 2P(3,3) | $61.0 \pm 2.6$ | 48.0 | 394 | 2P(2,5) | $3.20 \pm 0.12$ |
| 347 | 2P(3,4) | $23.2 \pm 0.9$ | 1.9 | 399 | 2P(1,4) | $9.09 \pm 0.34$ |
| | | | | 406 | 2P(0,3) | $8.68 \pm 0.32$ |

**Table 5.4:** Intensity Ratios of different lines in % to the respective band heads (a) and to the 2P(0,0)-transition (b). Gilmore's values are theoretical. The ratios in Table (b) depend on the gas mixture.

The match with the theoretical values from [27] is good, although there are some small lines that are polluted by other lines and hence give biased numbers. Therefore this comparison to theory should not be stressed overmuch. The results given in Table 5.4(b) are also depicted in Figure 5.8.

Because the results of this thesis are only relative, a comparison to other experiments can also be relative only. However, if an absolute scale is adopted, absolute values can be given with the restriction, that they can only be used believing another author.

A relative comparison to Bunner [15] reveals that the results of the present analysis are in good agreement to Bunner's results. The overall deviation is a 10% higher yield for this thesis' results. The spectral distribution of the yield is very similar with a biggest deviation for the band heads at 316 nm and 358 nm. If Bunner's value for the fluorescence yield of 3.001 photons/m [41] is believed, this work's value turns out to be 3.36 photons/m.

A comparison to Nagano et al. [50] is of special interest, since these results are currently used by the Pierre Auger Observatory to calculate the primary energy of cosmic rays. In [50] the fluorescence yield of 10 mayor band heads are given, that sum up to a fluorescence yield of 3.698 photons/m. For these 10 band heads, the present result is 10% lower, indicating $Y = 3.29$ photons/m. However, believing the absolute scale of Nagano et al. all of the band heads analyzed in this thesis sum up to 3.7 photons/m.

This indicates, that the spectral distribution of the fluorescence light is not well resolved by
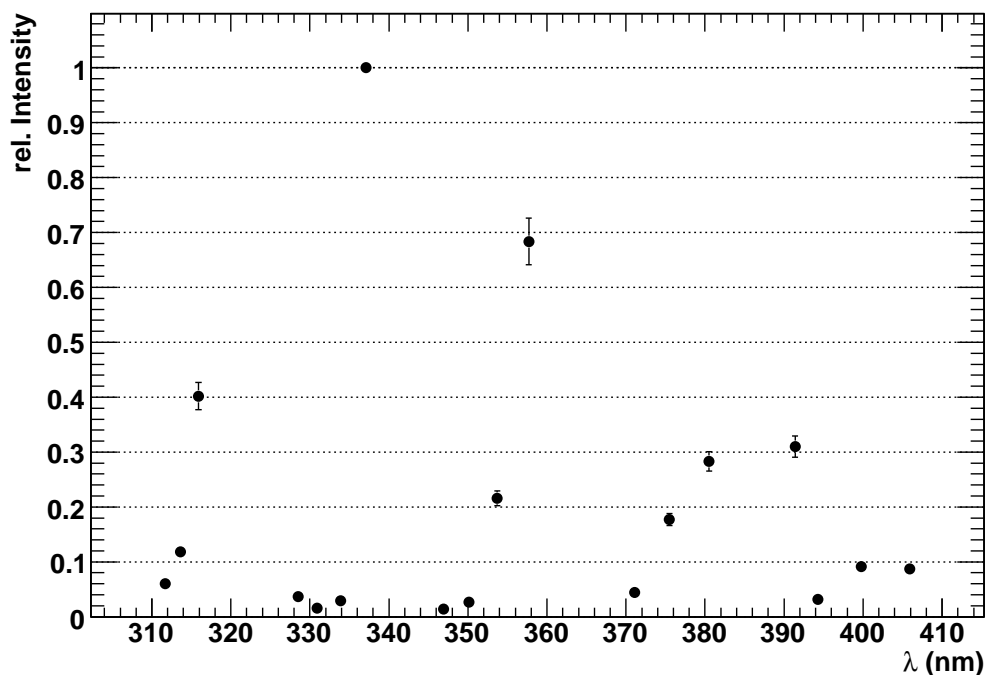
**Figure 5.8:** Model spectrum of AIRFLY results. The data points represent the relative intensities of the band heads analyzed. All points are relative to the 2P(0,0) band head, which is normalized to unity and whose uncertainty has therefore been propagated to the other band heads.

Nagano et al. They use interference filters and an analysis procedure to separate band heads within the same filter. Without this separation procedure, the stated results would be integral values of the respective filterbands, and in very good agreement with this diploma dissertation. The comparison to Bunner and Nagano et al. is summarized in Figure 5.9 (data from [41]). It shows an artificial relative spectrum. All line intensities have been normalized to the 2P(0,0)-line. Although the data points are relative, the absolute scales give a hint towards absolute yields. The data points of this thesis' analysis read to the absolute Bunner-scale give absolute values of the fluorescence yield as measured here, believing Bunner's value of $Y_{337}$. The same is true for the absolute Nagano-scale.
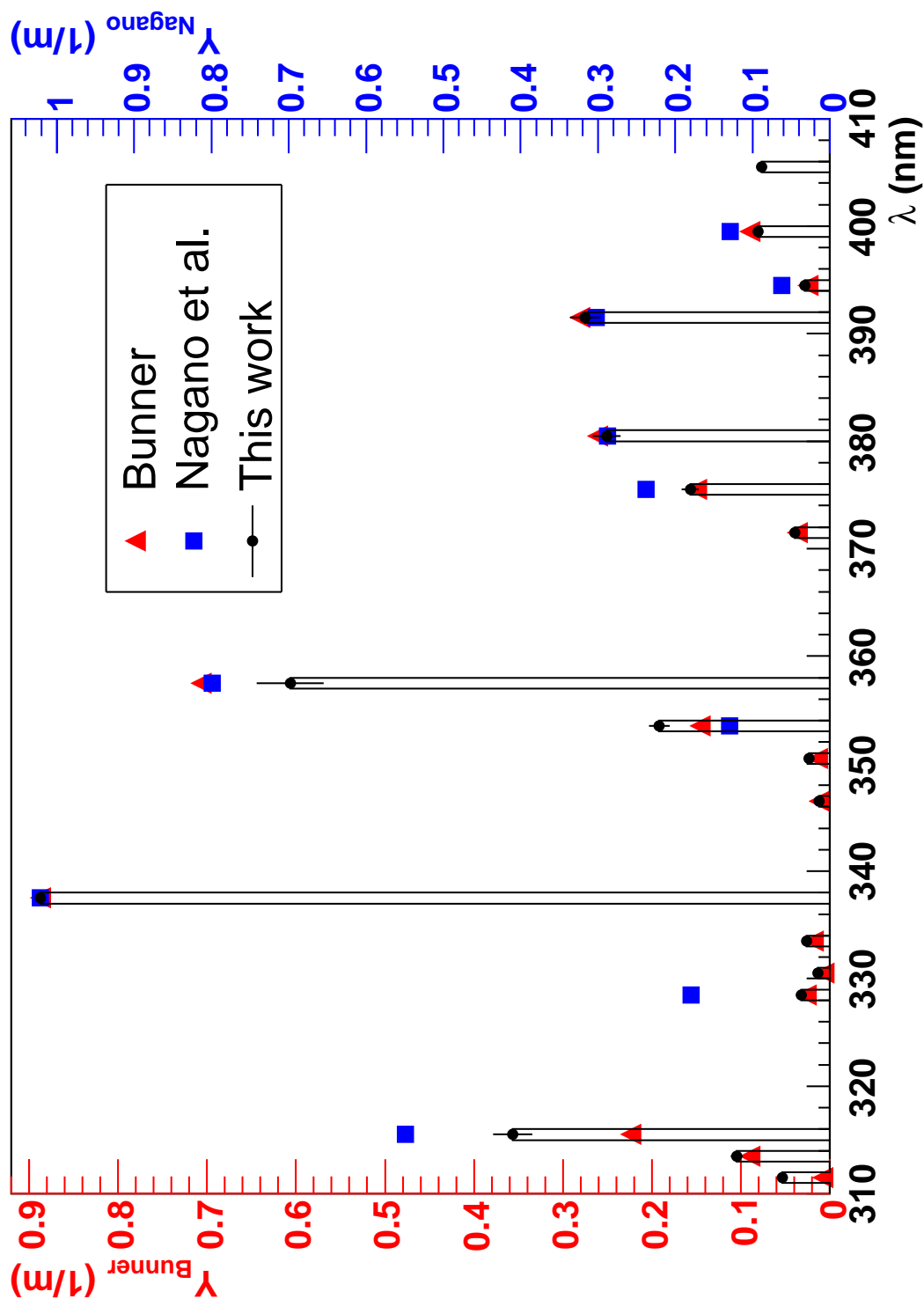
**Figure 5.9:** Comparison of the results of this thesis with Bunner [15] and Nagano et al. [50]. The data points are relative yields for each line, normalized to the 2P(0,0) band head. The absolute scales are those of Bunner and Nagano et al. respectively. Missing points indicate that the respective authors et al. do not give a value for the fluorescence yield of these band heads.
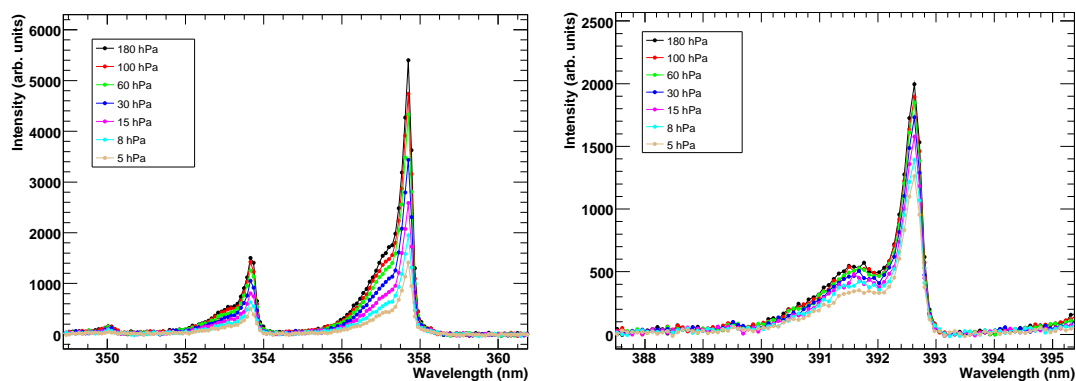
**Figure 5.10:** Relative intensities of the 2P(1,2), 2P(0,1), and 1N(0,0) band heads for different pressures, ranging from 180 hPa to 5 hPa, as indicated by different colours. Their shape does not change, but only their height.

## 5.2.4   Pressure Dependence of the Band Heads

Measurements 1 to 4 are pressure scans. In the following section their analysis will be outlined. The analysis of the presure dependence of the different lines is always relative to the 2P(0,0) transition whose reference pressure $p'$ equals $16.2 \pm 0.6\,\mathrm{hPa}$.

### Constant Form of Peaks

The position of the peaks is very stable, but in order to make as little errors as possible by integrating between fixed boundaries for each peak, it is important to know if their shape (i.e. width) changes. Therefore, Figure 5.10 shows some peaks at different pressures. The very high pressures have been excluded, because the intensity does not change visibly there, so the graphs of these peaks would lie on top of each other. The peaks of the 1N(0.0) band head are more closely cramped, because of the small reference pressure $p'$ of this line.

It is clear from these pictures, that the peaks keep their shape and width, but change only in height, indicating that the relative distribution of electrons on rotational states does not change.

### Pressure Dependence of the Band Heads

In order to determine the pressure dependence of every band head, measurements 1-4 have to be analyzed. First, every line is treated independently, to see if the obtained values are equal in a reasonable manner. This is an indication, whether the measurement and the analysis is biased. Then, a constraint is used that every band head of the same initial state has the same reference pressure $p'$. This reduces the uncertainty of the obtained parameters.

For each of the 17 chosen lines the intensity ratio to the 2P(0,0) line was calculated for each
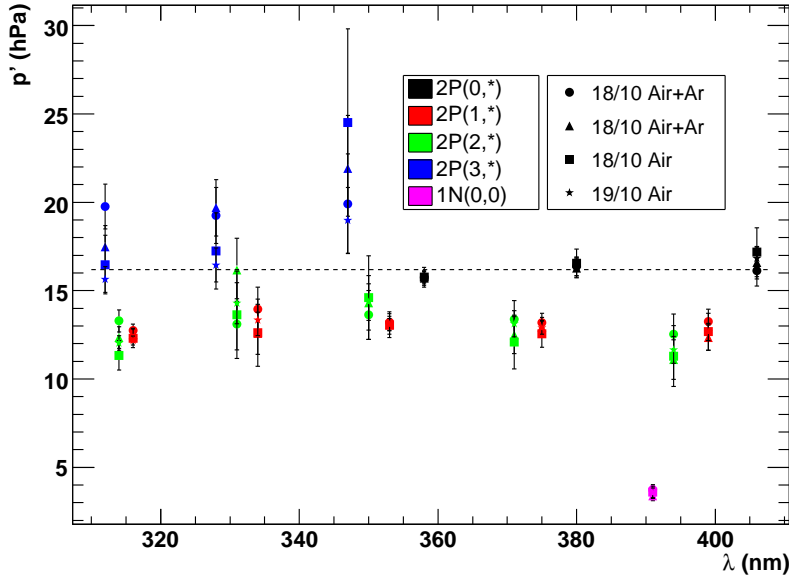
**Figure 5.11:** Results of pressure measurement analysis without constraint for each individual line. The reference pressures $p'$ are plotted over the wavelength of the respective band heads. Colours indicate band systems, different markers show different measurements. The dashed line is the PMT result relative to which the spectra have been analyzed.

pressure. Then the data points were fitted, using

$$\frac{I_{line}}{I_{337}} = R = \frac{\Phi^0_{line}}{\Phi^0_{337}} \cdot \frac{1 + \frac{p}{p'_{337}}}{1 + \frac{p}{p'_{line}}}, \tag{5.10}$$

with $p'_{337} = 16.2\,\text{hPa}$ and the ratio without quenching $\Phi^0_{line}/\Phi^0_{337}$.

The results of this method are given in Figure 5.11. It can be seen, that the reference pressures of the different lines of the same band system agree within their statistical errors. Also, the $p'$ values for the same band head and different scans agree within these errors, indicating, again, no difference between "air" and "air with argon". It also shows the stability and reproducibility of the measurements, as well as the correct functioning of the analysis procedure.

Furthermore, band heads that are polluted by other nearby lines do not show a significant shift in the reference pressure, which is due to the small differences in $p'$ for the different band systems. This indicates, that a further separation is not necessary. The determination of a common reference pressure for each band system is realized by a modified $\chi^2$ function that consists of several summands:

$$\chi^2 = \sum_{\text{lines}} \sum_i \left( \frac{(f_{\text{line}}(p_i) - R_i)^2}{\sigma_i^2} \right), \tag{5.11}$$

with the measured pressure $p_i$ and ratio $R_i$, their uncertainty $\sigma_i$, and a function

$$f_{\text{line}}(p_i) = \frac{\Phi^0_{\text{line}}}{\Phi^0_{337}} \cdot \frac{1 + \frac{p}{p'_{2\text{P}(0,*)}}}{1 + \frac{p}{p'_{\text{system}}}}, \tag{5.12}$$
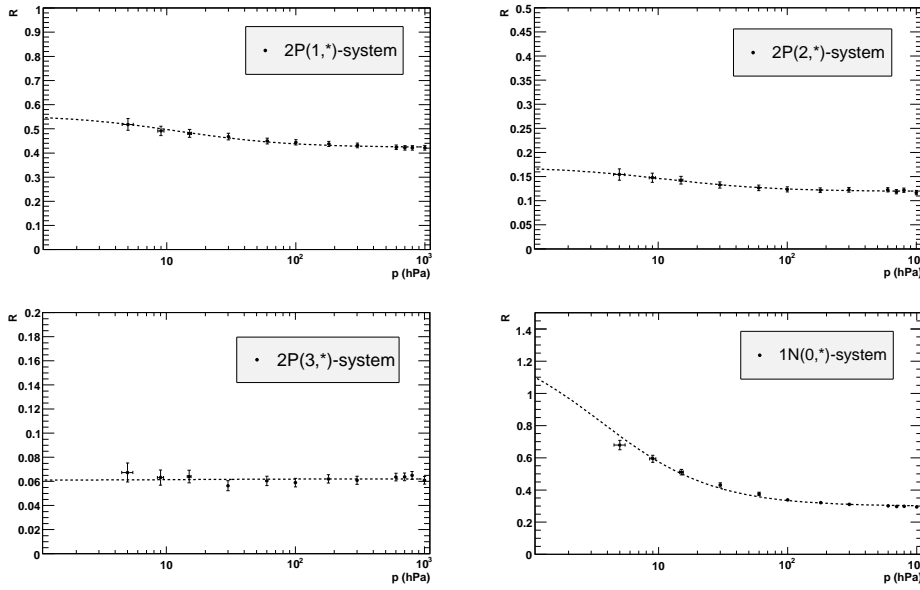
**Figure 5.12:** Intensity Ratios $R$ over pressure $p$ for the 2P(1,0), 2P(2,1), 2P(3,2), and the 1N(0,0) band heads. The more the data points differ from a constant line, the more the reference pressure differs from 16.2 hPa. The dashed lines indicate the respective fits yielding the reference pressures of the band systems. Please note the different scales for $R$.

| source | 2P(1,*) | 2P(2,*) | 2P(3,*) | 1N(0,0) |
|---|---|---|---|---|
| Poisson and $\Delta p$ | 0.23 | 0.44 | 0.94 | 0.29 |
| $\Delta p'_{337}$ | 0.51 | 0.52 | 0.70 | 0.30 |
| Integration Boundaries | negl. | 0.05 | 0.2 | negl. |

**Table 5.5:** Uncertainties for the determination of the reference pressure $p'$ for each band system. The statistical uncertainty is specific for measurement 1.

that includes a parameter $\Phi^0_{line}/\Phi^0_{337}$ for each line and a common parameter $p'_{system}$ for the whole band system.

The applied errors are the statistical Poisson-like error and $\Delta p = 0.5\,\text{hPa}$. By changing the value of $p'_{337}$ within its stated uncertainty, its error was propagated, as well as an uncertainty due to the integration boundaries was found by changing them systematically. The data points and the fit of the most intense band heads for each considered band system are given in Figure 5.12. The Poisson-like error assures, that weak lines have less weight in the fit, which is advantageous, because weak lines tend to be more polluted by other band heads. In Table 5.5 the mentioned uncertainties are stated for each system and for measurement 1. The statistical uncertainty does change from measurement to measurement (see Table 5.6), which is considered in the results, but the other uncertainties hold true for every measurement.

The common reference pressure $p'_{system}$ is in agreement to the single ones of the respective band system. The measurements agree with each other and the $p'$ value for the 2P(0,*) system is equal to the PMT result within its errors. In order to connect all four measurements, a weighted

| system \ scan | 1 | 2 | 3 | 4 | $\sigma_{sys}$ | RESULT |
|---|---|---|---|---|---|---|
| 1N(0,0) | $3.74 \pm 0.29$ | $3.40 \pm 0.28$ | $3.60 \pm 0.35$ | $3.56 \pm 0.28$ | 0.30 | $3.57 \pm 0.45$ |
| 2P(1,*) | $13.05 \pm 0.23$ | $12.74 \pm 0.24$ | $12.59 \pm 0.35$ | $12.64 \pm 0.16$ | 0.51 | $12.75 \pm 0.62$ |
| 2P(2,*) | $13.22 \pm 0.44$ | $12.75 \pm 0.45$ | $11.95 \pm 0.63$ | $12.58 \pm 0.30$ | 0.57 | $12.69 \pm 0.78$ |
| 2P(3,*) | $19.61 \pm 0.94$ | $18.80 \pm 0.92$ | $17.54 \pm 1.30$ | $16.29 \pm 0.55$ | 0.90 | $17.49 \pm 1.30$ |

**Table 5.6:** Reference Pressures in hPa of every system and scan. The stated errors are statistical. The result is the respective weighted average of the reference pressures of each band system. Its uncertainty is the sum of statistical and systematic uncertainty $\sigma_{sys}$.
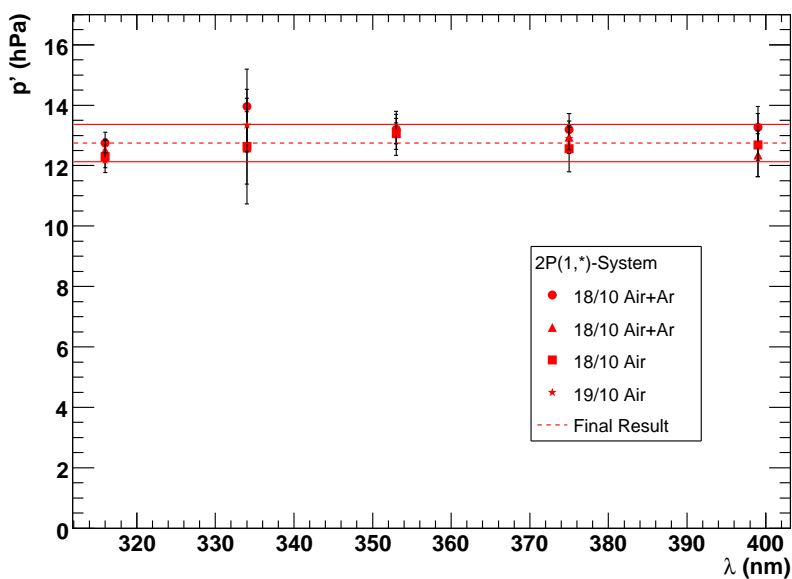


**Figure 5.13:** Reference pressure of the 2P(1,*) system plotted over the wavelength of the respective lines. The markers indicate different measurements, the lines depict the final result and its uncertainty.

average has been calculated for each band system [18]. Therefore, the statistical uncertainty has been propagated to the average value, and the systematic uncertainty that is the same for all measurements has been added to an uncertainty of the mean:

$$p' = \frac{\sum_{i=1}^{4} p'_i / \sigma_{i,stat}^2}{\sum_{i=1}^{4} 1/\sigma_{i,stat}^2} \pm \sqrt{\frac{1}{\sum_{i=1}^{4} 1/\sigma_{i,stat}^2}} \pm \sigma_{sys}. \tag{5.13}$$

With this method and the errors stated above, the result of the analysis of the spectrometer pressure scans can be given in Table 5.6. Figure 5.13 illustrates the result for the 2P(1,*)-system, and illustrates that the resulting error is in reasonable agreement with the individual results.

**Discussion of the Results**

Since a discussion of the results for the 2P(0,0) band head was already done in Section 4.2.5, it is not presented here, again. Table 5.7 states results of other authors and experiments. These

| author | 2P(1,*) | 2P(2,*) | 2P(3,*) | 1N(0,*) | reference |
|---|---|---|---|---|---|
| Present Result | $12.75 \pm 0.62$ | $12.69 \pm 0.78$ | $17.62 \pm 1.22$ | $3.57 \pm 0.45$ | — |
| Nagano et al. | 23-34 | $24.2 \pm 9.4$ | $40.2 \pm 4.6$ | $5.02 \pm 0.26$ | [50] |
| Mitchell | — | — | — | $1.23 \pm 0.13$ | [47] |
| Bunner | 8.7 | 6.1 | 3.3 | 1.4 | [15] |
| Hirsh et al. | — | — | — | $1.27 \pm 0.10$ | [34] |
| Waldenmaier | $15.4 \pm 0.3$ | — | — | $1.23 \pm 0.24$ | [69] |
| Pancheshniy et al. | $11.2 \pm 1.2$ | $9.10 \pm 1.3$ | $7.94 \pm 1.3$ | $2.4 \pm 0.29$ | [54, 55] |
| Davidson and O'Neil | $9.76 \pm 1.6$ | $11.4 \pm 1.8$ | $11.4 \pm 2.0$ | $1.22 \pm 0.4$ | [21] |

**Table 5.7:** Results for the pressure dependence of the band systems of the nitrogen fluorescence light emitted from air, given by various authors. All $p'$ values are given in hPa at temperature $\vartheta = 20°$ C.

values scatter over a wide range, with the largest deviations for the 2P(3.*)-system of a factor of 12. Because of its low intensity, this system is also the most difficult to analyze.

It should be mentioned here, again, that a reasonable judgment of the experimental strategies of the authors is not possible, and that these could account for the deviations of the results. The experiments cited in Table 5.7 differ in the source of the exciting electrons, or use x-rays or discharge tubes. The analyses of the different authors utilize different models of fluorescence, sometimes taking vibrational relaxation or three body processes into account. Some use interference filters, others monochromators.

Bunner, for instance, gives rather a compilation of the results obtained until 1967, mingling his own results with the results of Brocklehurst et al. and Davidson and O'Neil ([20] and references therein). Despite the experimental differences, the theoretical model for the fluorescence yield has always been the same as given in Section 2.3.3.

The advantage of this thesis' analysis is that the spectra actually show what is measured in a very direct way. It is not necessary to believe the filter transmission curve or the monochromator setting. Also, aspects of analysis procedures that have been used prior to this thesis have been examined and taken into consideration. The results obtained here relate to the previous ones as follows.

The best agreement to the present results is the measurement of Panshechniy et al. [54, 55] and of Davidson and O'Neil [21] who used a thick target. The results agree within their uncertainties, except for the 2P(3,*)-system. The obtained uncertainties are the lowest for light intensity measuring experiments.

Again, a dicussion of the results of Nagano et al. is of interest. The present results are not in agreement with those given in [50]. For the 2P(1,*)-system different reference pressures are given for the band heads, that vary from 23-34 hPa. The uncertainty is stated between 2 hPa and 4 hPa, depending on the band head. This means, reference pressures that have to be equal differ by $3\sigma$. This thesis' results for the reference pressures are allways lower, but tend to the same direction. For example the value for the reference pressure $p'_{2P(3,*)}$ is the highest, only in this analysis and in the work of Nagano et al.

# CHAPTER 6

# IMPACT ON EXTENSIVE AIR SHOWER MEASUREMENTS

This chapter investigates the consequences of the results, that have been obtained in this diploma dissertation. Therefore, Golden Hybrid events, events that can be reconstructed by an analysis of both surface and fluorescence detector observations, measured with the Pierre Auger Observatory have been analyzed twice and compared.

At present, the reconstruction procedure implemented for the Pierre Auger Observatory utilizes the results on the fluorescence yield by Nagano et al. [50]. Therefore, this thesis' results have been converted to parameters that are used in the "Nagano Fluorescence Model" by applying the respective absolute scale (see Figure 5.9). As a consequence, the following comparison is based on the assumption that the absolute fluorescence yield of the 2P(0,0) band head as reported in [50] is correct.

This comparison is a relative one between the "Nagano Fluorescence Model" and the present results with respect to the band head at 337 nm. It is believed that such a comparison is reasonable, because this band head is the most intense, hence most reliable and precise to determine. It is believed that future measurements will be in overall agreement on the absolute yield of the 2P(0,0)-transition.

The differences are expected to be small, because the overall agreement between this thesis and [50] is very good for air, even if there are some large deviations for individual band heads. Apparently, many differences cancel in average, if the total photon flux is considered.

For the comparison, one dataset of cosmic-ray events observed with the Pierre Auger Observatory was analyzed with exactly the same version of the analysis procedure, except for the fluorescence model.

**Dataset**  Golden Hybrid Events of the years 2004 and 2005, including 2718 extensive air showers.

**Analysis version**  $\overline{\text{Off}}\underline{\text{line}}$ v38 svn version r5065 ($9^{th}$ October 2006) with extensions of the Karlsruhe Group ($\overline{\text{Off}}\underline{\text{line}}$ KG cvstag v1r0p2_DrStrangelove)

| $\lambda$ | Nagano et al. | | Present Results | |
| | $A_\lambda$ | $B_\lambda$ | $A_\lambda$ | $B_\lambda$ |
| (nm) | (m$^2$/kg) | (m$^3$/kg/$\sqrt{K}$) | (m$^2$/kg) | (m$^3$/kg/$\sqrt{K}$) |
|---|---|---|---|---|
| 311.7 | — | — | 2.96 | 2.81 |
| 313.6 | — | — | 7.99 | 3.87 |
| 315.9 | 20.5 | 2.14 | 27.08 | 3.85 |
| 328.5 | 3.91 | 1.22 | 1.81 | 2.81 |
| 330.9 | — | — | 1.04 | 3.87 |
| 333.9 | — | — | 1.97 | 3.85 |
| 337.1 | 45.6 | 2.56 | 53.19 | 3.03 |
| 346.9 | — | — | 0.69 | 2.81 |
| 350.1 | — | — | 1.79 | 3.87 |
| 353.7 | 3.68 | 1.60 | 14.56 | 3.85 |
| 357.7 | 37.8 | 2.72 | 36.36 | 3.03 |
| 371.1 | — | — | 2.99 | 3.87 |
| 375.5 | 6.07 | 1.44 | 11.92 | 3.85 |
| 380.5 | 12.7 | 2.53 | 15.04 | 3.03 |
| 391.4 | 50.8 | 9.80 | 73.90 | 13.77 |
| 394.3 | 2.25 | 2.03 | 2.16 | 3.87 |
| 399.8 | 4.58 | 2.03 | 6.13 | 3.85 |
| 405.9 | 8.18 | 3.99 | 4.62 | 3.03 |
| 414 | 1.83 | 2.55 | — | — |
| 420 | 4.9 | 6.8 | — | — |
| 427 | 0.40 | 0.68 | — | — |
| 428 | 26.5 | 12.7 | — | — |

**Table 6.1:** Parameters of the fluorescence models used for comparison. Nagano et al. represents the standard model used at present in the Pierre Auger Observatory.

**Fluorescence Model** "Nagano Fluorescence Model":

Fluorescence yield at wavelength $\lambda$ by an electron of energy $E$ in units of [1/m] as a function of gas density $\rho$ ([kg/m$^3$]) and temperature $T$ ([K]):

$$Y_\lambda = \frac{\left(\frac{dE}{dx}\right)_E}{\left(\frac{dE}{dx}\right)_{0.85\text{MeV}}} \cdot \frac{A_\lambda \rho}{1 + \rho B_\lambda \sqrt{T}}, \tag{6.1}$$

with $A_\lambda = \left(\frac{dE}{dx}\right)_{0.85\text{MeV}} \cdot \Phi^0_\lambda \lambda/(hc)$ and $B_\lambda = R_{\text{air}} \cdot \sqrt{293}/p'_\lambda$. There, $dE/dx$ is the energy loss per pathlength, $\Phi^0_\lambda$ the pure fluorescence efficiency, $h$ the Planck constant, $c$ the speed of light, $R_{\text{air}}$ the gas constant of air, and $p'_\lambda$ is the reference pressure of the respective band system at 20° C. The parameters of the two models compared are given in Table 6.1.

A direct comparison of the two fluorescence models is illustrated in Figure 6.1 as a plot of the fluorescence yield calculated as a function of altitude above sea level. The calculation was
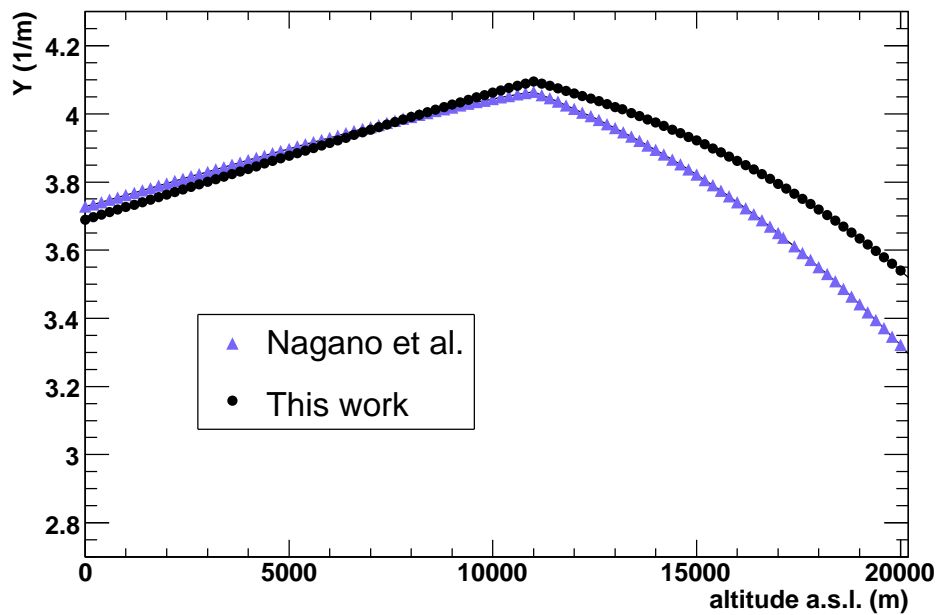
**Figure 6.1:** The fluorescence yield as a function of altitude above sea level, calculated for the Nagano fluorescence model and the altered model, according to this work's results. A US standard atmosphere is assumed and scattering neglected.

carried out for conditions of the US standard atmosphere [40, 52] including all wavelengths between 300 nm and 400 nm. The wavelength region was chosen to mimic the optical sensitivity of the telescopes of the Pierre Auger Observatory. Furthermore, for the comparison equal electron energies are assumed and scattering is neglected.

The difference between the models is greatest at high altitudes and vanishes at about 8 km height a.s.l. This comparison shows that the main difference is not in the absolute value of the yield, but in the pressure dependence.

The change of the spectral distribution of the light is not visible, because scattering was neglected in the calculation of the yield as a function of altitude, which means that the light is assumed to be observed at the point of production. At a given distance, the relative weight of the individual spectral lines is changed due to Rayleigh scattering, whose cross section is proportional to $1/\lambda^4$. Thus, the spectrum is shifted, weighting the lines at high wavelengths. There, slight differences in the spectrum can cause large differences in the reconstructed result.

An event-by-event comparison of air shower measurements revealed that the reconstructed energy of the cosmic-ray primary is shifted upwards by 3%. This shift is depicted in Figure 6.2 which shows a histogram of the relative difference in energy. The difference is calculated for each individual event that has been reconstructed twice. Once using the standard fluorescence model of Nagano et al., and then again using the modified model. The reconstructed events are within an absolute energy range of $10^{17}$ eV to $10^{20}$ eV.
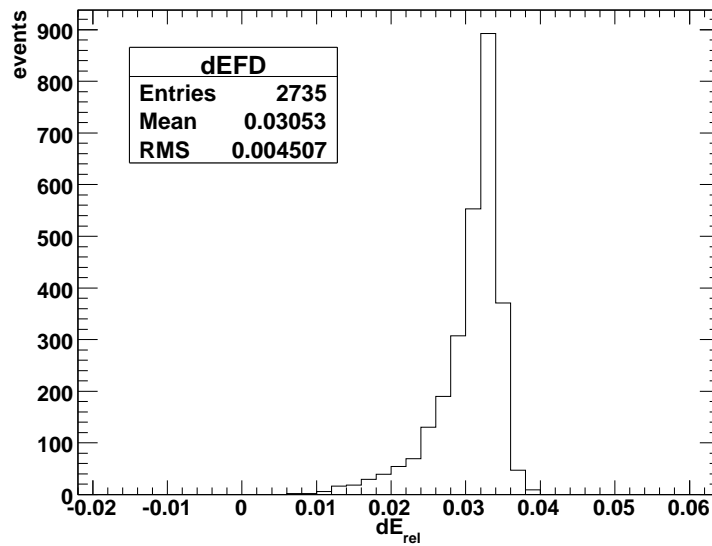
**Figure 6.2:** Relative difference in reconstructed primary energy obtained by an event-by-event comparison using the standard fluorescence model and the model altered according to this thesis' results. On average the new reconstructed primary energy is 3% higher. The absolute primary energy is between $10^{17}$ eV to $10^{20}$ eV.

The deviations are larger for higher energies, as indicated in Figure 6.3, which shows the relative difference in energy as a function of the standard energy. This can be explained, because air showers of higher energies are — in general — observed at different altitudes and different distance to the telescope, showing the effect of the deviations in pressure dependence of the fluorescence models and the effect of the altered spectral distribution of the light.

The correlation of $dE_{rel}$ with energy suggests, that if a new absolute measurement should reveal significant deviations in the fluorescence yield of the 2P(0,0) band head, its implications for extensive air shower measurements my not be significant at all energies.

A corelation of the effect of the present results with the amount of fluorescence light measured is visible in Figure 6.4. This plot shows the relative difference in reconstructed energy as a function of Cherenkov-fraction.

The Cherenkov fraction describes the relative amount of Cherenkov light that the fluorescence detector measured for an individual shower. This light is mainly emitted along the shower axis, which means that a shower, whose axis points into or near a telescope, is seen with a large Cherenkov fraction. The treatment of the Cherenkov light was not changed, explaining the decreasing difference in reconstructed energy at increasing Cherenkov fraction.

As expected, the impact of the modified fluorescence model vanishes, if the fraction of Cherenkov light increases. This can also explain the tail towards a Null-effect in the histogram of Figure 6.2, because these entries correspond to events with large Cherenkov-fraction.

The reconstruction of the zenith angel is not affected by the change of the fluorescence parameters. Hence, the determined geometry of each shower stays the same.
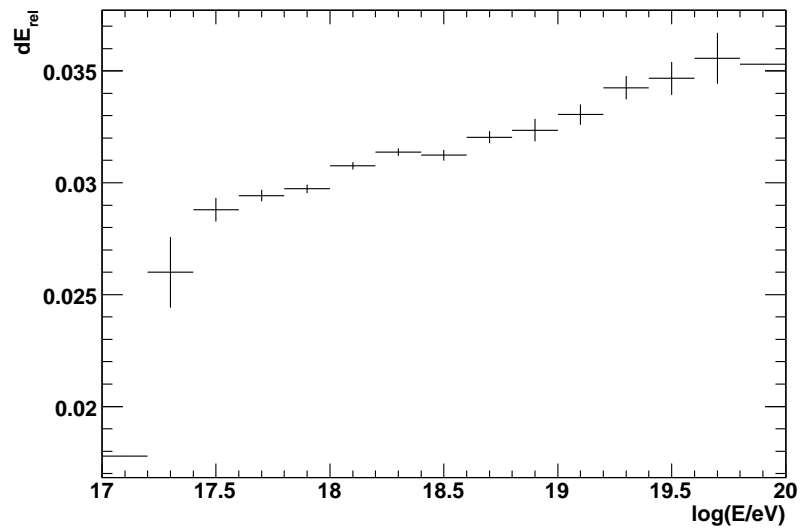
**Figure 6.3:** Relative difference in reconstructed energy as a function of energy. This is the result of an event-by-event comparison that indicates a change in reconstructed energy that increases with energy.
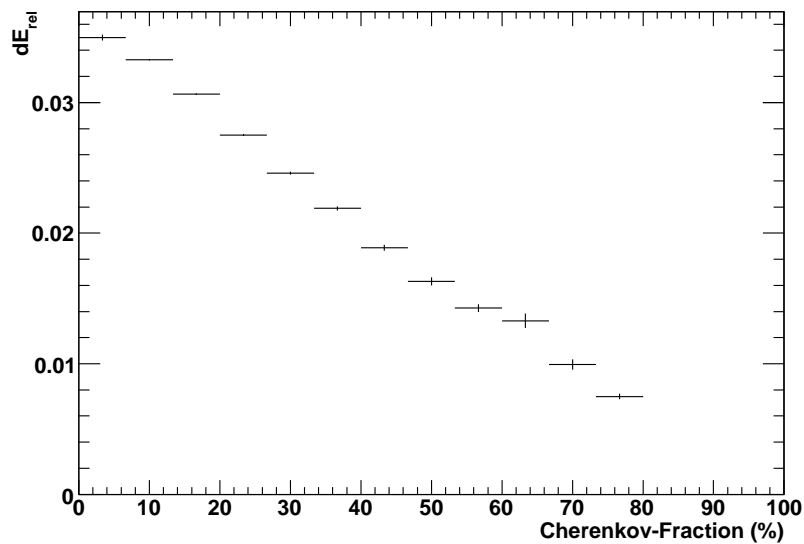


**Figure 6.4:** Relative difference in reconstructed energy as a function of Cherenkov fraction. A high Cherenkov fraction means less fluorescence light, whose treatment in the reconstruction has been altered. The effect of this change decreases, if less fluorescence light is observed.

# CHAPTER 7

# SUMMARY AND OUTLOOK

In this diploma thesis, the relative fluorescence yield has been studied. Its pressure dependence, and its energy dependence have been determined with measurements of the AIRFLY experiment.

The AIRFLY experiment is located at the Argonne National Laboratory, near Chicago (USA), and can use three different accelerators. It is a thin target experiment, that uses electrons between a few keV to 15 MeV to excite nitrogen or air at variable pressures, whose emitted fluorescence light is measured perpendicular to the beam by a photomultiplier or a spectrometer.

Advantages of AIRFLY are the use of relative measurements and the abandonment of simulations as far as possible, as well as the spectral resolved measurement at varying pressures, and a new strategy for an absolute end-to-end calibration. This diploma thesis has been restricted to relative measurements, but made use of the spectral resolved measurements, that are a new approach to the issue of the fluorescence yield.

The photomultiplier measurements provided a relative estimator for the fluorescence yield. This is the slope of the linear correlation of PMT signal and number of electrons, which was measured with a pick-up coil. These measurements have been conducted for varying pressures of different gases, and for varying energies, but for the 2P(0,0) band head only, that was filtered by an interference filter. *The measurements have shown that the fluorescence yield is, within the considered energy range, proportional to the energy deposit in the gaseous medium.*

The fluorescence yield as a function of pressure follows a Stern-Volmer kinetics. Its pressure dependence has been determined with the use of the reference pressure, which can be defined by a thermodynamic calculation as the pressure at which the radiative lifetime equals the lifetime of collisional deactivation. The reference pressure could be obtained directly from a Stern-Volmer plot, but a correction is needed, due to secondary electrons that escape the field of view of the PMT. *Thus, the ratio method has been introduced and the reference pressure of the 2P(0,0) band head has been determined to 16.2±0.6 hPa for air.*

The spectrometer measurements have been calibrated and analyzed. The intensity ratios obtained are in good agreement with theory and determine the spectral distribution of the fluorescence light, hence defining the fluorescence yield as a function of wavelength. *This way,*

*the spectral distribution of the fluorescence light emitted by air has been determined between 280 nm and 430 nm.*

In addition, the reference pressures of the four observable band systems — since the 2P(0,*) band system has been subject to the PMT measuremens and its reference pressure is a parameter here, it is not counted again — have been determined. Since the initial state of transitions specifies their affection by quenching, all band heads of the same band systems share one reference pressure. *They are:*

| System | 2P(0,*) | 1N(0,0) | 2P(1,*) | 2P(2,*) | 2P(3,*) |
|---|---|---|---|---|---|
| $p'$ (hPa) | $16.2 \pm 0.6$ | $3.57 \pm 0.45$ | $12.75 \pm 0.62$ | $12.69 \pm 0.78$ | $17.49 \pm 1.30$ |

*Another important result is that argon has no significant effect on the fluorescence yield in the atmosphere.*

A comparison to the results of Bunner and Nagano et al. reveals significant differences for some details, but shows a good overall agreement, because deviations in individual band heads average. In order to investigate these small deviations, an event-to-event comparison of the primary energy of cosmic-ray particles, that the currently used fluorescence model yielded after the reconstruction of extensive air showers observed by the Pierre Auger Observatory, to energy reconstructed with the use of the results obtained here was performed with 2718 events. *It revealed an energy shift towards higher energies of 3%.*

Although this thesis is completed, the measurement schedule of AIRFLY is still rich. The absolute calibration with Cherenkov light is on its way, and will allow for a precise determination of the absolute fluorescence yield.

Furthermore, the effects of water vapor on the yield will be studied, and its temperature dependence determined.

Some further measurements have already been conducted at the Argonne National Laboratory and need to be analyzed, other measurements have yet to be done. Some of them will be undertaken at the Beam Test Facility, in Frascati (Italy).

# BIBLIOGRAPHY

[1] J. Abraham et al. for the Pierre Auger Collaboration. Properties and performance of the prototype instrument for the Pierre Auger Observatory. *Nucl. Instr. and Meth. A*, 523:50, 2004.

[2] C. D. Anderson. The positive electron. *Phys. Rev.*, 43:491, 1933.

[3] F. Arciprete et al. AIRFLY: Air fluorescence induced by electrons in a wide energy range. In *Proc. 28th Int. Cos. Ray Conf.*, page 837, Tsukuba, Japan, 2003.

[4] F. Arciprete et al. AIRFLY: Measurement of the fluorescence yield in atmospheric gases. In *Proc. 29th Int. Cos. Ray Conf.*, volume 7, page 55, Pune, India, 2005.

[5] F. Arqueros, F. Blanco, A. Castellanos, M. Ortiz, and J. Rosado. The yield of air fluorescence induced by electrons. *Astroparticle Physics*, 26(4):231, 2006.

[6] P. Auger. Extensive cosmic-ray showers. *Rev. Mod. Phys.*, 11:288, 1939.

[7] J. A. Bellido for the Pierre Auger Collaboration. Performance of the fluorescence detectors of the Pierre Auger Observatory. In *Proc. 29th Int. Cos. Ray Conf.*, volume 7, page 13, Pune, India, 2005.

[8] W. A. Bingel. *Theorie der Molekülspektren*. Chemische Taschenbücher 2. Verlag Chemie, Weinheim, 1967.

[9] F. Blanco and F. Arqueros. The role of secondary electrons in some experiments determining luorescence emission from nitrogen $C^3\Pi_u$ levels. *Phys. Lett. A*, 345:355, 2005.

[10] J. Blümer for the Auger Collaboration. Cosmic rays at the highest energies and the Pierre Auger Observatory. *J. Phys. G: Part. Phys.*, 29:867, 2003.

[11] H. L. Bradt and B. Peters. Investigation of the primary cosmic radiation with nuclear photographic emulsions. *Phys. Rev.*, 1948:1828, 1948.

[12] B. Brocklehurst and F. A. Downing. Mechanism of excitation of luminescence in nitrogen gas by fast electrons. *J. Chem. Phys.*, 46(8):2976, 1967.

[13] R. Brun and F. Rademakers. ROOT: An object oriented data analysis framework. *Nucl. Instr. and Meth. A*, 389:81, 1997.

[14] H. Brunet. *Destruction des Etats $C^3\Pi_u$ ($v' = 0$ et $v' = 1$) de $N_2$ dans l'Azote pur et melange avec* $O_2, H_2O, CO_2, CH_4$. PhD thesis, Paul-Sabatier University, France, 1973.

[15] N. A. Bunner. *Cosmic ray detection by atmospheric fluorescence*. PhD thesis, Cornell University, New York, 1967.

[16] J. M. Calo and R. C. Axtmann. Vibrational relaxation and electronic quenching of the $C^3\Pi_u$ ($\nu' = 1$) state of nitrogen. *J. Chem. Phys.*, 54(3):1332, 1971.

[17] P. Colin. *Reconstruction des gerbes atmospheriques et mesure de la fluorescence de l'air pour l'etude des rayons cosmiques ultra energetiques au sein du projet EUSO*. PhD thesis, University Grenoble, France, 2005.

[18] G. Cowan. *Statistical Data Analysis*. Clarendon Press, Oxford, 1998.

[19] J. W. Cronin. Cosmic rays: the most energetic particles in the universe. *Rev. Mod. Phys.*, 71(2):165, 1999.

[20] G. Davidson and R. O'Neil. Optical radiation from nitrogen and air at high pressure excited by energetic electrons. *J. Chem. Phys.*, 41(12):3946, 1964.

[21] G. Davidson and R. O'Neil. The fluorescence of air and nitrogen excited by energetic electrons. Final Report for the Air Force Cambridge Research Laboratories, 1968. AFCRL-67-0227.

[22] R. Engel. private communication, 2006.

[23] R. Engel. Very high energy cosmic rays and their interactions. *Nucl. Phys. B (Proc. Suppl.)*, 151:437, 2006.

[24] E. Fermi. On the origin of cosmic radiation. *Phys. Rev.*, 75(8):1169, 1949.

[25] J. T. Fons, J. S. Allan, R. S. Schappe, and C. C. Lin. Production of electronically excited $N_2^+$ ions by electron impact an $N_2$ molecules. *Phys. Rev. A*, 49(2):927, 1994.

[26] J. T. Fons, R. S. Schappe, and C. C. Lin. Electron-impact excitation of the second positive band system ($C^3\Pi_u \longrightarrow B^3\Pi_g$) and the $C^3\Pi_u$ state of the nitrogen molecule. *Phys. Rev A*, 53(4):2239, 1996.

[27] F. R. Gilmore, R. R. Laher, and P. J. Espy. Franck-condon factors, r-centroids, electronic transition moments, and einstein coefficients for many nitrogen and oxygen band systems. *J. Phys. Chem. Rev. Data*, 21(5):1005, 1992.

[28] K. Greisen. End to the cosmic-ray spectrum? *Phys. Rev. Lett.*, 16(17):748, 1966.

[29] A. E. Grün and E. Schopper. Die Untersuchung von Energieaustausch- und Lösch-prozessen in Gasen durch Anregung mit schnellen Teilchen. *Z. Naturforschg.*, 9a:134, 1954.

[30] H. Haken and H. Ch. Wolf. *Molekülphysik und Quantenchemie*. Springer Verlag, Berlin, 2005.

[31] V. F. Hess. Über Beobachtungen der durchdringenden Strahlung bei sieben Freiballon-fahrten. *Physik. Zeitschr.*, 13:1084, 1912.

[32] V. F. Hess. Über den Ursprung der durchdringenden Strahlung. *Physik. Zeitschr.*, 14:610, 1913.

[33] A. M. Hillas. The origin of ultra-high energy cosmic rays. *Annu. Rev. Astron. Astrophys.*, 22:425, 1984.

[34] M. N. Hirsh, E. Poss, and P. N. Eisner. Absolute fluorescence yields of 3914-Å photons from $N_2$ and air excited by relativistic electrons. *Phys. Rev. A*, 1(6):1615, 1970.

[35] J. Hörandel. On the knee in the energy spectrum of cosmic rays. *Astropart. Phys.*, 19:193, 2003.

[36] J. Hörandel. Overview on direct and indirect measurements of cosmic rays. *J. Mod. Phys. A*, 20(29):6753, 2005.

[37] Y. Itikawa et al. Cross sections for collisions of electrons and photons with nitrogen molecules. *J. Phys. Chem. Ref. Data*, 15:985, 1986.

[38] F. James and M. Roos. 'MINUIT' a system for function minimization and analysis of the parameter errors and correlations. *Comput. Phys. Commun.*, 10:343, 1975.

[39] F. Kakimoto et al. A measurement of the air fluorescence yield. *Nucl. Instr. Meth. in Phys. Res. A*, 372:527, 1996.

[40] B. Keilhauer. private communication, 2006.

[41] B. Keilhauer, J. Blümer, R. Engel, and H. O. Klages. Impact of varying atmospheric profiles on extensive air shower observation: Fluorescence light emission and energy reconstruction. *Astroparticle Physics*, 25:259, 2006.

[42] H. V. Klapdor-Kleingrothaus and K. Zuber. *Teilchenastrophysik*. Teubner Verlag, Stuttgart, 1997.

[43] W Kolhörster et al. Gekoppelte Höhenstrahlen. *Naturwiss.*, 10:576, 1938.

[44] The Argonne National Laboratory. http://www.anl.gov.

[45] G. Lefeuvre. *Precise measurement of the Absolute Yield of the Fluorescence of Nitrogen in the Air. Effects on the Detection of the Cosmic rays of Ultra-high Energy*. PhD thesis, l'Université Denis Diderot, Paris, France, 2006.

[46] M. S. Longair. *High energy astrophysics*. Cambridge University Press, Cambridge, 1981.

[47] K. B. Mitchell. Fluorescence efficiencies and collisional deactivation rates for $N_2$ and $N_2^+$ bands excited by soft x rays. *J. Chem. Phys.*, 53(5):1795, 1970.

[48] A. Morozov, R. Krücken, J. Wieser, and A. Ulrich. Gas kinetic studies using a table-top setup with electron beam excitation: quenching of molecular nitrogen emission by water vapour. *The European Physical Journal D*, 33:207, 2005.

[49] M. Nagano, K. Kobayakawa, N. Sakaki, and K. Ando. Photon yields from nitrogen gas and dry air excited by electrons. *Astroparticle Physics*, 20:293, 2003.

[50] M. Nagano, K. Kobayakawa, N. Sakaki, and K. Ando. New measurement of photon yields from air and the application to the energy estimation of primary cosmic rays. *Astroparticle Physics*, 22:235, 2004.

[51] M. Nagano and A. A. Watson. Observations and implications of the ultrahigh-energy cosmic rays. *Rev. Mod. Phys*, 72(3):689, 2000.

[52] National Aeronautics and Space Administration (NASA). U.S. Standard Atmosphere. NASA-TM-X-74335, 1976.

[53] S. H. Neddermayer and C. D. Anderson. Note on the nature of cosmic ray particles. *Phys. Rev*, 51:884, 1937.

[54] S. V. Pancheshniy, S. M. Starikovskaia, and A. Yu. Starikovskii. Measurements of rate constants of the $N_2(C^3\Pi_u, v = 0)$ and $N_2^+(B^2\Sigma_u^+, v = 0)$ deactivation by $N_2, O_2, H_2$ and $H_2O$ molecules in afterglow of the nanosecond discharge. *Chem. Phys. Lett.*, 294:523, 1998.

[55] S. V. Pancheshnyi, S. M. Starikovskaia, and A. Yu. Starikovskii. Collisional deactivation of $N_2(C^3\Pi_u, v = 0, 1, 2, 3)$ states by $N_2, O_2, H_2$ and $H_2O$ molecules. *Chem. Phys.*, 262:349, 2000.

[56] R. W. B. Pearse and A. G. Gaydon. *The Identification of molecular Spectra*. Chapman and Hall, London, 1976.

[57] T. Pierog et al. Dependence of the longitudinal shower profile on the characteristics of hadronic multiparticle production. In *Proc. 29th Int. Cos. Ray Conf.*, volume 7, page 103, Pune, India, 2005.

[58] B. Povh, K. Rith, Ch. Scholz, and F. Zetsche. *Teilchen und Kerne*. Springer Verlag, Berlin, 2004.

[59] P. Privitera. private comunication, 2006.

[60] NIST ESTAR Database Program. http://physics.nist.gov/PhysRefData/Star/Text/ESTAR.html.

[61] M. V. S. Rao and B. V. Srekantan. *Extensive Air Showers*. World Scientific Publishing, Singapore, 1998.

[62] M. Risse and D. Heck. Energy release in air showers. *Astropart. Phys.*, 20:661, 2004.

[63] C. J. Sansonetti, M. L. Salit, and J. Raeder. Wavelengths of spectral lines in mercury pencil lamps. *Appl. Opt.*, 35(1):74, 1996.

[64] K. Shinozaki and M. Teshima. AGASA results. *Nuclear Physics B (Proc. Suppl.)*, 136:18, 2004.

[65] R. W. Springer for the HiRes collaboration. Recent results from the HiRes air fluorescence experiment. *Nuclear Physics B (Proc. Suppl.)*, 138:307, 2005.

[66] J. C. Street and E. C. Stevenson. New evidence for the existence of a particle of mass intermediate between proton and electron. *Phys. Rev.*, 52:1003, 1937.

[67] H. Ulrich et al. Energy spectrum and elemental composition of cosmic rays in the PEV region. *Euro. Phys. J. C*, 33(s01):944, 2004.

[68] T. Waldenmaier. private communication, 2006.

[69] T. Waldenmaier. *Spectral Resolved measurement of the nitrogen fluorescence yield in air induced by electrons*. PhD thesis, Universität Karlsruhe, Germany, 2006. Report FZKA 7209, Forschungszentrum Karlsruhe.

[70] G. T. Zatsepin and V. A. Kuz'min. Upper limit of the spectrum of cosmic rays. *JETP Lett.*, 4(3):78, 1966.